UNIVERSITY OF SOUTHAMPTON

# Direct Laser Writing in Semiconductors for Photonics Applications

by

Stuart J. MacFarquhar

A thesis submitted for the
degree of Doctor of Philosophy

in the
Faculty of Engineering and Physical Sciences
Zepler Institute for Photonics and Nanoelectronics

May 2022

UNIVERSITY OF SOUTHAMPTON

ABSTRACT

FACULTY OF ENGINEERING AND PHYSICAL SCIENCES
ZEPLER INSTITUTE FOR PHOTONICS AND NANOELECTRONICS

Doctor of Philosophy

by Stuart J. MacFarquhar

Research in silicon photonics is accelerated by the extensive understanding of silicon fabrication from the microelectronics industry, and silicon appears to be ideally placed to offer a solution for the integration of photonic layers onto an electronic chip. However, the manufacture of a crystalline silicon film requires high temperatures incompatible with back-end-of-line integration with the complementary metal-oxide semiconductor process flow. Significant interest therefore lies in research into low-temperature fabrication of alternatives to crystalline silicon. This thesis presents a direct laser crystallisation technique suitable for use in a low-temperature fabrication process flow, and demonstrates its applications in a range of semiconductor materials.

Laser writing is used to define waveguides in thin films of hydrogenated amorphous silicon, which has attracted attention for optical applications due to its low transmission losses and high nonlinear refractive index. A lithography-free waveguide definition process is proposed, and the optical loss of the resulting waveguides is measured and compared to those in conventionally fabricated waveguides.

The laser crystallisation process is then applied to etched wire structures in low temperature deposited amorphous silicon, maintaining a substrate temperature below the thermal budget for back-end-of-line integration. The material and optical properties of the resulting polycrystalline material are investigated by Raman spectroscopy, X-ray diffraction crystallography, cutback transmission measurements and nonlinear optical characterisation, and found to be comparable to those of single-crystal silicon. Most significantly, the lowest losses to date are recorded at $2.4\,\mathrm{dB\,cm^{-1}}$, and third-order nonlinear characteristics in or near the range reported for crystalline silicon are measured.

Finally, the application of the laser writing process to silicon-germanium is investigated. Silicon-germanium is a binary alloy with composition-dependent properties and applications. The laser writing system is used to carry out localised tailoring of the germanium fraction. The change in local composition is investigated by Raman spectroscopy, electron microscopy and finite-element simulation, and the effect on the photoconductivity is studied.

# Contents

# List of Figures

# List of Tables

# Nomenclature

| | |
|---|---|
| AFM | Atomic force microscopy |
| $Ar^+$ | Argon ion |
| a-Si | amorphous silicon |
| a-Si:H | Hydrogenated amorphous silicon |
| BEOL | Back end of line |
| BOX | Buried oxide |
| BSED | Backscattered electron diffraction |
| $C_4F_8$ | octofluorocyclobutane |
| CCD | Charge-coupled device |
| CMOS | Complementary metal-oxide-semiconductor |
| CMP | Chemical mechanical polishing |
| CNC | Computer numerical control |
| c-Si | Crystalline silicon |
| CVD | Chemical vapour deposition |
| CW | Continuous wave |
| CWLA | Continuous-wave laser annealing |
| DCIM | Differential contrast interference microscopy |
| DRAM | Dynamic random access memory |
| e-beam | Electrom-beam |
| ELA | Excimer laser annealing |
| FCA | Free carrier absorption |
| FOM | Figure of merit |
| FWM | Four-wave mixing |
| FWHM | Full-width at half maximum |
| Ge | Germanium |
| $GeH_4$ | Germane |
| GVD | Group velocity dispersion |
| HF | Hydrofluoric acid |
| HWCVD | Hot-wire chemical vapour deposition |
| ICP-RIE | Inductively-coupled plasma reactive ion etching |
| IR | Infrared |
| $K_2Cr_6O_7$ | Potassium dichromate |

| | |
|---|---|
| LPCVD | Low-pressure chemical vapour deposition |
| NA | Numerical aperture |
| Nd:YAG | Neodymium-doped yttrium aluminum garnet |
| NLSE | Nonlinear Schrödinger Equation |
| OSA | Optical spectrum analyser |
| PECVD | Plasma-enhanced chemical vapour deposition |
| polySi/polysilicon | Polycrystalline silicon |
| RF | Radio-frequency |
| rms | Root-mean square |
| sccm | standard cubic centimetres per minute |
| SEM | Scanning electron microscope |
| $SF_6$ | Sulphur hexafluoride |
| Si | Silicon |
| SiGe | Silicon-germanium |
| $SiH_4$ | Silane |
| $SiO_2$ | Silica |
| SLG | Super-lateral growth |
| SOI | Silicon on Insulator |
| SPC | Solid-phase crystallisation |
| SPM | Self-phase modulation |
| TFT | Thin-film transistor |
| THG | Third harmonic generation |
| TPA | Two-photon absorption |
| UV | Ultraviolet |
| XPM | Cross-phase modulation |
| XRD | X-ray diffraction |

# Acknowledgements

My immense thanks go to my supervisors, Anna Peacock and Harold Chong, for their advice, support and assistance throughout this project. Their invaluable guidance, encouragement and expertise have made this work possible.

I would also like to extend my gratitude to the Engineering and Physical Sciences Research Council and the Optoelectronics Research Centre for supporting and financing this project, and to beamline I18 at Diamond Light Source, for enabling some of the key findings.

I would like to thank my colleagues from across the university and beyond, for their support and aid throughout. To Yohann Franz for passing on his experience in the field and for teaching me so many of the processes that I came to rely on for this work, and to Ozan Aktas for his expertise and his unwavering enthusiasm and encouragement. To the fabrication team: SweZin Oo, Antulio Tarazona, Callum Littlejohns and Ying Tran for carrying out the deposition and lithography work, with particular gratitude to SweZin for her time training me on analysis tools. To Neil Sessions and Kathleen Leblanc for their assistance in the cleanrooms, and to Konstantin Ignatyev for his guidance at Diamond Light Source. I thank my co-authors for their assistance on each project, and I would also like to thank the rest of the Nonlinear Semiconductor Photonics research group, past and present, who aided me over the course of my PhD. Finally, I would like to wish the best to Amar Ghosh as he continues the avenues of investigation that I have been working on.

Outside of work there are a great many people whose support must be recognised. My thanks go to Lauren Stockley for her lifelong friendship, and to Tegan Birch, Alathea Fernyhough, Harri Lawes and especially to Ben Farmer, for keeping me sane throughout my undergraduate and postgraduate degrees. To Joseph Campling, Mathias Weisen, Jake Prentice and Dean Clarke for the countless entertaining and valuable conversations over the past five years. Writing a thesis during the COVID-19 pandemic has been no easy task, but the regular digital company of friends has made it that bit easier. For that, my thanks go to Sam Walstow, Thomas Davies, Suzannah Boardman, Elizabeth Martin, James Castelow, Devon Compton, Daniel Bull, Ian Jones, Raphaël Durand-Delacre, Callum Anderson, Kennie Hayward, Michael Sessions and Sebastian Chenerey.

I would like to thank everyone at Southampton University Archery Club, particularly my coach Gary Carr who taught me so much.

I must also thank Callum Anderson and Alex Smith, and Jason Khuu, Hannah Liddell, John Murray, Ethan Samama and Nicholas Cooke, who found space in their homes for me to stay while I returned to Southampton to complete my experimental work.

Finally, I must thank my family for their constant support. My parents and my brother, who have always encouraged and believed in me, and my extended family, particularly my uncle James, who has always been happy to help where he can.

Thank you, everyone.

# Declaration of Authorship

I, Stuart James MacFarquhar, declare that the thesis entitled *Direct Laser Writing in Semiconductors for Photonics Applications* and the work presented in the thesis are both my own, and have been generated by me as a result of my own original research.

I confirm that

1. This work was done wholly or mainly while in candidature for a research degree at this University;
2. Where any part of this thesis has previously been submitted for a degree or any other qualification at this University or any other institution, this has been clearly stated;
3. Where I have consulted the published work of others, this is always clearly attributed;
4. Where I have quoted from the work of others, the source is always given. With the exception of such quotations, this thesis is entirely my own work;
5. I have acknowledged all main sources of help;
6. Where the thesis is based on work done by myself jointly with others, I have made clear exactly what was done by others and what I have contributed myself;
7. Parts of this work have been published as listed in Appendix C.

Signed:

Date: 30$^{\text{th}}$ May 2022

# Chapter 1

# Introduction

## 1.1 Silicon Photonics

Originating in the 1980s from the pioneering work of Soref and Lorenzo [1], [2], the field of silicon photonics has vastly outstripped market value predictions as it takes an ever-greater role in the telecommunications industry [3], [4]. This is due in part to the significant body of research which has been carried out into semiconductor fabrication technology for microelectronics, which can be translated into the photonics domain.

Crystalline silicon (c-Si) has a multitude of attractive properties for optical applications. The high refractive index at telecommunications wavelengths ($n = 3.64$ at $\lambda = 1550\,\text{nm}$[5]) enables small waveguide dimensions while maintaining good optical confinement, minimising the waveguide footprint and therefore maximising component density. The broad transmission window in the infrared (IR), ranging from $1.1\,\mu\text{m}$ to $7\,\mu\text{m}$, allows low-loss waveguides across the telecommunications wavelength range and beyond, and the excellent nonlinear properties of silicon hold the potential for on-chip optical signal processing.

Since the first demonstration of waveguiding in silicon, a multitude of photonic devices have been developed, including sub-$1\,\text{dB}\,\text{cm}^{-1}$ loss waveguides [6], optical filters for wavelength multiplexing [7], electro-optic modulators [8], ring resonators [9], [10], and on-chip lasers [11]. Furthermore, with the inclusion of germanium, telecommunications-wavelength photodetectors have also been fabricated [12]. This broad range of applications, when considered in tandem with the requirement in microelectronics for high-bandwidth communications beyond the limits of metal interconnects, has resulted in significant research interest in the integration of silicon photonics with complementary metal-oxide semiconductor (CMOS) microelectronics. To fully demonstrate viable integrated optoelectronic circuitry, the fabrication of both passive (e.g. bus waveguides and ring resonators) and active (e.g. sources and detectors) components must be achieved in an integrated optical system.

Integration of photonic circuits on electronics layers in c-Si has been demonstrated [13], with an example of an optoelectronic layer shown in Figure 1.1. The fabrication of electronic transistors alongside waveguides demonstrates the capacity for parallel integration, but this is not without some significant drawbacks. The thin insulation layer in electronics is insufficient for optical purposes, and so selective underetching must be carried out to avoid significant optical losses. The component density is also limited, with four "paperclip" waveguides at the top of the die in Figure 1.1 occupying an area approximately equal to that required for 250,000 transistors. Therefore, multilayer photonic integration is desirable to maximise the real estate available for electronics and to minimise design constraints.

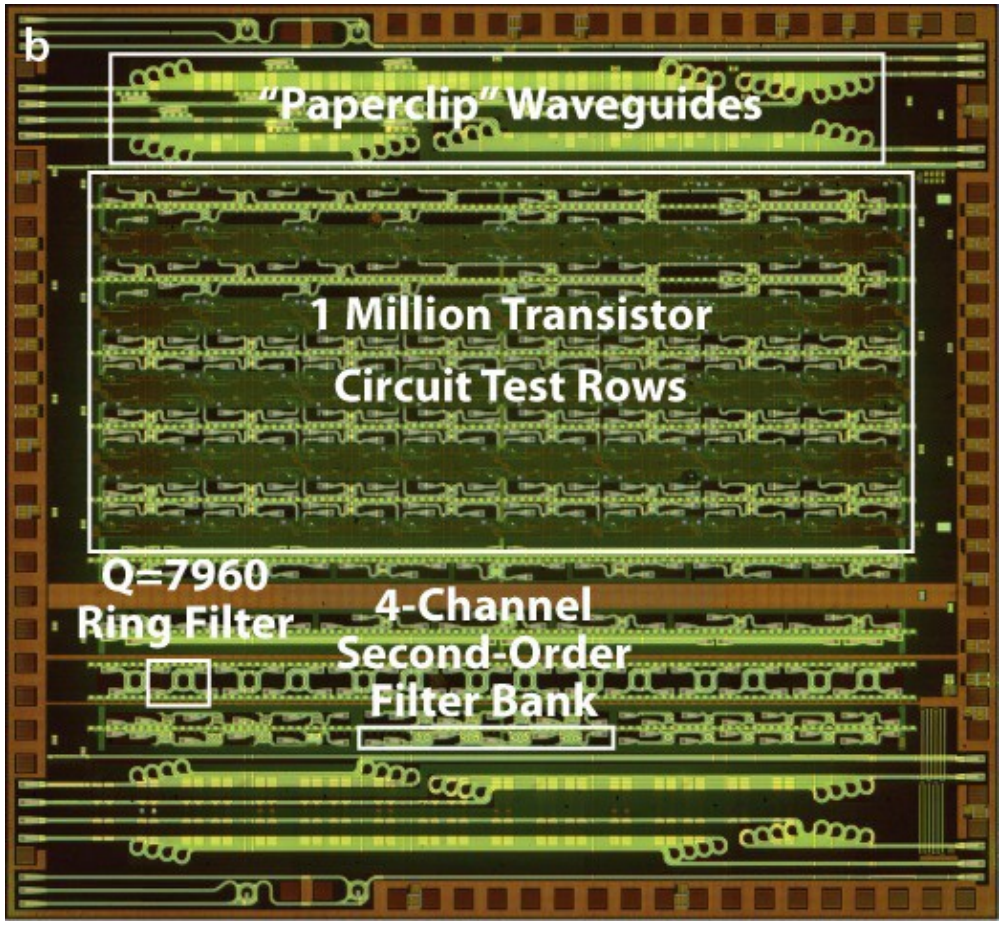


FIGURE 1.1: A silicon die with photonic and electronic components, from [13].

Thin films of photonic c-Si can be fabricated by epitaxial growth, however this process requires substrate temperatures between 600 °C and 1100 °C [14]. This process is therefore incompatible with back-end-of-line (BEOL) integration, as the CMOS metallisation step imposes a thermal budget of 450 °C to all subsequent process stages. In an attempt to avoid this temperature limitation, other integration processes have been investigated.

Front-end-of-line integration (i.e. before the CMOS metallisation stage) has been studied, allowing conventional annealing of the photonic silicon. However, the subsequent CMOS temperature cycles were shown to degrade waveguide performance, increasing optical losses by 32% [15]. Flip-chip bonding, common to the electronics fabrication processes, is a promising option for photonic integration. Photonic chips can be independently fabricated, avoiding the temperature limitations of fabrication on an electronics chip, and the completed chips are then bonded together, positioned using high-precision alignment systems [16]. However, this has the consequence of increasing the fabrication cost by adding a new stage that requires expensive equipment for high-accuracy placement. Alternatively, co-packaging approaches have also been investigated, offering high interconnection density and scalable design features[17]. However, some limitations are present, in particular the limited accuracy of standard high-volume fabrication devices [18].

To overcome these problems, attention has turned to other silicon-based materials with the capacity for direct integration, including polycrystalline silicon (polysilicon), hydrogenated amorphous silicon (a-Si:H) and silicon-germanium (SiGe), the materials of interest in this thesis.

## 1.2 Materials of Interest to This Thesis

Polysilicon consists of c-Si grains with amorphous silicon (a-Si) boundaries, with the electrical and optical properties dependent on the relative amorphous and crystalline content. The irregular bond lengths, dangling bonds and defect sites in a-Si cause optical and electrical scattering, and optical loss by absorption. Therefore, a significant body of research has been carried out with the goal of maximising the grain sizes of polysilicon films [19]–[35]. A more detailed discussion of the material properties of polysilicon and the existing research are provided in Section 2.1 and Section 5.2.

Early researchers investigating polysilicon for waveguiding fabricated polysilicon films by either direct deposition, or by post-deposition oven annealing of a-Si [28], [36]–[44]. However, these processes use high substrate temperatures in excess of the CMOS thermal budget. Later work investigated the crystallisation of a-Si films by excimer laser annealing (ELA) [45], [46], a method common to the manufacture of thin-film transistors (TFTs) [26], [27], [32], [47], [48]. By applying the heat treatment directly to the a-Si in short bursts, laser crystallisation is achieved without significant heat transfer to the substrate.

Following investigations into continuous-wave laser annealing (CWLA) of silicon-core fibres [33], [34], work began in our group to study the application of a similar procedure to planar geometries [49]. Already an area of investigation in the electronics industry, where maximisation of grain size is desirable for TFT applications, part of this thesis

is an investigation into CWLA of low-temperature deposited planar a-Si films, with the goal of producing low loss polysilicon waveguides suitable for optoelectronic integration. The objective was to reduce losses, from the current best achieved value of $5\,\mathrm{dB\,cm^{-1}}$ reported by Franz et al. [35], to better than $3\,\mathrm{dB\,cm^{-1}}$, as effective nonlinear propagation has been seen in optical fibers with losses at this level.

Hydrogenated amorphous silicon as an optical material has been widely investigated due to its low transmission losses [50] and nonlinear properties [51]–[53]. With its favourable deposition flexibility, it is a potential material for multilayer photonic systems. Although its electrical properties are limited by the amorphous structure, its potential for use as a low-dimension optical interconnect or for signal processing is significant. Waveguides in a-Si:H are typically defined lithographically, however scattering losses from waveguide sidewall roughness has been identified as a significant source of loss in etched waveguides [6], [54]. The work on a-Si:H in this thesis was carried out to investigate a novel process of waveguide definition, using direct laser writing to create a polysilicon cladding in a lithography-free process flow.

Finally, the binary alloy silicon-germanium has been widely investigated due to the modifications to the optical and material properties associated with the incorporation of Ge. For example, the bandgap of SiGe is lower than that of c-Si, enabling photodetection [12]. Additionally, the nonlinear properties of SiGe are superior to those of c-Si [55], [56], and so its applications for signal processing have been considered. These applications, and others, often make use of graded material content, which under standard fabrication techniques is limited to vertical tailoring. This work investigates the use of direct laser writing to induce highly localised lateral compositional segregation, and investigates the resulting changes in material properties.

## 1.3 Thesis Outline

Chapter 2 of this thesis sets out the theoretical background for this work. First, the relevant optical and material properties of c-Si, a-Si:H, polysilicon and SiGe are given, and the resulting suitability of these materials for photonic applications is discussed. The mechanisms of crystallisation are then described, in the context of common methods of fabrication of polysilicon films. The mechanisms of optical loss are then outlined, followed by the essential mathematics of optical waveguiding and dispersion.

Chapter 3 discusses the techniques used in the manufacture, processing and characterisation of the samples studied. Material growth by plasma-enhanced and hot-wire chemical vapour deposition (CVD), etching by electron-beam lithography, and the system used for localised laser crystallisation are described. In each case, a discussion of the suitability of each method for optoelectronic integration is explained. This is followed by an explanation of the processes for characterisation of optical and material properties

by Raman spectroscopy, X-ray diffraction crystallography and cutback transmission loss measurements.

Chapter 4 covers the experimental work towards a new method of lithography-free waveguide definition using localised laser crystallisation of a-Si:H to create the waveguide cladding from low refractive index polysilicon. Following optimisation of the processing conditions, the technique is compared to conventional lithography methods, and its applicability to complex structures is considered.

Chapter 5 contains the bulk of the work for this project, pursuing the development of a localised laser processing technique for producing low-loss polysilicon waveguides. The crystalline quality, characterised using Raman spectroscopy and X-ray diffraction crystallography, is compared to that obtained from other crystallisation techniques, and record low losses are presented.

Chapter 6 follows on from the previous work, describing the efforts undertaken to demonstrate the third-order optical nonlinear response in polysilicon. Following the discussion of the uses of nonlinear optics in c-Si, the theory, measurement procedures, computational simulations and experimental results are presented.

Chapter 7 relates to work led by Dr Ozan Aktas, investigating the laser segregation of materials in a silicon-germanium alloy. The chapter provides a background of the motivation, proof-of-concept and fabrication, before focusing on my contributions to the work - specifically, the determination of local material composition by analysis of Raman spectroscopy measurements. The characterisation of the photoconductivity of the laser-written SiGe stripes is then described, providing context for the broader scope of the work.

Chapter 8 concludes the thesis, summarising the results obtained throughout the project, highlighting the versatility of the laser crystallisation technique used, and demonstrating the importance of novel contributions. Finally, potential avenues of further investigation are discussed.

## 1.4 Contributions

The work reported in this thesis has been carried out by me, under the supervision of Professor Anna Peacock and Professor Harold Chong. Some contributing work has been carried out by others, as detailed here.

The deposition and, where appropriate, lithographical etching of samples was predominantly carried out by members of Professor Harold Chong's group in the Electronics and Computer Science department. Of particularly great assistance in this regard were Dr SweZin Oo and Dr Antulio Tarazona.

X-ray diffraction crystallography measurements as detailed in Chapter 5 were carried out mainly by myself with the assistance of Dr Sakellaris Mailis, Dr Yohann Franz and Dr Ozan Aktas, and Dr Konstantin Ignatyev provided assistance in his capacity as the principal beamline scientist for beamline I18 at Diamond Light Source. Dr Amar Ghosh assisted with Raman spectroscopy measurements and collection of data for error calculations. The Matlab script used in Chapter 6 to solve the nonlinear Schrödinger equation was written by Professor Anna Peacock.

The work on silicon-germanium in Chapter 7 was led by Dr Ozan Aktas, who carried out the bulk of the laser processing work. My main contribution was the writing and use of a Matlab script to identify the germanium concentration from Raman spectroscopy measurements.

# Chapter 2

# Background Theory

This chapter covers some of the fundamental physical concepts of the work undertaken. First, the properties of a range of silicon materials are discussed, highlighting the optical characteristics relevant to this thesis, and the advantages and drawbacks of each material in regard to optoelectronic applications and fabrication. Following this, the principles of crystallisation are covered, comparing the processes for furnace annealing, excimer laser annealing and continuous-wave laser annealing. Sources of optical loss are then described. The chapter concludes with a review of waveguide structures, mode confinement and optical dispersion.

## 2.1 Properties of Silicon-Based Optical Materials

Silicon has been a material of interest for optical applications since 1985, when the use of single-crystal silicon as a passive waveguiding structure was demonstrated [1]. This was followed shortly afterwards by active components in 1986 [2]. Since then, other silicon-based materials have also been used. Of particular interest to this thesis are polysilicon, a-Si, a-Si:H and SiGe.

This section provides a brief overview of the compositional differences of these materials, and discusses the effects of these on their optical characteristics. Figure 2.1 shows the structural differences between crystalline (a), polycrystalline (b), amorphous (c) and hydrogenated amorphous (d) silicon using a schematic lattice structure. The true arrangement of a Si lattice is discussed in Section 3.2.2. Of particular note are the amorphous boundaries separating crystalline grains in polysilicon and, within the amorphous areas, the irregular bond length and disconnected 'dangling' bonds, which can be passivated with the addition of hydrogen.

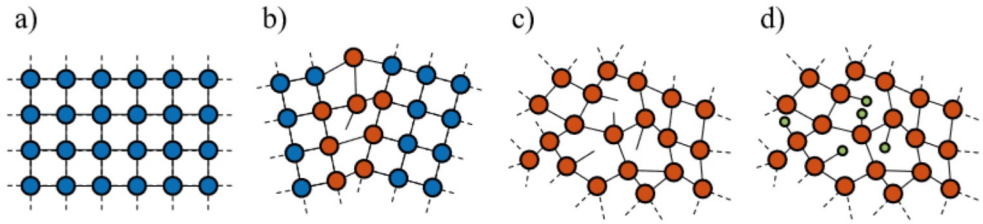


FIGURE 2.1: Schematic structure of different forms of silicon. a) Single-crystal silicon has long-range order with a diamond-like lattice structure. b) Two crystal grains (blue) separated by an amorphous grain boundary (orange) in polysilicon. c) a-Si with dangling bonds and defects. d) Hydrogen atoms (green) passivate dangling bonds and defect sites in a-Si:H.

### 2.1.1 Crystalline Silicon

Crystalline silicon has good electronic and optical properties, with an electron mobility of around $1000\,\mathrm{cm^2\,V^{-1}\,s^{-1}}$, and an optical transparency window ranging from 1.1 µm to 7 µm [57]. The bandgap of 1.11 eV causes absorption at shorter wavelengths ($<$ 1.1 µm), as these photons have sufficient energy to excite an electron from the valence to the conduction band. Losses as low as $2\,\mathrm{dB\,cm^{-1}}$ have been measured at 1550 nm in conventionally-fabricated small-core waveguides [58]. This is limited primarily by the capabilities of current fabrication techniques, rather than being a material limit, as losses of $0.31\,\mathrm{dB\,cm^{-1}}$ have been reported in large-core c-Si waveguides [42]. The primary source of loss has been shown to be surface roughness, discussed in greater detail in Section 2.3.2, as small-core waveguides with surface roughness below 0.5 nm have exhibited losses of only $0.3\,\mathrm{dB\,cm^{-1}}$ [6]. The high refractive index at telecommunications wavelengths ($n = 3.45$) ensures good light confinement when used with the conventional silica ($SiO_2$) cladding, reducing waveguide dimensions and increasing component density. Moreover, by comparison with other common optical materials such as $SiO_2$, silicon has excellent nonlinear properties, discussed further in Chapter 6. Silicon is widely used in photonic applications, such as wavelength conversion [59], parametric amplification [60], Mach-Zehnder modulation [61], and supercontinuum generation [62].

However, the capacity for optoelectronic integration of c-Si is limited by the constraints of the material, and the different manufacturing process flows typical to electronics and photonics. The standard electronics CMOS process flow makes the growth of additional silicon layers for multilayer fabrication incompatible, due to the thermal budget imposed by the ion implantation and metallisation stages [45]. Proposed alternatives include flip-chip wafer bonding [63]–[65], and epitaxial growth of local silicon islands [66], however these methods suffer from high cost and limited design options due to fabrication tolerances [46]. Another common approach is the use of polysilicon, either by deposition or by laser annealing of amorphous silicon. In the case of laser annealing, care must be

taken to minimise transfer of heat to the substrate, as the melting temperature of silicon (1414 °C) is significantly greater than the damage threshold for back-end integration.

### 2.1.2 Amorphous Silicon

Unlike c-Si, a-Si has no long-range order, with the consequence that the high variation in bond length and the density of defects results in high absorption. However, the deposition of high-quality films of a-Si at low temperatures is a well-established process. The addition of hydrogen during the deposition process is used to passivate the dangling bonds, and has resulted in measured losses below $1\,\mathrm{dB\,cm^{-1}}$ [50], [67]. The refractive index of a-Si:H has been measured as similar to, but higher than that of c-Si, with $n = 3.69$ [50]. Active devices such as all-optical [68], and thermo-optic Fabry-Perot modulators [69] have been demonstrated in a-Si:H, and the nonlinear parameters are favourable when compared to c-Si. Narayanan and Preble reported a nonlinear coefficient $\gamma$ (discussed in Chapter 6) in a-Si:H five times higher than that in c-Si, suggesting that for applications such as nonlinear optical switching, a-Si:H would be the more suitable material [51]. The most significant drawback of a-Si:H is its poor electrical properties. The electron mobility, estimated at $10\,\mathrm{cm^2\,V^{-1}\,s^{-1}}$ [70], makes it unsuitable for electronics applications.

### 2.1.3 Polycrystalline Silicon

Polycrystalline silicon consists of multiple c-Si grains separated by a-Si boundaries. The irregular bond lengths, dangling bonds, and defects within these boundaries contribute to optical losses, the mechanisms of which are discussed in greater detail in Section 2.3.

Like the optical properties, the electrical properties of polysilicon are limited by the amorphous content. Estimates of the electron mobility are around $100\,\mathrm{cm^2\,V^{-1}\,s^{-1}}$ [38], limiting its use in electronic layers or for devices such as electro-optic modulators. However, it is likely that advancements in fabrication technology that enable large grain sizes would improve the mobility and expand the range of potential uses.

Despite the electron mobility being approximately an order of magnitude lower than that in c-Si, it is sufficient for some applications. In particular, polysilicon has been widely used in the electronics industry for solar cells and thin-film transistors. The work on these has fuelled extensive research into deposition flexibility and fabrication processes [19]–[27], [71]–[73], and the standard manufacture processes (low-pressure CVD and laser annealing of amorphous silicon) are suitable for multilayer fabrication without necessitating flip-chip bonding or epitaxial growth, which are required for multilayer c-Si structures. This makes polysilicon a promising material for multilayer optoelectronic integration, with the most significant barrier being the high optical losses [74], [75].

However, in recent decades an extensive body of research in optics has driven the transmission losses of polysilicon ever closer to the sub-3 $\mathrm{dB\,cm^{-1}}$ losses observed in c-Si waveguides [15], [28], [36]–[46], [76]–[79]. As well as passive waveguides, a range of important optical components and effects have been demonstrated in polysilicon, including optical modulation [40], [41], [46], ring resonators [38], [45], and bandgap tailoring in fiber geometry [34]. A comprehensive discussion of these advancements is presented in Chapter 5.

### 2.1.4 Silicon-Germanium

Silicon-germanium is a binary alloy, with the composition typically denoted as $\mathrm{Si}_{1-x}\mathrm{Ge}_x$ for an atomic Ge fraction $0 < x < 1$. The incorporation of Ge influences the material properties in a number of ways, most significantly changing the transmission window, refractive index and material bandgap. Pure Ge has good transmission between 1.8 µm and $\sim$ 14 µm, a refractive index of 4.2 at 1550 nm and a bandgap of 0.66 eV. The melting temperatures of Si and Ge are 1414 °C and 938 °C respectively, while the solidus temperature in $\mathrm{Si}_{1-x}\mathrm{Ge}_x$ is given by $(1412 - 738x + 263x^2)$°C [80]. In the SiGe alloy, the composition determines the exact values of the material and optical properties, making the precise tailoring of the Ge content a valuable tool for enabling a variety of applications such as photodetection [81], electro-optic modulation [82], and nonlinear optics [55].

Each of the materials discussed in this section present different requirements and limitations in terms of fabrication. Crystalline Si and Ge require high-temperature processes such as epitaxial growth to fabricate a high-quality film, limiting the range of systems into which they can be incorporated. By contrast, a-Si:H requires lower temperatures to avoid crystallisation or hydrogen out-diffusion. For ease of comparison between materials, the relevant parameters are summarised in Table 2.1.

## 2.2 Crystallisation

The manufacture of polysilicon through annealing of deposited a-Si has been an area of extensive research in both the photonics and electronics industries [19], [21], [25]–[28], [30]–[32], [36], [37], [47], [48], [93]–[95], as it is a suitable material for electronic components such as thin-film transistors [21], [25], [26], [30], [32], [47], [48], [93], [94], and has applications in solar cell technology [19], [21], [31]. In general terms, crystallisation occurs in two distinct regimes - solid-phase crystallisation (SPC) and liquid-phase annealing. The methods discussed here, furnace annealing and laser annealing, typically make use of solid-phase and liquid-phase annealing respectively. Optimisation of the material for electronic component performance has driven the interest in low-temperature

| Material Property | c-Si | a-Si:H | $Si_0.2Ge_0.8$ | c-Ge |
|---|---|---|---|---|
| Transmission Loss ($dB\,cm^{-1}$) | 2 [58] | 2 [67] | 1.3 [83] | 1.4 [84] |
| Transmission Window (µm) | $1.1-7$ | $0.7-7$ | $1.5->7$ | $1.8-14$ |
| Refractive Index | 3.45 | 3.69 [50] | 3.86 [85] | 4.2 |
| Bandgap (eV) | 1.11 | 1.85 [86] | 0.80 [87] | 0.66 |
| $\beta_{TPA}$ ($10^{-12}\,m\,W^{-1}$) | $4-9$ | 7 [88] | High* [89] | $\sim$120 [90] |
| $n_2$ ($10^{-18}\,m^2\,W^{-1}$) | $4.3-6$ | 17 [88] | 13 [89] | 4 [90] |
| Electron Mobility ($cm^2\,V^{-1}\,s^{-1}$) | 1000 | 10 | 500 [91] | 3000 [92] |
| Melting Temperature (°C) | 1414 | | 1097 [80] | 938 |

TABLE 2.1: Direct comparisons of material properties of c-Si, a-Si:H, SiGe and c-Ge. Values for the transmission loss and nonlinear coefficients are given at $\lambda = 1550\,nm$ except for Ge, where they are given at 2 µm. Transmission losses are taken for single-mode waveguides, therefore dimensions vary. Refractive indices are given at 1550 nm. Where relevant, $T = 293\,K$. *Exact data not given, but value indicated to be in excess of $2.5 \times 10^{-9}\,m\,W^{-1}$.

processes to maximise crystal grain sizes, as increasing crystal grain size is linked with improved electronic properties [95].

### 2.2.1 Solid-Phase Furnace Annealing

The furnace annealing process offers a high throughput, as a-Si is crystallised in a high temperature oven and so many samples can be treated at once. In early experiments in polysilicon for optics, samples were subjected to uniform heating to temperatures between 600 °C and 1100 °C [28], [36], [37]. It was noted by Liao et al. that "a high temperature (1100 °C) thermal treatment yielded lower losses than a lower temperature (600 °C) anneal because of improved degree of crystallinity, larger grain size, fewer grain boundaries and fewer light-absorbing dangling bonds." [37]. Generally speaking, enlargement of grain sizes reduces optical loss by increasing the crystalline fraction of the material, reducing the interaction between the propagating light and the absorption and scattering sites in the amorphous boundaries. Grain sizes of approximately 0.2 µm were obtained using this approach. However, furnace annealing is not suitable for the maturing field of polysilicon photonics. Back end of line integration with the CMOS process flow imposes a thermal budget of 450 °C, as higher temperatures risk damage to metal contacts in the electronics layers [38], [96]. To avoid exceeding this, other approaches such as laser annealing must be explored.

### 2.2.2 Laser Annealing

Laser annealing and crystallisation of polysilicon falls into two main categories. The first is excimer laser annealing, which uses a pulsed laser, typically homogenised over an area of several square centimetres, to induce rapid crystallisation in thin films. The second,

continuous-wave laser annealing, typically crystallises smaller areas and has therefore been less widely adopted due to the lower manufacture volume throughput. Here I will discuss the development of each technology, the bulk of which has been carried out in the field of electronics due to the suitability of polysilicon for TFT applications. The main focus here will be on the increase in crystal grain sizes, as the reduction of scattering and absorption at grain boundaries was a major objective for this project.

#### 2.2.2.1 Excimer Laser Annealing

Excimer laser annealing uses a near-UV pulsed laser to crystallise an amorphous film, and is commonly used in the electronics industry, thanks to high volume output. The incident laser beam is homogenised and expanded to cover an area of several square centimetres. The pulsed laser transfers a large amount of energy in a short time, crystallising the amorphous film but avoiding heating the substrate.

ELA can be divided into two main regimes, labelled as low energy density and high energy density [27], distinguished by whether the incident energy is sufficient to fully melt the exposed volume. In the low energy density regime, crystal grain size has a slight dependence on energy fluence, until the incident power is sufficient to nearly fully melt the film. The remaining solid areas act as nucleation sites, seeding crystallisation as shown in Figure 2.2a. Grain size shows a significant increase when fluence is sufficient to prompt super-lateral growth (SLG), in which only a small number of residual solid regions remain in any given volume (Figure 2.2b). The seeded crystals are therefore significantly larger. In the high energy density regime, crystal grain size is unaffected by the fluence, as complete melting of the film has been achieved, and so no solid material remains to act as a nucleation site. The nucleation is therefore spontaneous, occurring throughout the entire molten volume, and the resulting crystals are smaller than in SLG, as seen in Figure 2.2c.

Typical grain sizes from ELA are in the range of 0.1 µm to 0.9 µm [26], [27], [32], [47], [48], with grain sizes beyond $\sim 0.3\,\mu m$ only achieved from SLG. The presence of the amorphous boundaries places limitations on the optical and electrical properties of ELA-produced polysilicon, with electron mobility of approximately $100\,cm^2\,V^{-1}\,s^{-1}$ [47], and optical losses of around $20\,dB\,cm^{-1}$ [46].

#### 2.2.2.2 Continuous-Wave Laser Annealing

Research has been conducted on the use of CWLA of a-Si films for electronics applications [19]–[25], [30], [31], [71], [72], [93], [94], [97]–[99], with some focus on the maximisation of grain size in planar films. Unlike ELA, maximum grain size is achieved when the incident laser power approaches the ablation threshold of the film [100]. The

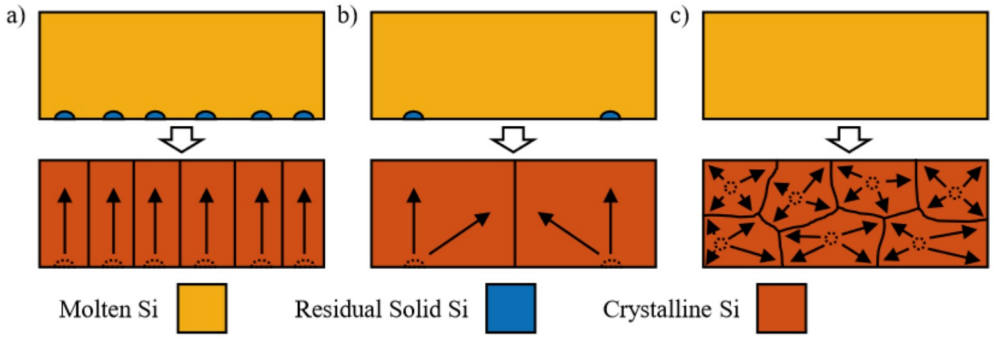


FIGURE 2.2: Cross-section schematics of grain growth during during excimer laser annealing. a) Low energy density exposure leaves many solid regions which act as nucleation sites for small crystal grains. b) In super-lateral growth, few solid points remain and these seed large crystal growth across the film. c) In the high energy density regime, the exposed film is completely melted and crystal nucleation is spontaneous, resulting in small crystals.

high fluence, in combination with the long exposure time relative to ELA, results in long cooling times which encourages the growth of larger crystals (approximately 600 µm was reported by Kawamura et al. [25]) from a smaller number of nucleation sites.

These large grain sizes were achieved with a shaped beam, as using a Gaussian beam profile results in a high energy transfer to the film at the beam centre, but the lower laser fluence at the beam edges does not raise the temperature to the same extent. The outer edges therefore crystallise first with a large number of small crystals, and these smaller crystals then act as seeds for larger ones which grow inwards towards the centre of the beam path, as shown in Figure 2.3a. This growth tendency results in a characteristic 'chevron' pattern visible under a scanning electron microscope (Figure 2.3b). The grain boundaries across the waveguide cause high scattering and absorption losses.

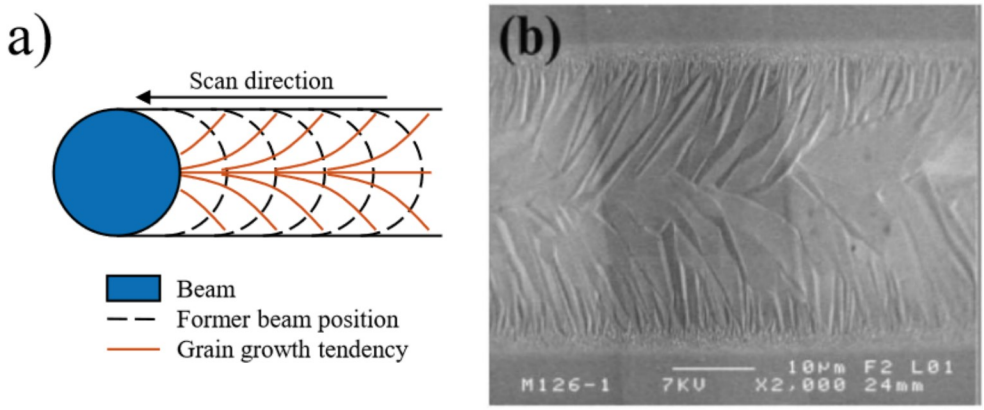


FIGURE 2.3: Grain structures in planar laser-crystallised polysilicon are a consequence of the heat distribution profile across the Gaussian beam. a) Crystallisation begins at the outer edges and propagates towards the beam path centre as the material solidifies. b) Scanning electron microscope image of chevron-structured grains from CWLA following selective etching of the amorphous material, from [100].

However, laser crystallisation of silicon in a confined geometry, specifically the core of a silicon fiber, showed that it was possible to achieve single-crystal growth across the full material width [34]. In particular, it was proposed that the confinement of the core ensured complete melting of the silicon, eliminating nucleation from residual solid material and supporting the growth of large crystal grains. The altered dynamics of the crystallisation process mean that here, unlike in ELA, complete melting is desirable and results in large grains rather than small ones. As the laser is scanned along the fibre length, the molten zone moves, so that the crystallisation of the cooling material is seeded from the previously crystallised volume. Without additional nucleation sites, this becomes the dominant seed, and the crystal growth follows the laser spot along the fiber core as shown in Figure 2.4.

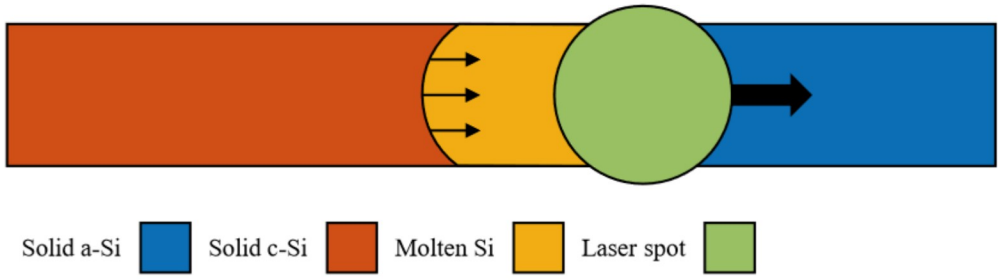


FIGURE 2.4: Laser crystallisation in a confined fiber core. As molten material solidifies, crystal growth is seeded from the previously crystallised areas.

This complete melting and nucleation suppression is potentially replicable in on-chip geometries by etching waveguide structures in advance of crystallisation, as shown in Figure 2.5. This was first investigated by Franz et al. [35], who obtained the best results by carrying out the crystallisation process with a laser spot diameter larger than the width of the target waveguide. The Gaussian beam profile transfers less heat at the edges of the laser spot, causing solid-phase crystallisation in a planar film. This issue is avoided in an etched waveguide, as complete melting is achieved, with roughly homogeneous energy transfer at any given point reducing the tendency for nucleation at the outer edges of the waveguide.

In summary, furnace annealing typically produces low grain sizes of approximately 200 nm, and despite the high production capacity is unsuitable for integrated optoelectronic systems due to the high temperatures required. ELA also offers a high volume throughput, but grain sizes remain limited to below 1 µm. CWLA is the slowest process, but compensates for this with significantly larger grain sizes. In planar films, grains of up to 600 µm have been reported [25], while the constrained fiber geometry has allowed the growth of single-crystal material along the entire processed length.

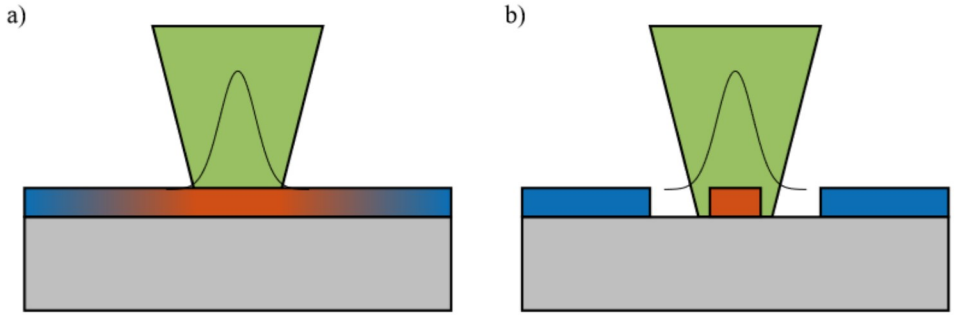


FIGURE 2.5: Heat confinement in a) planar and b) etched structures, showing how etching reduces thermal transfer. The Gaussian profile across the incident laser beam shows the beam intensity profile.

## 2.3 Optical Loss

Although much work has gone into increasing the grain size in polysilicon, the optical loss measured within a material at the wavelength of interest is the most important characteristic in determining its suitability for photonic applications. The reduction of loss in polysilicon has been the driving focus of research into polysilicon photonics. In this section, I will provide an overview of the sources and mathematical treatment of optical loss.

Equation 2.2 shows the exponential attenuation of light passing through a medium, with the intensity $I$ at a distance $z$ through the medium given by

$$I(z) = I_0 e^{-\mu z}, \tag{2.1}$$

where $I_0$ is the initial intensity, and $\mu$ is an attenuation coefficient with units $\mathrm{cm}^{-1}$. Isolating the attenuation coefficient gives

$$\mu = -\frac{1}{z} \ln\left(\frac{I(z)}{I_0}\right) \tag{2.2}$$

For experimental measurement of loss, it is easier to rewrite this in terms of the input and output power ($P_{in}$ and $P_{out}$) from a given length of material $L$, and convert to a logarithmic decibel scale. The loss coefficient $\alpha$ (units $\mathrm{dB\,cm}^{-1}$) is then

$$\alpha = \frac{10 \log_{10}}{L}\left(\frac{P_{in}}{P_{out}}\right) \tag{2.3}$$

Note that the negative sign has been removed for consistency with the rest of this thesis, in which the losses will be reported as positive values.

Contributions to the linear loss $\alpha$ arise from several different sources. Applicable to the materials and waveguides studied in this thesis are absorption, Rayleigh scattering and surface roughness.

### 2.3.1 Absorption

Optical absorption in a semiconductor material such as silicon arises primarily due to the excitation of electrons from the valence band to the conduction band. The silicon bandgap of 1.11 eV ensures low single-photon absorption at standard telecommunications wavelengths, as 1550 nm light has a photon energy of 0.8 eV. The transmission spectra of 5 mm crystalline silicon and crystalline germanium are shown in Figure 2.6.

Additionally, in-grain defects in the crystal structure and dangling bonds at crystal grain boundaries create bandgap states, which cause greater absorption in polycrystalline materials. Increasing crystal grain sizes therefore reduces optical loss to approach values similar to that of a crystalline material.

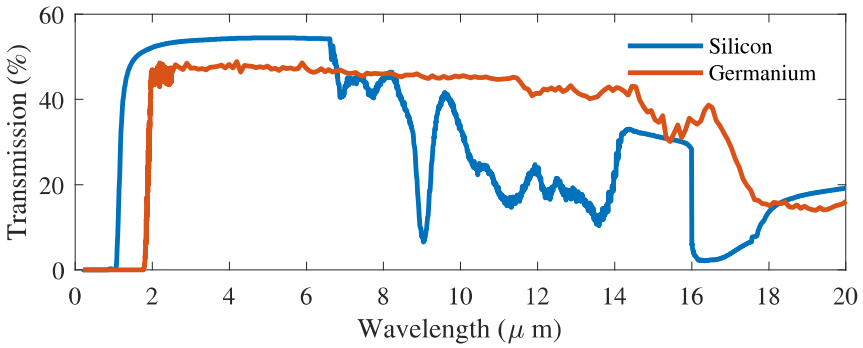


FIGURE 2.6: Transmission through 5 mm Si and Ge in the wavelength range 0.2 µm to 20 µm. The sharp increase in transmission at 1.1 µm in Si and 1.8 µm in Ge corresponds to the wavelength below which photons are sufficiently energetic to excite electrons across the bandgap. Data from Thorlabs [101], [102].

### 2.3.2 Scattering from Surface Roughness

Surface scattering $\alpha_s$ from a rough waveguide sidewall results from the coupling induced by these imperfections between guided and unguided modes, the complete mathematical consideration of which was developed by Marcuse [103]. For an approach more specifically tailored to scattering into radiation modes, a simpler alternative was developed by Payne and Lacey [104]. They derived the expression

$$\alpha_s = \frac{\sigma^2}{\sqrt{2}k_0 d^4 n_1} g(V) f_e(x, \gamma) \tag{2.4}$$

for a waveguide of width $2d$, root mean square (rms) surface roughness $\sigma$ and refractive index $n_1$ guiding a wave with free-space wavenumber $k_0$. The parameters $g(V)$ and $f_e(x, \gamma)$ are dependent on the waveguide and material characteristics. Applying this to the waveguides fabricated in this work, using $k_0 = 4.05 \times 10^6\,\mathrm{m}^{-1}$ (1550 nm), approximations of waveguide dimensions ($d = 1.5\,\mu\mathrm{m}$), and material properties such as the refractive index ($n_1 = 3.45$), the relation shown in Figure 2.7 is obtained between the surface roughness and the scattering loss.

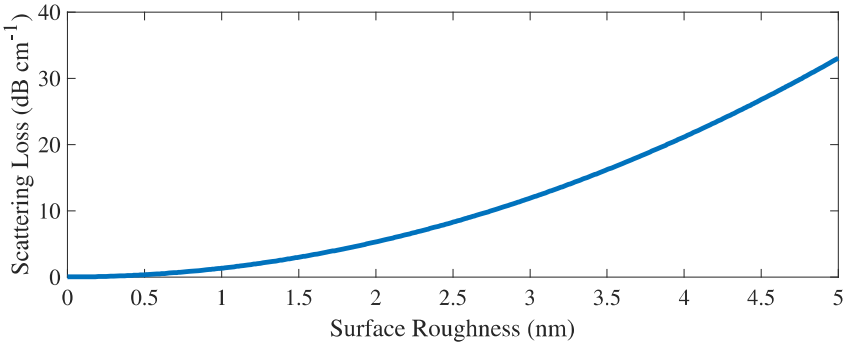


FIGURE 2.7: Estimated relationship between waveguide surface roughness and resulting scattering loss, based on the formulation in [104].

While Equation 2.4 was derived for single-mode systems, the general implication remains valid - that the surface roughness plays a significant role in defining the minimum transmission loss achievable in a waveguide. With 2 nm surface roughness resulting in approximately $5\,\mathrm{dB\,cm}^{-1}$ scattering loss, it is clear that significantly lower surface roughness must be achieved to meet the target of $3\,\mathrm{dB\,cm}^{-1}$ transmission loss in polysilicon waveguides. The presence of higher order modes in a waveguide would be expected to increase scattering loss from surface roughness, as the different electric field distribution would bring the intensity peaks closer to the sidewall. Additionally, the polarisation of the guided mode influences scattering loss, with significantly higher losses from both the upper surface and sidewall roughness typically being observed in TM modes compared to TE modes [105], [106].

### 2.3.3 Rayleigh Scattering

Rayleigh scattering is an intrinsic loss mechanism resulting from density fluctuations in the guiding medium. Taking the approximate form

$$\alpha_R = C_R \lambda^{-4}, \tag{2.5}$$

where $\alpha_R$ is the Rayleigh scattering loss, $C_R$ is a proportionality term and $\lambda$ is the wavelength of the scattered light, it can be seen that shorter wavelengths are more

significantly affected. When the relevant materials in this thesis, a-Si:H and polysilicon, are considered, the influence of Rayleigh scattering will be marginally different due to the different approaches taken when fabricating waveguides. In a-Si:H, the number of scattering points is dependent on the deposition quality, while in polysilicon waveguides the crystallisation process is also a determining factor. Defects and grain boundaries will cause Rayleigh scattering, and so by optimising the crystallisation process to reduce these, the scattering loss can be reduced.

## 2.4 Waveguiding

This section discusses waveguide structures, and the mathematics of optical confinement and dispersion.

### 2.4.1 Waveguide Structures

The key principle of optical waveguiding is the confinement of light in a high refractive index core, which is surrounded by a low-index cladding. A wide variety of waveguide structures are used in photonics, with some of the most common shown in Figure 2.8. Ridge waveguides (a) are typically fabricated by lithography and have an air cladding on three sides, while diffuse waveguides (b) are usually defined by ion implantation to change the material composition in a selected region. Buried waveguides (c) are common to multilayer photonic systems where a cladding is applied above a ridge waveguide to act as insulation between optical layers, as well as to insulate the waveguide from the surrounding environment. Slot waveguides (d) are commonly used for sensing applications, where a gas or liquid entering the central slot alters the propagation of light through the waveguide. This project focuses on ridge and diffused waveguides, however the principles outlined may also be applicable to other structures. A variant on the diffused waveguide structure using hydrogenated amorphous silicon is presented in Chapter 4, while polysilicon ridge waveguides are presented in Chapter 5 and Chapter 6. Diffuse structures in silicon-germanium are presented in Chapter 7, although the waveguiding properties of these are not investigated.

Just as important as the waveguide structure is the refractive index contrast between core and cladding. Increasing the difference between the core and cladding index improves the optical confinement, influencing both the mode interaction with the core and the minimum possible waveguide dimensions. The confinement in ridge waveguides, with an air cladding, will therefore offer greater confinement than a buried waveguide. Buried waveguides in common low-loss materials such as silica will also require larger waveguide dimensions due to the lower refractive index contrast, enhancing the appeal of silicon photonics for on-chip applications. However, a lower index contrast reduces

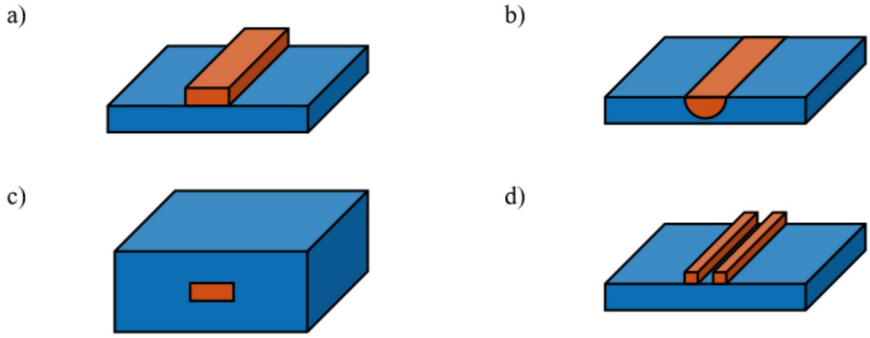


FIGURE 2.8: Common waveguide structures with low-index cladding (blue) and high-index core (orange), showing a) ridge, b) diffused, c) buried and d) slot waveguides.

the scattering loss from surface roughness, and so the influence of each factor must be considered when selecting a material for a specific application.

### 2.4.2 Optical Confinement

An electromagnetic wave propagating in free space must satisfy Maxwell's equations, the solution to this being a plane wave with the electric field component taking the form

$$\mathbf{E}(z) = Ee^{-ikz}e^{i\omega t}. \tag{2.6}$$

$E$ is the amplitude of the wave, $k$ is the wavenumber, $z$ is the distance in the $z$-axis along which the wave is assumed to be propagating, $\omega$ is the frequency and $t$ is time. For a wave propagating in a non-vacuum medium such as a waveguide, the expression becomes more complex. The generalised form of this is

$$\mathbf{E}(x, y, z) = \mathbf{E}(x, y)e^{-i\beta z}e^{i\omega t}, \tag{2.7}$$

where $\mathbf{E}(x, y)$ is the electromagnetic field distribution in the $x$ and $y$ axes, and $\beta$ is the propagation constant. For simple systems, a solution can be obtained analytically, but for more complex structures such as those studied in this thesis, numerical simulations are required, as the polarisation and electric field direction can vary across the waveguide. Figure 2.9 shows a simulation of the fundamental transverse electric (TE) mode of a polysilicon waveguide such as those studied in Chapter 5. The simulation was carried out using COMSOL Multiphysics, and shows the magnitude of $\mathbf{E}(x, y)$ across a waveguide cross-section and the surrounding $SiO_2$ substrate and air cladding.

From these simulations, values of the effective refractive index $n_{\text{eff}}(\omega)$ and effective mode area $A_{\text{eff}}$ can be calculated. These values can then be used to determine the mode

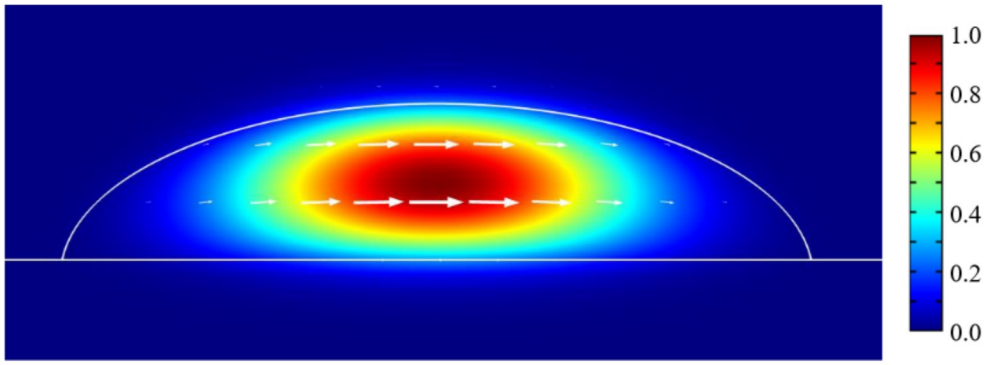


FIGURE 2.9: Simulated mode profile in a laser-crystallised polysilicon waveguide. Colour scale shows normalised electric field intensity, arrows show field direction. The shape, being neither rectangular nor cylindrical, prevents analytical calculation of the mode profile, effective area or effective refractive index.

intensity and the optical dispersion for nonlinear simulations, as described in Chapter 6. Calculation of $n_{\text{eff}}$ also enables determination of $\beta$, which is related to the effective index by $\beta(\omega) = n_{\text{eff}}(\omega)k_o = n_{\text{eff}}(\omega)\omega/c$, where $k_0$ is the free-space wavenumber of the wave and $c$ is the speed of light in vacuum.

### 2.4.3 Optical Dispersion

In a non-vacuum medium, a propagating wave will be subject to dispersion, which is most evident when considering an optical pulse with many constituent frequency components. Chromatic dispersion arises due to the refractive index of the medium. As the pulse propagates, each frequency component will experience a different phase shift due to the frequency dependence of the refractive index. Waveguide dispersion is influenced by the waveguide geometry and the refractive indices of the core and cladding, which can be used to calculate an effective refractive index $n_{\text{eff}}$. For non-trivial systems such as those studied in this thesis, $n_{\text{eff}}$ is calculated numerically, for example by using finite-element method computation. To understand the influence of dispersion on a pulse, a Taylor expansion of $\beta$ around the central pulse wavelength $\omega_0$ can be used. This gives

$$\beta(\omega) = \beta_0 + \beta_1(\omega - \omega_0) + \frac{\beta_2}{2}(\omega - \omega_0)^2 + \frac{\beta_3}{6}(\omega - \omega_0)^3 + \ldots \tag{2.8}$$

where

$$\beta_m = \left(\frac{d^m\beta}{d\omega^m}\right)_{\omega=\omega_0} \tag{2.9}$$

Typically, only the terms $\beta_1$ and $\beta_2$ are required for this analysis, as higher-order terms become negligibly small. $\beta_1$ governs the propagation velocity, or group velocity $v_g$, of the overall pulse, and is equivalent to

$$\beta_1 = \frac{1}{v_g} = \frac{1}{c}\left(n + \omega\frac{dn}{d\omega}\right). \tag{2.10}$$

The term $\beta_2$ is known as the group velocity dispersion (GVD) parameter, and is given by

$$\beta_2 = \frac{1}{c}\left(2\frac{dn}{d\omega} + \omega\frac{d^2n}{d\omega^2}\right). \tag{2.11}$$

This describes the rate at which a pulse spreads in the temporal domain as a result of the phase shift experienced by each frequency component. The GVD can exist in three distinct regimes. The first, where $\beta_2 > 0$, is the normal dispersion regime, and lower frequencies propagate fastest. The second, where $\beta_2 < 0$, is the anomalous regime, and the reverse is true. Finally, in the case where $\beta_2 = 0$, the pulse is centred at the zero-dispersion wavelength (ZDW) and higher order dispersion terms must be considered. The ZDW is frequently used in applications which require phase matching, for example where nonlinear processes such as four-wave mixing are desired. As the total dispersion has influences from both the material and the waveguide dimensions, the structure can be tailored to obtain propagation in a desired regime. Large waveguides are typically governed by the normal dispersion regime, as the primary influence on dispersion is from the material. As dimensions are reduced, the geometry changes the effective index, and when the waveguide is small enough the anomalous dispersion takes over.

# Chapter 3

# Sample Fabrication and Characterisation Processes

This chapter describes the general fabrication and characterisation processes used for the samples investigated in this project. First, the processes for CVD, electron-beam (e-beam) lithography and CWLA are presented, highlighting the suitability of each process for the requirements of the projects in which they were used. The characterisation processes used to assess the quality of the materials are then described, covering Raman spectroscopy and X-ray diffraction crystallography. Finally, the optical coupling setup used for linear transmission measurements is shown, and the method by which transmission losses were calculated is explained along with a discussion of the methods used for facet preparation.

## 3.1 Manufacture Processes

This section provides a description of the generic production stages used to fabricate the samples investigated throughout this project. Two CVD techniques, hot-wire CVD (HWCVD) and plasma-enhanced CVD (PECVD), are described, and the steps used in e-beam lithography to define the waveguides are detailed. Finally, the setup used for subsequent laser crystallisation of the samples is described. As a variety of materials were studied, the exact fabrication conditions used for each are given in the relevant chapters. The deposition and lithography stages were carried out by members of Professor Harold Chong's research group, due to their expertise in thin-film semiconductor fabrication.

### 3.1.1 Chemical Vapour Deposition

CVD processes are a mature technological field encapsulating a wide variety of distinct methods for material production. However, all methods rely on the same basic principle

in which a precursor gas is injected into a deposition chamber and broken down into constituent parts, which then adsorb onto a substrate. In this work, two examples have been used, HWCVD and PECVD. HWCVD was used to deposit a-Si and a-Si:H on c-Si substrates with an optically isolating $SiO_2$ buried-oxide layer, while PECVD was used to grow amorphous $Si_{0.4}Ge_{0.6}$ directly onto c-Si.

#### 3.1.1.1 Hot-Wire CVD

Typical CVD processes such as low-pressure CVD present numerous challenges for obtaining CMOS-compatible device-quality a-Si or a-Si:H films. Most require high substrate temperatures to aid the thermal decomposition of precursor gases, making them unsuitable for the manufacture of integrated optoelectronic systems due to the back-end-of-line thermal budget. In this regard, HWCVD offers a suitable alternative with numerous advantages over other methods [107]–[109]. Specifically, high substrate temperatures are unnecessary, as decomposition occurs when the precursor gas flows over a high-temperature filament, as shown in Figure 3.1. Additionally, HWCVD is a plasma-free process, eliminating the risk of damage occurring from high-energy ion impact during deposition. Finally, HWCVD has demonstrated high deposition rate and uniformity over large areas, ideal for both high-turnover experimental work and larger-scale high-throughput manufacture.

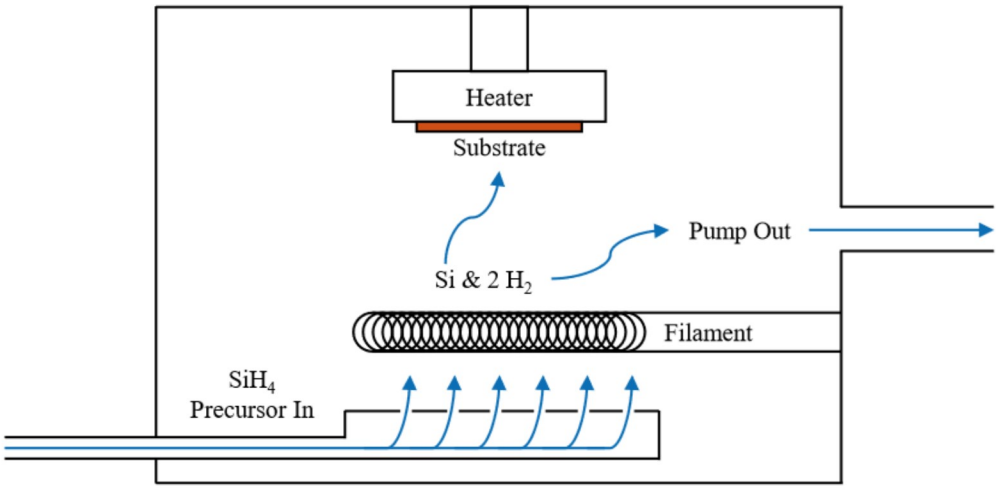


FIGURE 3.1: Schematic representation of a Hot-Wire Chemical Vapour Deposition chamber during the deposition of an amorphous silicon film. The silane precursor undergoes thermal decomposition into silicon radicals, which are deposited on the substrate, and gaseous hydrogen, which is removed from the chamber.

The HWCVD process is as follows. After the evacuation of the deposition chamber, both the substrate and the tungsten filament are brought up to the desired temperature to ensure a constant deposition rate. For the samples manufactured for this thesis, the substrate temperature was 230 °C and the filament temperature was 1730 °C. The

precursor gas silane ($SiH_4$) passes over the filament, and thermally decomposes to silicon and hydrogen. The silicon then adsorbs to the substrate surface while the hydrogen is removed from the chamber by the vacuuming system. Hydrogen can be incorporated into the deposited layer, forming a-Si:H, by adding molecular hydrogen to the precursor gas mix. This has the effect of passivating dangling bonds in the amorphous structure, thus reducing optical loss. However, when heating the sample to produce polySi, the thermal outdiffusion of hydrogen from a-Si:H has been observed to induce damage to the material surface [79], and so for the samples studied in Chapters 5 and 6, hydrogen content was minimised by adjustment of the gas pressure.

#### 3.1.1.2 Plasma-Enhanced CVD

In PECVD, the dissociation of precursor gases is brought about by the presence of a radio-frequency (RF) alternating electric field. An inert argon gas is injected and ionised to form a plasma. The precursor gases are then introduced, and the high-energy ions break down the precursor gases into ions and free radicals. The electric field from the cathode repels the ions, which are directed toward the grounded electrode on which the substrate is mounted, while uncharged free radicals are pumped out of the system. The substrate is heated to promote material adhesion, and the temperature can be altered to influence the structure of the deposited film. Low temperatures produce an amorphous film, while higher temperatures (typically $> 500\,^{\circ}C$) are required to form polycrystalline material. In this project, PECVD was used for the fabrication of amorphous $Si_{0.4}Ge_{0.6}$ films, with the conditions for this detailed in Section 7.2.1. Deposition was carried out directly onto the c-Si substrate, allowing it to act as a heat sink during laser crystallisation.

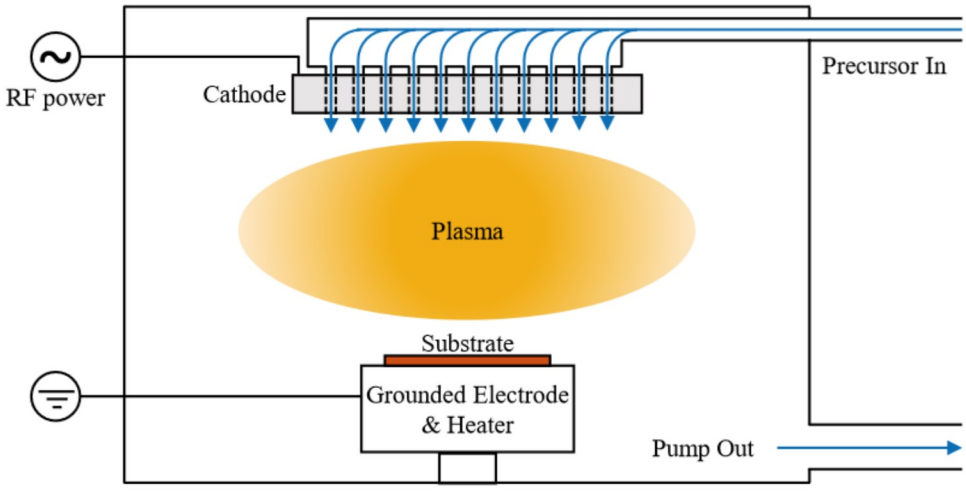


FIGURE 3.2: Schematic of a PECVD chamber. Precursor gases are broken down by the plasma generated by the RF field. Ions are repelled by the cathode and deposit on the substrate.

### 3.1.2 Electron-Beam Lithography

Lithography is a conventional means to transfer a desired pattern from a 'mask' onto a material layer. Typically, ultraviolet-light photolithography is preferred due to the fast process allowing high volume throughput. Few-second exposure times are sufficient regardless of the area to be processed, as the entire sample surface is exposed simultaneously. E-beam lithography is an alternative, preferred for high-detail structures that are harder to produce using photolithography due to diffraction at sub-wavelength scales and the consequent resolution limitations. It is significantly slower than photolithography, however the higher accuracy and resolution make it favourable for small structures. As an early goal of this project was the laser processing of 1 µm width waveguides, e-beam was chosen. An additional advantage of the process is that changes to the pattern are easy, fast and cheap. Photolithography requires a physical mask, and so any change to the desired pattern requires a new mask to be designed and manufactured. By comparison, the e-beam mask is a digital file, and can therefore be adapted quickly and easily with no manufacture stages needed. For this reason, e-beam lithography was used for all patterned structures presented in this thesis.

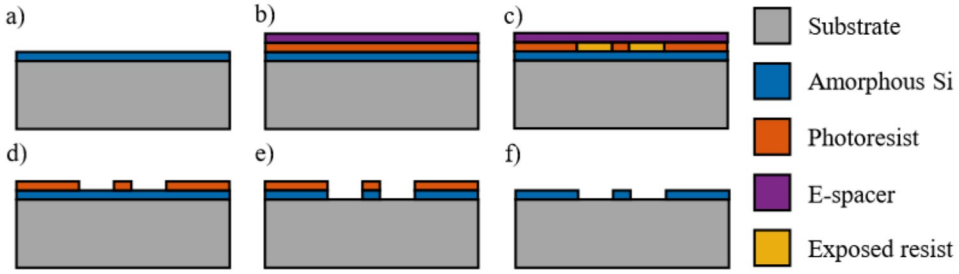


FIGURE 3.3: Electron-beam lithography process for structures in Chapter 5. a) Deposited amorphous silicon (blue) on substrate (grey). b) A positive resist layer (orange) is applied with an e-spacer (purple) to prevent charge accumulation. c) Selected regions (yellow) are exposed to a high-energy electron beam. d) The e-spacer is washed off, and development of the resist removes the exposed regions. e) Etching of the amorphous film isolates strip waveguide structures. f) The remaining resist layer is removed.

The lithography and subsequent etching steps used to produce waveguides used in the work described in Chapters 5 and 6 are shown in Figure 3.3. A ZEP-520A resist layer (orange) was applied by spin-coating on top of the layer onto which the pattern was to be transferred (blue). The spin coating was carried out at 2370 rpm for 15 s, giving a resist thickness of 435 nm. It was then fixed in place by a 180 s bake at 180 °C. The application of a conductive e-spacer (purple) avoided the accumulation of charge on the sample, eliminating pattern distortion due to same-charge repulsion. The sample was then exposed to the electron beam of a scanning electron microscope, which is directed to specific locations by the patterning file. The beam charge was set to 190 µC. This exposure alters the properties of the resist, making it either soluble or insoluble in a development fluid, depending on whether the resist is classified as 'positive' or 'negative'.

Following exposure, the e-spacer was removed with a water rinse and the resist was developed by immersion in a ZED developing fluid to expose areas of the underlying material layer as determined by the pattern. Inductively-coupled plasma reactive ion etching (ICP-RIE) was used to etch the exposed film. To monitor the etching rate and avoid over- or under-etching, the etch depth was measured by ellipsometry after a known process time. The etch rate was calculated, and the remaining etch time was adjusted to etch the full film thickness. The remaining resist was then removed and the sample cleaned to remove all residue.

### 3.1.3 Laser Annealing

Laser processing on the samples characterised in this thesis was carried out using a focused continuous-wave (CW) laser beam, with the beam power and position on the sample surface controlled using the setup shown in Figure 3.4. The arrangement shown is the final iteration of the system, however a number of changes were made throughout the project. The majority of these were system improvements to the alignment, focusing and user interface, with no change to the system functionality. The most significant change was the replacement of the laser source. Early samples were processed using an $Ar^+$ ion gas laser (Coherent Innova FreD) emitting at 488 nm, with an ouput power of $\sim 1$ W. However, due to a critical failure this was replaced with a 532 nm fiber laser (IPG GLR-10W) with a power range from 250 mW to 10 W. Prior to this failure, the $Ar^+$ laser quality was significantly deteriorating due to the age of the system, with the power delivered to the sample surface declining steadily over the course of weeks or months and requiring regular servicing. In addition, noticeable power fluctuations over individual processing sessions were observed. This made the installation of the fiber laser a significant upgrade to the system capabilities.

The change in wavelength between the lasers affected the absorption, with the penetration depths $\delta$ in silicon being $\delta_{488\,\mathrm{nm}} = 485$ nm and $\delta_{532\,\mathrm{nm}} = 814$ nm. The required incident power for each of the two lasers was therefore significantly different, as a film of thickness 400 nm absorbs a greater proportion of shorter-wavelength light. Additionally, a Roithner LaserTechnik ULV-445-700 diode laser emitting at 445 nm ($\delta = 224$ nm) was used briefly while awaiting delivery and installation of the fiber laser.

Laser output power was set at the computer-controlled CW fiber laser, and where necessary fine-tuned using a half-wave plate and polarising beam splitter. This addition allowed the use of powers incident on the sample surface below that given by the minimum laser output power of $\sim$250 mW. A collimated white light source, used for in-situ imaging of the sample surface, was coupled to the beam path using a dichroic mirror which transmits at the laser wavelength. The laser beam and white light were focused on the sample surface using a 10× objective, giving a laser spot with a diameter of 5 µm. The objective was mounted on a high-precision z-axis stage. The sample was

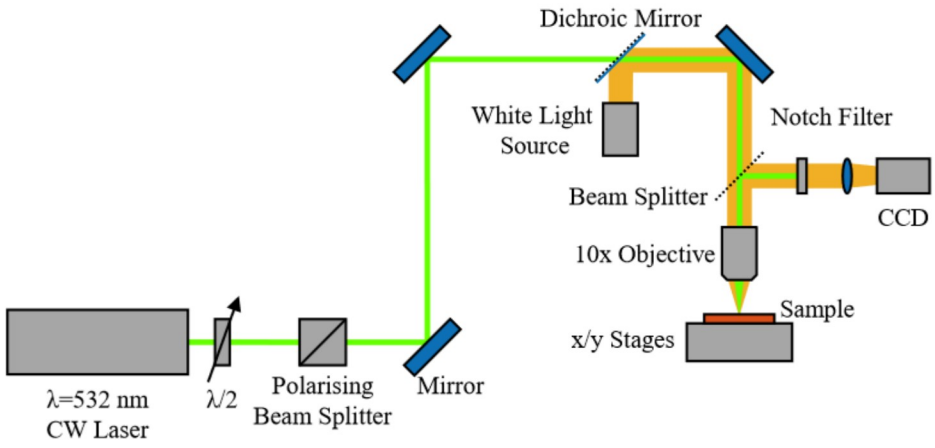


FIGURE 3.4: Laser crystallisation setup.

vacuum-mounted on high-precision x/y stages (Aerotech ABL-1500) which, along with the z-axis, were computer controlled using the G-Code CNC tool programming language, enabling reliable and repeatable control over the stage position and movement speed using pre-written programs. Although G-Code is capable of highly versatile and complex stage movements, the majority of work was kept to simple linear translation between two points, at constant velocity. Where more complex movements were necessary, these have been described in greater detail in the relevant section of the thesis. A small fraction of the back-reflected light was split off by a high-transmission beam splitter and directed towards a CCD camera, which had an adjustable lens to ensure that the imaging focus and laser focus were independent. A notch filter eliminated the laser wavelength, preventing damage to the CCD panel. The live image was used to ensure correct focus, select the start and end points of the laser path, and to monitor the waveguide during the crystallisation process.

## 3.2 Characterisation Techniques

Following laser crystallisation, material characterisation was carried out to gain an initial indication of the material quality and waveguiding viability before optical transmission characterisation began.

First, a visual inspection of the waveguides was carried out using a microscope, to identify any defects or damage that had occurred during laser writing. Then, Raman spectroscopy was used to estimate the crystallinity and any induced stress in the processed materials, by comparing the spectra to that of a crystalline reference. In the case of SiGe alloy materials, the Raman spectra were also used to determine the fractional composition at a given location. Loss measurements were then carried out to determine

the transmission loss in the waveguides, which is made up of material loss as well as surface and defect scattering. Additionally, some samples were studied using micro-focus X-ray diffraction crystallography at the Diamond Light Source facility.

### 3.2.1 Raman Spectrosopy

Raman spectroscopy utilises the principle of Stokes' radiation in which an incident photon is absorbed, exciting a phonon in the material and releasing a photon with a reduced energy compared to that of the original. This is shown in Figure 3.5. For a known incident photon energy $h\nu$, where $h$ is the Planck constant and $\nu$ is the frequency, and measured output energy $h(\nu - \Delta\nu)$, the energy difference $h\Delta\nu$ between ground and excited state can be calculated. The phonon energy is dependent on the atomic content and structure of the material in which it is excited, and so the recorded spectrum at the output can be used to identify the elemental composition and structural properties of the material under investigation.

The Raman spectroscopy system used was a Renishaw Invia, with a Nd:YAG excitation laser emitting at 532 nm. The beam was focused to a spot diameter of 1 µm, allowing highly localised investigation of the material content and crystallinity. This in turn makes high-resolution study of material composition and structure easily available. Conversely, it can also present a barrier to the investigation of material characteristics on a larger scale. Where large crystal grains or localised regions of uniform composition exist, a small investigation region limits the usefulness of the data from that point, and so multiple measurements must be taken to more accurately characterise the material.

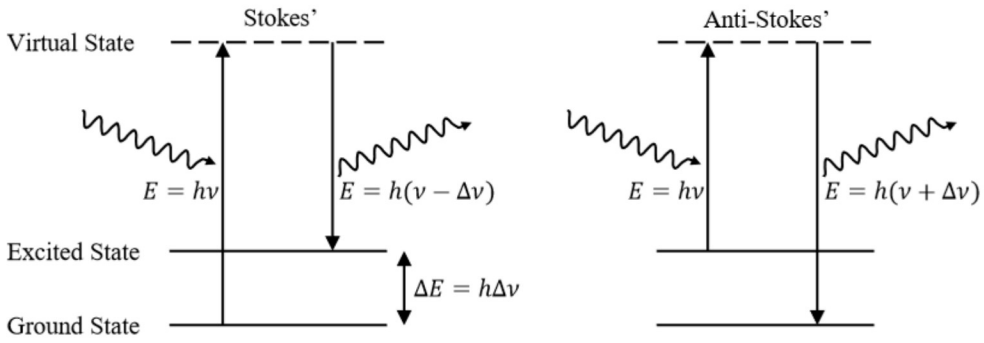


FIGURE 3.5: Energy level diagrams of the Stokes' and anti-Stokes' mechanisms. Incident radiation with energy $h\nu$ excites an atomic bond, which relaxes to a different energy state to that in which it started. The frequency shift of the radiation released during relaxation is determined by the energy difference between states. The anti-Stokes' mechanism is less common than the Stokes'.

Across the studies in this thesis, a number of different materials were investigated by Raman spectroscopy: polysilicon, SiGe and a-Si:H. The primary Raman peak positions associated with each material are shown in Table 3.1. In a-Si:H, the visible peaks are

from the amorphous silicon-silicon bond, and the Si-H bond. These peaks are broad, with a low intensity and approximate location. In polysilicon, the crystalline Si-Si bond is of much greater significance, although the amorphous material will still have some lesser contribution. Finally, in SiGe, the three peaks corresponding to the Ge-Ge, Si-Ge and Si-Si bonds will be seen. For each area of work, the application of Raman spectroscopy and analysis of the data was different, and so the methods have been fully explained in the relevant chapters.

| Bond | Peak Position ($cm^{-1}$) |
|---|---|
| Ge-Ge | 280 |
| Si-Ge | 411 |
| amorphous Si-Si | 480 |
| crystalline Si-Si | 520 |
| Si-H | 2000 |

TABLE 3.1: Raman shifts in bonds relevant to this thesis.

However, the Raman output from measured samples cannot be directly compared with the reference c-Si values. Raman spectrometers rely on an excitation laser, which has a Gaussian spectral beam profile. The material response will have a Lorentzian spectral profile, and the resulting peak will be a convolution of these. Therefore, the Gaussian influence on an experimental peak must be removed to make a valid comparison to the c-Si reference. This can be achieved using a Voigt function (Equation 3.1), the convolution of Gaussian and Lorentzian expressed as

$$V(x;\sigma,\gamma) \equiv \int_{-\infty}^{\infty} G(x';\sigma)L(x-x';\gamma)dx', \tag{3.1}$$

where $G$ is the Gaussian with standard deviation $\sigma$, $L$ is the Lorentzian with FWHM $\gamma$, and $x$ is the separation from the peak position $x'$. This can be approximated as

$$V(x;\sigma,\gamma) = \frac{\mathrm{Re}\left[w(z)\right]}{\sigma\sqrt{2\pi}} \tag{3.2}$$

where $w(z) := e^{-z^2}\,\mathrm{erfc}(-iz)$ is the Faddeeva function calculated for $z = (x+i\gamma)/\sigma\sqrt{2}$, erfc being the complementary error function. By taking a spectrum from a crystalline silicon reference with the known Lorentzian FWHM $2.7\,cm^{-1}$, the Gaussian standard deviation from the optical system can be calculated. This is then used to calculate the Lorentzian FWHM of the sample response by fitting to data with a constrained value of $\sigma$. The resulting value of $\gamma$ can be compared to the crystalline value to assess the material quality. A MATLAB script was written to carry out this process for all the Raman data collected.

### 3.2.2 X-Ray Diffraction Crystallography

X-ray diffraction (XRD) crystallography allows direct investigation of the crystalline structure of a material. The wavelength of the incident beam is comparable to the interatomic spacing of the crystal lattice structure such as that of c-Si, shown in Figure 3.6a. This therefore satisfies the necessary conditions for Bragg diffraction, with Equation 3.3 giving the angles $\theta$ at which constructive interference occurs:

$$\theta = \sin^{-1}\left(\frac{m\lambda}{2d}\right), \tag{3.3}$$

where $m$ is an integer corresponding to the order of diffraction, $\lambda$ is the incident wavelength and $d$ is the lattice spacing as shown in Figure 3.6b.

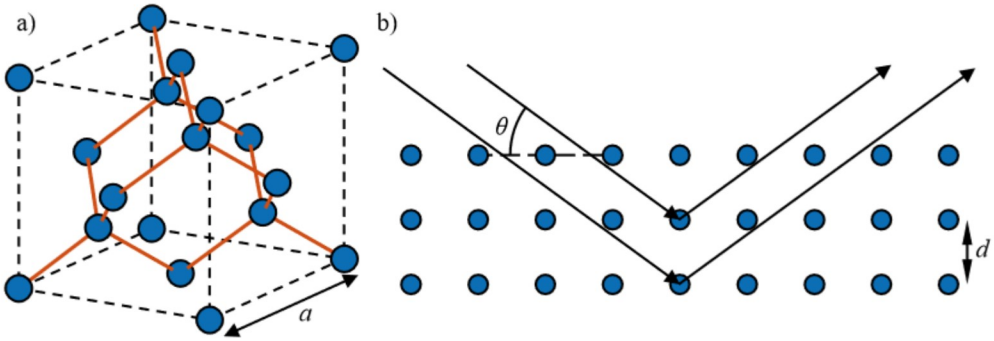


FIGURE 3.6: a) Unit cell of crystalline silicon, reproduced from Kittel [110]. b) Diffraction from crystallographic planes. Constructive interference occurs at discrete angles dependent on the lattice spacing $d$.

The lattice spacing is dependent on the orientation of the plane within the unit cell, denoted by the Miller indices $h$, $k$ and $l$, and the lattice constant $a$, and is given by the relation

$$d_{hkl} = \frac{a}{\sqrt{h^2 + k^2 + l^2}} \tag{3.4}$$

For crystalline silicon, $a = 5.430\,\text{Å}$ [110]. Figure 3.7 shows the planes denoted by $\langle 1\,0\,0\rangle$, $\langle 1\,1\,1\rangle$ and $\langle 2\,2\,0\rangle$, which have lattice spacings $d_{\langle 1\,0\,0\rangle} = 5.430\,\text{Å}$, $d_{\langle 1\,1\,1\rangle} = 3.135\,\text{Å}$ and $d_{\langle 2\,2\,0\rangle} = 1.920\,\text{Å}$ respectively. These are chosen as examples because the $\langle 1\,0\,0\rangle$ plane is the orientation of the standard single-crystal substrate, and the latter two are the planes with the next largest spacings.

XRD experiments were carried out using beamline I18 at Diamond Light Source on Harwell Campus, Didcot, Oxfordshire. The incident X-ray beam was focused to a 2 µm beam waist, and the samples were placed into the mount at a 4° grazing incidence as shown in Figure 3.8a. This angle extended the horizontal interaction zone to 30 µm, and

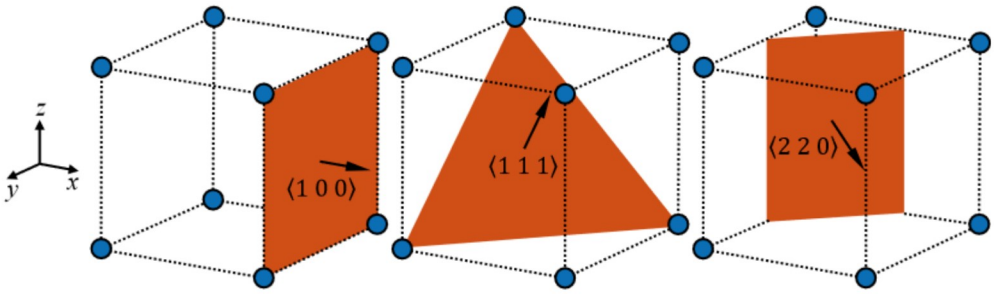


FIGURE 3.7: The $\langle 1\,0\,0\rangle$, $\langle 1\,1\,1\rangle$ and $\langle 2\,2\,0\rangle$ crystallographic planes in a simplified unit cell.

was chosen to maximise the interaction of the beam with the laser-written structures under investigation. Each crystal grain in a studied volume diffracts the incident X-rays according to the crystal orientation of the grain, and the angle of the diffracted beam can be calculated from Equation 3.3. A detector screen placed at a set distance from the interaction point captured the diffracted beams, and the diffraction angle $\theta_{hkl}$ associated with each crystal axis corresponds to a separation $r_{hkl}$ on the screen between the diffracted ray and the central beam path. The spots from individual crystal grains also have an angular offset $\phi$ around the central beam path, allowing individual grains to be distinguished even when they have the same crystallographic orientation. This is shown in Figure 3.8b, with the example of five distinct grains in the interaction volume, and in Figure 3.8c where only two crystals exist.

To precisely calibrate the measurements taken, the separation between the interaction zone and the detector must be known, as this determines the position of each ring. To find this, the diffraction pattern from a polysilicon powder reference was captured. As the wavelength of the incident X-ray beam is known, as are the lattice spacings $d_{hkl}$, the angles $\theta_{hkl}$ are easily calculated and by fitting rings to the powder diffraction spectrum, the separation between interaction zone and detector can be easily calculated. An example calibration spectrum is shown in Figure 3.9. The $\langle 1\,0\,0\rangle$ ring is not shown here, as the crystalline substrate is in the $\langle 1\,0\,0\rangle$ orientation, and so any signal from crystals in this orientation will be hidden behind the substrate response. As the detector screen is not perfectly normal to the diffracted rays, the fitted rings are elliptical in shape with the major axis shown by the diagonal red line. With the separation known, the orientation of crystals in subsequent diffraction patterns can be determined, and signals from other sources can be identified and ignored as they will not align with the rings.

### 3.2.3 Cutback Transmission Loss Measurements

The most significant factor in a material's suitability for optical applications is the transmission loss, and one of the driving factors in the projects undertaken in this thesis has been the minimisation of the loss in waveguide structures. Measurements of the

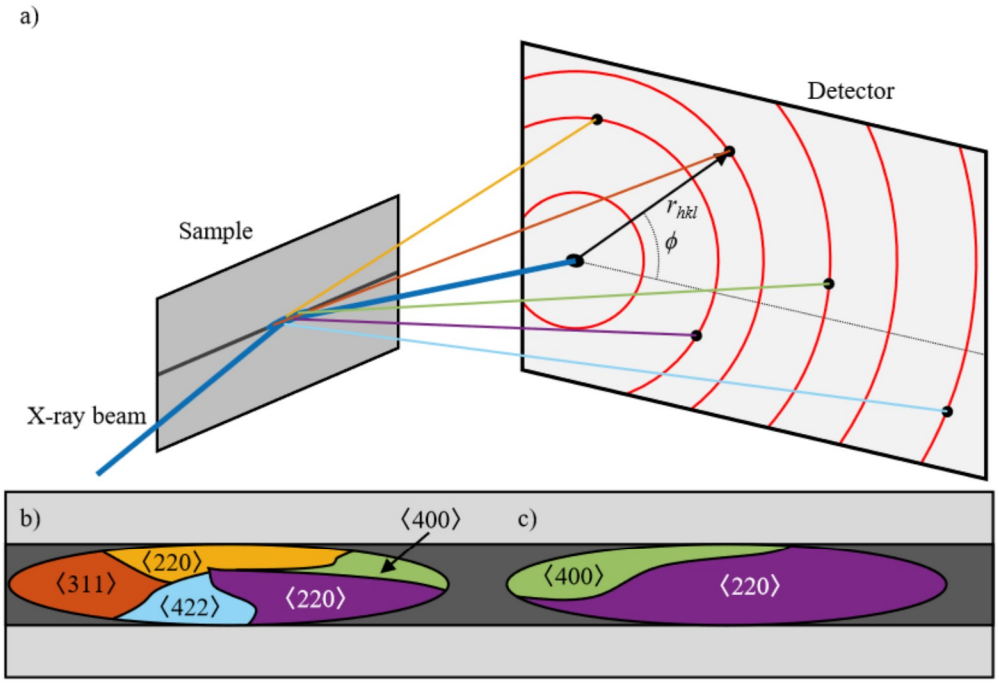


FIGURE 3.8: a) Schematic of the grazing-incidence X-ray diffraction setup, showing diffracted beams incident at different distances from the central beam, indicating multiple crystal grains. The diffracted spots appear at a radius from the central beam $r_{hkl}$ that is dependent on the diffraction angle, and at an azimuthal offset $\phi$ from an arbitrary axis, dependent on the crystal orientation. b) Crystal orientations within the interaction zone for a point with a large number of crystals. c) Interaction zone with few crystals.

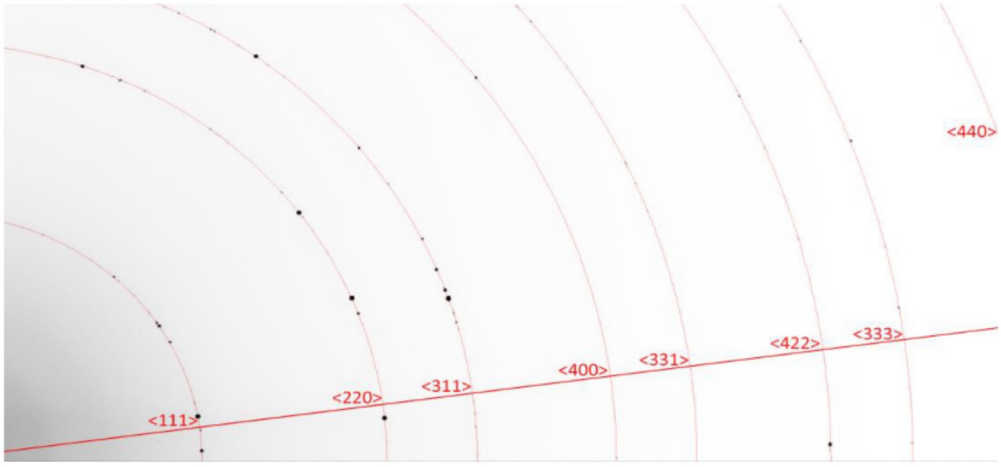


FIGURE 3.9: Calibration pattern from a c-Si powder reference. Dark spots are the diffraction pattern, with fitted rings in red. Diagonal red line shows the major axis of the elliptical rings.

waveguide transmission were carried out by the cutback method, and coupling facets were prepared by cleaving. Here a discussion of these processes is presented, and a

comparison between cleaving and polishing as a means to reduce the waveguide length is made.

#### 3.2.3.1 Transmission Measurement Setup

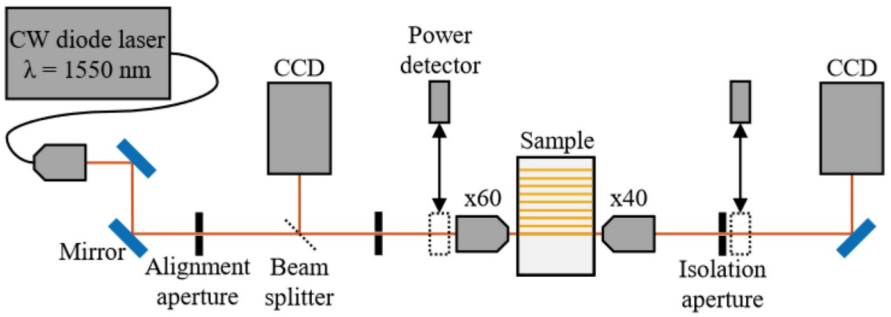


FIGURE 3.10: Setup for measuring transmission losses. CW laser light at 1550 nm is coupled into waveguides. CCD cameras are used to image the input and output facets to monitor coupling, and an isolation aperture eliminates scattered cladding and substrate modes.

Net transmission loss through a waveguide was measured using the setup shown in Figure 3.10. A CW fiber-coupled diode laser emitting at 1550 nm was collimated, and focused onto the input facet of the waveguide using a 60× (0.85 numerical aperture (NA)) microscope objective. The output was collected with a 40× (0.6 NA) objective and directed onto an infrared-sensitive CCD camera to provide preliminary alignment optimisation. The input lens was chosen to maximise the efficiency of the input coupling, while the lower magnification of the output lens made the identification and alignment of the beam easier due to the larger focused spot area. However, this mismatch affects the uniformity of the coupling efficiency at each facet. Ideally, the lenses would be identical, however this proved unfeasible in practice. This was due to the difficulty of locating the waveguide output using the high magnification lens. Back-reflected light from the input was also directed to a CCD using a beam splitter for initial positioning of the input beam. The sample and both objectives were mounted on high-precision three-axis stages (Thorlabs MAX301). At the output, an isolation aperture was used to eliminate scattered light from the substrate and surroundings, leaving only the output profile. Powermeters placed immediately before the input objective and after the isolation aperture were used to measure the input and output powers ($P_{in}$ and $P_{out}$), from which the loss at that length was calculated using

$$\text{Loss} = 10\log_{10}\left(\frac{P_{in}}{P_{out}}\right) \tag{3.5}$$

These measurements were repeated for multiple waveguide lengths, and the transmission ($\text{dB}\,\text{cm}^{-1}$) and coupling losses (dB) were calculated from the gradient and intercept of

the best fit to the plot of loss against sample length. The root mean square error was used to indicate the reliability of the fitting.

#### 3.2.3.2 Facet Preparation

Prior to optical coupling, the input and output facets must be prepared. Two preparation techniques were tested. Mechanical polishing uses fine abrasive powder suspensions to grind down the facet, while cleaving makes use of the tendency of the crystalline substrate to split along atomic planes from a defect point. Each technique, and their respective advantages and drawbacks, is discussed in detail here. However, of these, only cleaving was used where transmission loss measurements were obtained, and so the polishing method is presented for the purpose of comparison.

In mechanical polishing, the sample is mounted onto a jig using a low melting temperature wax adhesive, and this jig holds the sample facet in contact with a flat plate coated with a suspension of aluminium oxide powder. This is shown schematically in Figure 3.11. The powder particle size is reduced over a series of polishing steps, removing material to shorten the waveguide between transmission measurements while also smoothing the facet to minimise scattering.

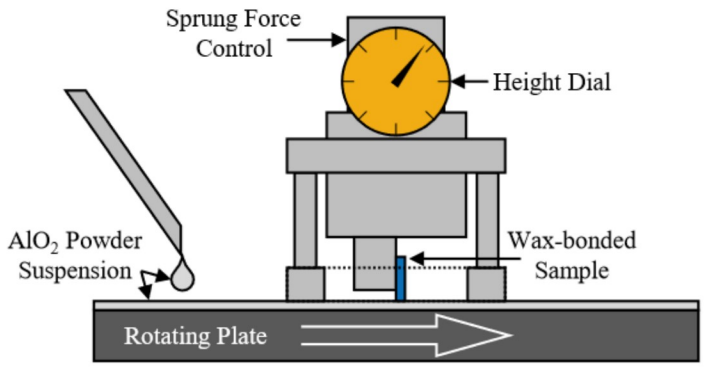


FIGURE 3.11: Jig for mechanical polishing.

This polishing process is commonly used within the optics industry to produce extremely smooth waveguide surfaces. Additionally, the total material removed can be monitored throughout the polishing, and so significant control over the reduction in length of a waveguide is possible. However, numerous issues were encountered while using this technique for facet preparation. The most significant of these was the frequency with which the waveguides were damaged during polishing. Examples of the types of damage are shown in Figure 3.12. It is believed that the source of this damage was the force applied to the sample by the polishing plate lifting the thin film of amorphous material, breaking the waveguides and rendering the sample unusable at any length where this

occurred. Despite attempts being made to optimise the process and limit the occurrence of such damage, the frequency of this was not significantly reduced. Additionally, the polishing process requires mounting the sample onto a polishing jig using a wax adhesive, which must be carefully cleaned to remove residues, and the slow rate of material removal makes polishing a time-consuming process. Future work may benefit from the addition of a silica cladding layer, deposited either before or after the laser crystallisation step. This would serve to generally protect the waveguides from surface impacts and contamination, as well as making the sample as a whole less vulnerable to damage during polishing. This would make the polishing process significantly more viable, and therefore improve the quality of transmission measurements obtained.

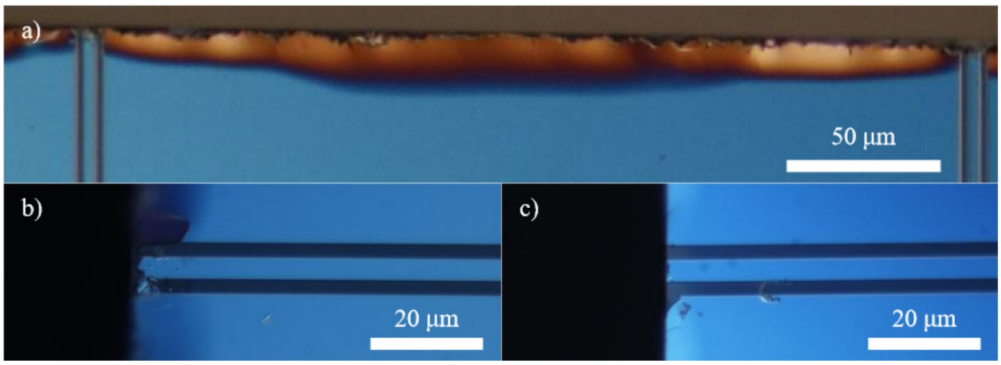


FIGURE 3.12: Polished facet quality of a-Si:H waveguides. a) Differential contrast interference microscopy shows damage to facets of laser-written waveguides. Lifted edges (orange areas) indicate excessive forces applied during polishing. b) Damaged etched waveguide facets prevent free-space coupling. c) Successful polishing results in a high-smoothness waveguide surface.

Cleaving as a method of facet preparation makes use of the tendency of crystalline materials to cleave along a crystal plane. A diamond scribe was used to create a defect in the substrate at the edge of the sample, as shown in Figure 3.13a. Care was taken to ensure that this initial defect did not interfere with any waveguides, as this was seen to be severely detrimental to facet quality. The sample was then placed on a solid surface such as a glass slide, with the defect directly over the edge of the slide and the material to be removed left overhanging, as shown in Figure 3.13b. Gentle pressure was applied evenly to either side of the defect to induce the cleaving. When the pressure is sufficient, the defect acts as a starting location, and the crystalline substrate cleaves along a crystal axis as shown in Figure 3.13c. Due to this tendency, waveguides were fabricated perpendicular to this axis where possible.

The cleaving process is quick, requiring no adhesive preparation. Additionally, the downwards forces applied to the sample avoids the lifting of the upper film, as observed in the polishing approach, eliminating a significant source of damage. However, by comparison to polishing, cleaving offers little precision in the cleaving point, and presents a lower limit to the amount of material that can be removed as there must be sufficient material each side of the induced defect to apply the force to initiate cleaving. In practice,

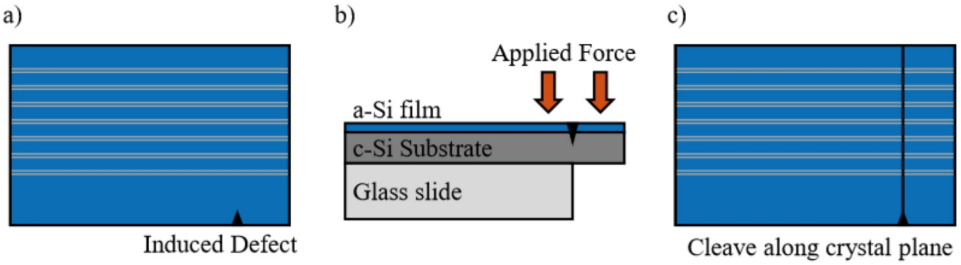


FIGURE 3.13: The cleaving process. a) A defect is induced in the crystalline substrate. b) The defect is placed over a pivot point and force is applied evenly on each side of the defect. c) The defect propagates along a crystalline plane, separating a section of material.

it was found that a reduction in sample length of less than approximately 3 mm resulted in a poor cleave, often failing to run along the intended axis and presenting a rough facet as a result. Additionally, while this proved effective for a-Si waveguides, minor issues arose in polysilicon strip waveguides. The waveguide facet itself often did not perfectly align with the substrate after cleaving, which is believed to be a result of the waveguide cleaving along the crystalline planes of the grains within the waveguide, rather than following the plane of the substrate as the amorphous materials do. This has not been fully investigated due to limitations in experimental time. Figure 3.14 shows example microscope images of a cleaved facet.

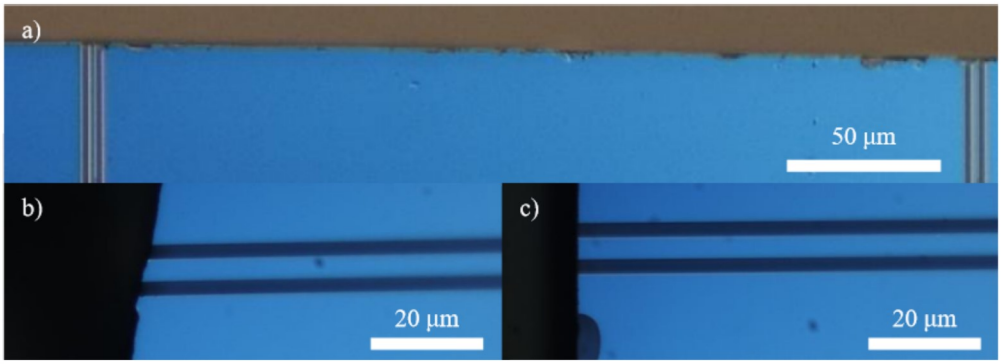


FIGURE 3.14: Cleaved facet quality. a) Differential contrast shows no lifting of the thin film. b) Poor distribution of force during cleaving causes breaking away from the crystal axis. c) Non-abrasive process results in smooth facets in the cleaved plane.

The decision to rely on cleaving for facet preparation was made predominantly on the basis of the high damage rates observed during mechanical polishing. The frequent damage to the waveguides combined with the slow time scale of the process made the collection of sufficient data for transmission measurements rare. By comparison, a relatively high success rate using the quick cleaving process made transmission loss measurements far less time consuming and provided significantly more data.

#### 3.2.3.3 Coupling Error Estimation

Due to high transmission losses (in the range of 30 dB to 50 dB) the exact value of the calculated propagation loss is highly sensitive to the errors associated with the loss measurement process. High facet coupling loss and variable facet quality make exact analysis of this difficult. To determine the reliability of individual transmission measurements, characterisation of the error in the optical coupling process was carried out. However, due to time constraints, the volume of collected data for each waveguide was too small to make valid assessments in the majority of cases. Furthermore, the difference in facet quality between waveguides resulted in significant offsets in total transmission, even in waveguides with nominally similar transmission loss. Therefore, to obtain an estimation of the error in coupling losses, a series of transmission measurements were taken on a single waveguide representative of the reported results, and the resulting error estimation applied to all measurements.

The waveguide used in these measurements was a polysilicon waveguide, fabricated using the techniques described in Chapter 5. The waveguide length was 1 cm, the width 3 µm and height 400 nm. The incident laser power was 285 mW at a stage translation speed of $0.1\,\mathrm{mm\,s^{-1}}$. The sample was removed from the coupling setup between measurements. The results of these measurements are shown in Table 3.2. Calculation of the standard deviation $\sigma$ shows $\sigma = 0.2$ dB, indicating reliable transmission values in the experimental data presented in the following chapters.

| **Input Power** (mW) | **Output Power** (µW) | **Loss** (dB) |
|---|---|---|
| 86 | 8.75 | 39.92 |
| 86 | 9.70 | 39.48 |
| 86 | 9.15 | 39.73 |
| 86 | 8.60 | 40.00 |
| 86 | 9.50 | 39.57 |

TABLE 3.2: Transmission loss measurements with a standard deviation of 0.2 dB.

This value of 0.2 dB has been used throughout this thesis to give an indicative error value in individual transmission loss measurements, unless sufficient data was collected to allow a value to be obtained for that waveguide. Although the errors have been obtained with a polysilicon waveguide, it has been assumed that the calculated standard deviation can also be applied to the a-Si:H structures discussed in Chapter 4, since the error being calculated is independent of the transmission loss. To obtain errors for the transmission loss calculated from the best-fit gradient, the 0.2 dB error is applied to each data point and the steepest and shallowest gradients that fit within the error bars are found. The difference between these and the best fit to the original data is then used to calculate the error in the reported gradient.

It should be noted that the error analysis carried out as described here does not take into account the variation in coupling loss between waveguides or between different lengths of the same waveguide. These variations result from the cleaving process, as described in the previous section. This error was not analysed due to insufficient data being available to make accurate estimations.

# Chapter 4

# Direct Writing of a-Si:H Waveguides and Components

## 4.1 Introduction

This chapter describes the development of an alternative method of waveguide definition in hydrogenated amorphous silicon, using localised laser writing to define the waveguide cladding. The core principle is that the refractive index of polysilicon is lower than that of a-Si:H, allowing the confinement of light in the unprocessed region. The sample deposition is outlined, and the process of fabricating the waveguide structures using this novel technique is described. Then, the experimental work undertaken is explained, starting with the methods of waveguide definition. Simulations used to understand the waveguiding in these structures are then presented. The comparison of this work with conventional lithographically-defined waveguides is detailed, as is the use of Raman spectroscopy to investigate sources of optical loss. Finally, complex structures fabricated by laser writing are presented, to demonstrate the flexibility of the technique.

## 4.2 Background and Concept

Low transmission losses have been observed in low-temperature-deposited hydrogenated amorphous silicon waveguides, with the lowest losses reported by Oo et al. in a-Si:H deposited by HWCVD with a substrate temperature of 230 °C [50]. Propagation losses of $0.8\,\mathrm{dB\,cm^{-1}}$ were recorded in waveguides with dimensions $650\,\mathrm{nm} \times 400\,\mathrm{nm}$. The deposition flexibility, along with its excellent optical characteristics, makes a-Si:H a popular material in photonics research.

Interest in a-Si:H as a waveguiding material for IR wavelengths picked up in the mid-1990s following the demonstration of components such as light-emitting diodes and photodetectors [111], [112], which leveraged the greater suitability of a-Si:H over c-Si for such applications. The first report of telecommunications wavelength guiding by Cocorullo et al. was carried out in integration-compatible material deposited at 200 °C, with measured transmission losses of 0.7 dB cm$^{-1}$ in 15 µm wide waveguides [69]. The low transmission losses in a-Si:H are attributed to the hydrogen passivation of dangling bonds, which are the main source of absorption in pure a-Si.

With the demonstration of 2 dB cm$^{-1}$ losses in single-mode waveguides [67], a-Si:H became a significant contender with c-Si for purely optical applications. Its interest expanded further in the 2010s following reports of strong nonlinear effects at 1550 nm [51]–[53], with a nonlinear coefficient 5 times higher than that of c-Si. Additionally, a-Si:H offers superior deposition flexibility with the capacity for multilayer fabrication, avoiding the integration barriers faced by c-Si photonics.

With observed losses approaching the theoretical bulk limit, attention turned to eliminating losses originating from the waveguides, in particular the scattering at the waveguide upper surface and sidewalls. The as-deposited top-surface roughness in a-Si:H has been reported as low as 1 nm [50], however after etching this has been measured as $> 1.8$ nm [113]. Additionally, the roughness of etched sidewalls has been identified as a source of waveguide loss in c-Si [6], [54], [114], and as the scattering losses are largely material-independent, these conclusions can be applied to any etched waveguide system. Therefore, a method for waveguide definition that avoids the etching process while maintaining low transmission losses would be of significant value.

Laser writing provides a potential method that fulfils these requirements. Martinez-Jiminez et al. demonstrated the use of a CW laser to fabricate complex polysilicon waveguide structures by direct writing [49]. Using an earlier iteration of the laser-writing system shown in Figure 3.4, the localised crystallisation of a pure a-Si film was used to manufacture polysilicon waveguides with losses of 9.3 dB cm$^{-1}$, as well as complex waveguide structures such as ring resonators and Y-junctions which are important elements for photonic circuits. Selective etching of the planar amorphous material was necessary to allow waveguiding in these structures, likely leading to an increased surface roughness and consequently increased loss from surface scattering. Although the recorded losses are significantly higher than in a-Si:H, waveguides, this can be attributed to the presence of defect sites in the polycrystalline structure, which is hard to control when directly writing into planar films.

In his thesis, Dr Yohann Franz discusses the application of a similar laser crystallisation process to a-Si:H films, and notes the out-diffusion of hydrogen during the laser melting stage [79]. This out-diffusion, combined with the crystallisation process itself, has the effect of reducing the refractive index from 3.69 in a-Si:H [50], to 3.46 in polysilicon.

This assumes that the crystalline fraction is high enough to use the refractive index of c-Si when considering polysilicon systems [115]. If the approach of Martinez-Jiminez et al. is inverted, using the low-index polysilicon as the waveguide cladding and the low-loss a-Si:H as the core, the need for etching is eliminated. This would allow the fabrication of complex structures by direct laser writing. The refractive index profile that would be produced is shown in Figure 4.1a, assuming a step-index structure. A schematic cross-section of such a system, assuming the presence of a $SiO_2$ buried oxide (BOX) layer and air upper cladding, is shown in Figure 4.1b.

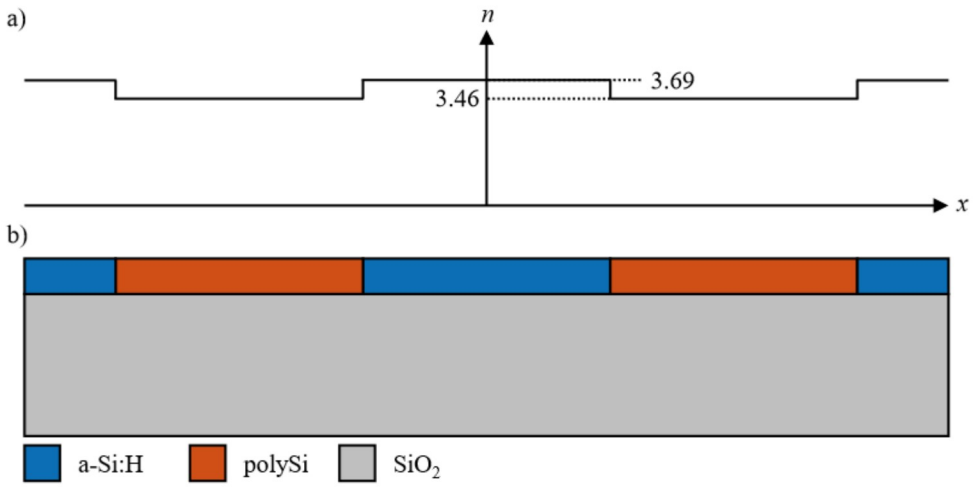


FIGURE 4.1: a) Refractive index profile and b) cross-section schematic of a laser-written a-Si:H waveguide. The low refractive index of the polysilicon cladding ($n = 3.46$) confines light to the a-Si:H core ($n = 3.69$).

By using the high-accuracy computer-controlled laser-crystallisation system previously described, the fabrication of easily-customisable complex waveguide structures in a CMOS-compatible process should be achievable. This chapter will outline the investigation of this premise, describing the fabrication stages, initial proof-of-concept, the comparison of waveguide losses with those from conventional lithographical definition, and the demonstration of complex waveguide structures.

## 4.3 Manufacturing Process

This section outlines the fabrication processes of the a-Si:H waveguides, covering the deposition of the film by HWCVD and the laser writing procedure for straight waveguides and S-bend and Y-junction photonic components.

### 4.3.1 Deposition

To minimise material losses, the deposition of the a-Si:H films followed the process used by Oo et al., who reported transmission losses of $0.8\,\mathrm{dB\,cm^{-1}}$ [50]. Hot-wire CVD with a substrate temperature of 230 °C was used to grow films of thickness 400 nm on a 4.6 µm BOX layer. To ensure complete dissociation of the silane precursor, the filament temperature was 1850 °C. To achieve the desired hydrogen content, the ratio of silane to hydrogen in the precursor gas flow was 2.4:1. Based on previous characterisation of films deposited using these parameters by Oo et al., the rms surface roughness was assumed to be 1 nm, ensuring minimal scattering from the waveguide top-surface. This assumption was made as the deposition was carried out by the same group using the same equipment.

### 4.3.2 Laser Writing

The laser definition of waveguide structures in a-Si:H was realised using the setup shown in Figure 3.4, using a top-down stationary beam focused by a 10×, 0.25 NA objective mounted on a z-axis stage, with the sample held by vacuum clamp to air-bearing x/y stages (Aerotech ABL-1500). Laser writing used the previously mentioned 445 nm and 532 nm lasers. The stages were controlled from a central computer using G-code command scripts and had sub-micrometre positioning accuracy. Additional programs were written to take input parameters and generate the necessary set of G-code commands to fabricate the desired structures. This section will outline the laser writing process, necessary input parameters and additional processing considerations for the fabrication of straight waveguides for cutback transmission loss measurements. More complex components are described later in this chapter, in Section 4.7

In his thesis, Dr Yohann Franz discusses the laser crystallisation of stripes in an a-Si:H thin film [79]. He notes that a significant barrier is presented by the explosive out-diffusion of hydrogen within the film, which occurs as a result of intense heating. Therefore, optimal processing in this manner must balance the laser intensity necessary to crystallise the silicon against this limit beyond which the cladding will be damaged, risking the introduction of scattering points from deposited silicon fragments onto the waveguide core. To determine this threshold, initial optimisation experiments involved the writing of single lines in a-Si:H, recording the power at the sample surface and noting the point at which any sign of damage was observed during subsequent examination by optical microscopy.

Three distinct regimes were observed as the incident power was increased, examples of which are shown in Figure 4.2. The lowest power regime is the desired range, in which the temperature is sufficient to induce crystallisation, but low enough that the thermally-induced out-diffusion of hydrogen is gentle. This produces a central section

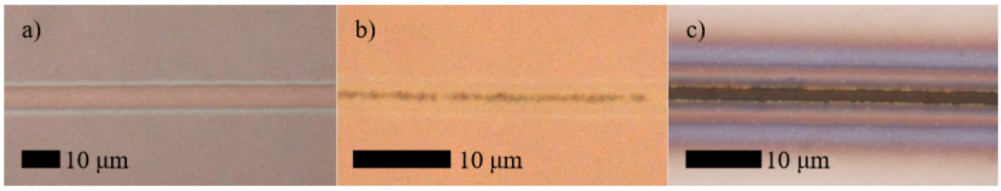


FIGURE 4.2: Laser written polysilicon lines in hydrogenated silicon, showing a) an undamaged line, b) damage due to explosive out-diffusion of hydrogen and c) damage from ablation of the silicon layer.

of the polysilicon stripe, uniform in colour, with the crystallised area clearly visible as seen in Figure 4.2a, and a gentle colour gradient over a 1-2 µm region at either side. The second regime is that in which explosive out-diffusion of hydrogen occurs. The appearance is characterised by uneven and darker patches along the centre of the written stripe, as shown in Figure 4.2b. The final regime, shown in Figure 4.2c, occurs when the incident laser power is sufficient to ablate the a-Si:H film, resulting in significant damage to the surrounding material. As the higher power regimes are detrimental to the material quality, the incident power was kept below the upper threshold for the lowest power regime.

Due to the limit to the power of the incident beam, there is a consequent limit to the crystalline quality of the laser-written tracks. A previous study of CWLA in planar Si films showed that the largest crystal grains are obtained close to the ablation threshold [100], but the requirement of avoiding explosive out-diffusion makes this incompatible with a-Si:H [35]. Therefore, the incident power was kept close to, but below the threshold for hydrogen out-diffusion to maximise grain size as far as possible. As the intensity of light carried in the cladding was expected to be low, the crystallinity is not expected to have a significant impact on waveguide quality.

During the process of identifying the power threshold to avoid damage, it was observed that the width of the crystallised stripe is dependent on the incident laser power and the x/y stage translation speed $v$. Higher incident power increased the volume of material that was heated to the point of crystallisation, while increasing $v$ decreased the energy absorbed by a given volume of silicon, thus reducing the stripe width. The recorded widths from the first waveguide tests are shown in Table 4.1. Due to the minor variations in film thicknesses following deposition, these parameters must be remeasured on each new sample. However, this only requires a small area and is a rapid process.

#### 4.3.2.1 Control Program

To facilitate the fabrication of waveguides with repeatable structures and dimensions, a parameter-based program was written to generate the G-code command script for the three-axis stages. The creation of this script is a multi-stage process. First, the waveguide structure must be defined in terms of the path that the writing laser will follow

| Power (mW) | Scanning Speed ($\mathrm{mm\,s^{-1}}$) 1 | 5 | 10 | 50 |
|---|---|---|---|---|
| 30 | 1.2 | 0.6 | 0* | 0* |
| 40 | 2.6 | 2.5 | 2.0 | 2.1 |
| 50 | 3.4 | 3.3 | 3.4 | 3.0 |
| 60 | 4.0 | 3.4 | 3.2 | 3.1 |

TABLE 4.1: The width (µm) of a crystallised stripe in a-Si:H is dependent on the scanning speed and the incident laser power. In combinations marked *, crystallisation did not occur.

on the sample surface. For straight waveguides this is two parallel lines with a suitable separation. Then, the path must be defined in terms of the user input parameters. For the creation of straight waveguides, five parameters were required. First, the initial and final coordinates of the waveguide core, $A$ and $B$, were selected. Next, the desired stage translation speed $v$ was entered. The width of the laser-written stripe, $w_{\mathrm{LAS}}$, was then added to the desired waveguide width $w_{\mathrm{WG}}$. The sum of these values is the separation $\delta$ between the two laser-written paths that become the waveguide cladding. The offset from the waveguide path is $\sigma = \delta/2$. Figure 4.3a shows how these parameters relate to the final structure. A program was then written to convert the user input parameters into the coordinate-based G-code language, creating a script which controls the stages such that the focused laser beam will, at a constant speed $v$, follow the path shown in Figure 4.3b. First, a straight path from $A + \sigma$ to $B + \sigma$ is written, then the sample is moved sideways by a distance $\delta$ and follows a second path, parallel to the first, from $B - \sigma$ to $A - \sigma$.

## 4.4 Numerical Modelling

Simulation of the confinement of optical modes in the manufactured waveguides was carried out using COMSOL Multiphysics, a numerical finite-element modelling software. A simplified waveguide cross-section (shown in Figure 4.4) was used, assuming sharp, well-defined boundaries between polysilicon and a-Si:H. Simulations for wide and narrow waveguides were calculated, with widths assumed to be 2 µm and 5 µm.

Using the inbuilt electromagnetic wave frequency domain solver, the supported modes were calculated. Figure 4.5 shows the three best-confined modes for the 5 µm (a-c) and 2 µm (d-f) structures. The arrows show the direction of the electric field, indicating preferential guiding of the TE mode, which results from the increased scattering from the upper surface of the waveguide. As the best confinement (indicated by the higher effective index $n_{\mathrm{eff}}$) is seen in the fundamental $\mathrm{TE}_{00}$ mode, the lowest propagation losses will be obtained when light is coupled into the fundamental mode, so care must be taken to do this during experimental work. In particular, coupling into higher order modes

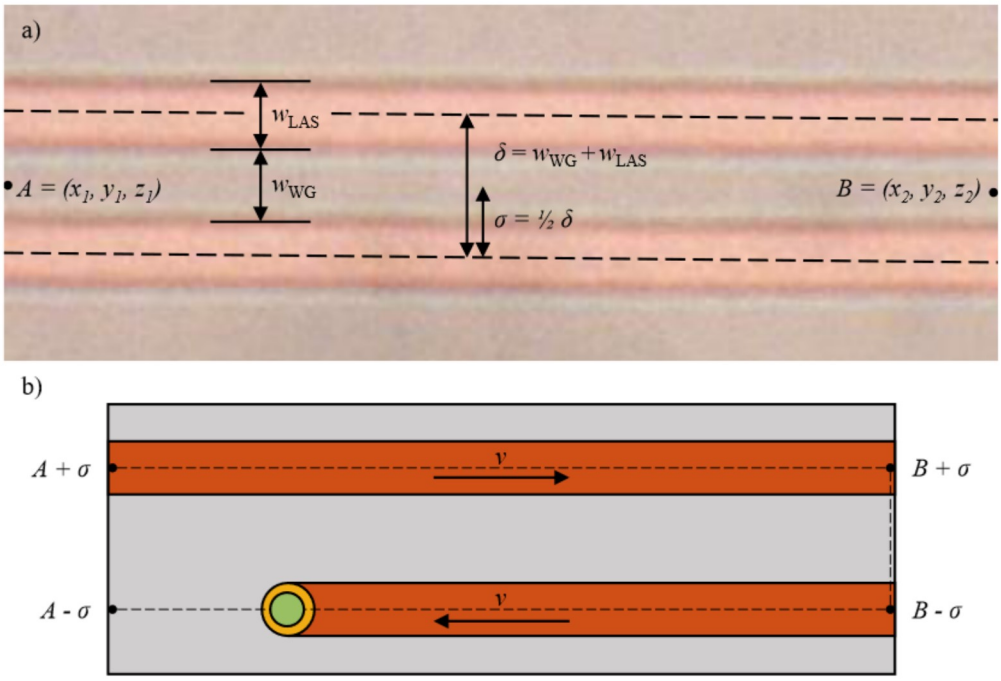


FIGURE 4.3: For straight waveguides in a-Si:H defined by laser crystallisation, a) the relation between the final structure and the input parameters, and b) the path of the laser beam across the sample surface.

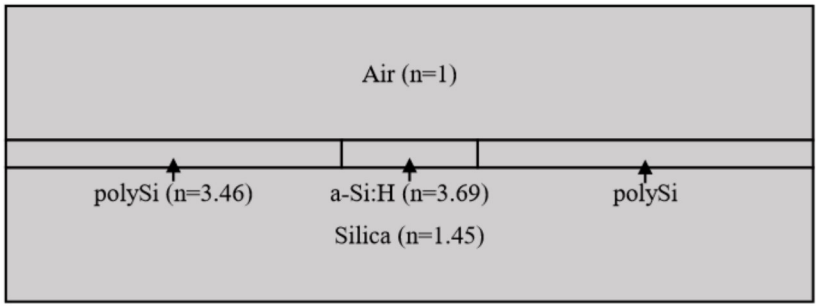


FIGURE 4.4: Geometry used for numerical simulations of waveguiding in laser-defined a-Si:H waveguides. The deposited layer is 400 nm thick, and the air and silica BOX layers are 2 µm thick.

would be detrimental to waveguide performance due to the higher relative intensity near the core/cladding interface.

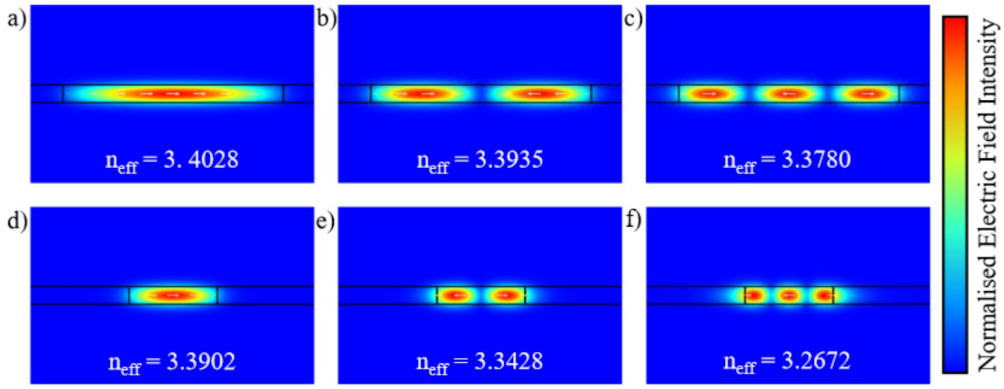


FIGURE 4.5: Simulated guided modes in waveguides written with widths of a-c) 5 and d-f) 2 microns. Arrows show the electric field orientation.

## 4.5 Transmission Losses

To determine the quality of waveguides manufactured using laser writing, transmission losses were measured by the cutback process. Additionally, the losses in lithographically defined waveguides of comparable dimensions were recorded to provide a baseline against which the results of the new technique were compared. In this section, the reference measurements are presented, followed by the results from laser-defined waveguides fabricated using two different laser sources. The first was a Roithner LaserTechnik ULV-445-700, a CW diode laser emitting at 445 nm. The second was an IPG GLR-10W CW fiber laser emitting at 532 nm. The laser source was changed to improve laser stability and beam quality, and to increase the accessible power range for other applications.

### 4.5.1 Lithographic Reference

Following the method in Section 4.3.1, a 400 nm layer of a-Si:H was deposited on a 5 µm $SiO_2$ BOX layer for optical isolation. Conventional electron-beam lithography was then used to define waveguides with widths of 2, 3 and 4 µm. Transmission loss measurements were then taken on these waveguides at a wavelength of 1.55 µm using the cutback method. Due to issues previously discussed in Section 3.2.3.2, the facets were prepared by mechanical cleaving. The lowest recorded losses were $(4.31 \pm 0.76)\,\mathrm{dB\,cm^{-1}}$ in a 2 µm waveguide, $(4.94 \pm 0.83)\,\mathrm{dB\,cm^{-1}}$ in a 3 µm waveguide and $(8.47 \pm 0.98)\,\mathrm{dB\,cm^{-1}}$ in a 4 µm waveguide, as shown in Figure 4.6. The highest losses being in the widest waveguides is counter to expectations, as linear loss is typically inversely proportional to width [42]. However, the facet quality from cleaving is subject to some inconsistencies as previously discussed, and this may contribute to artificially high measured losses if the quality of the output facet at a given length is either significantly better or worse than for other lengths at which the waveguide loss is measured. Therefore, a more comprehensive investigation should be undertaken before conclusions are drawn from

this data. These losses are also significantly higher than the $0.8\,\mathrm{dB\,cm^{-1}}$ previously reported in a-Si:H [50], however an investigation into the cause of increased loss was not part of this study.

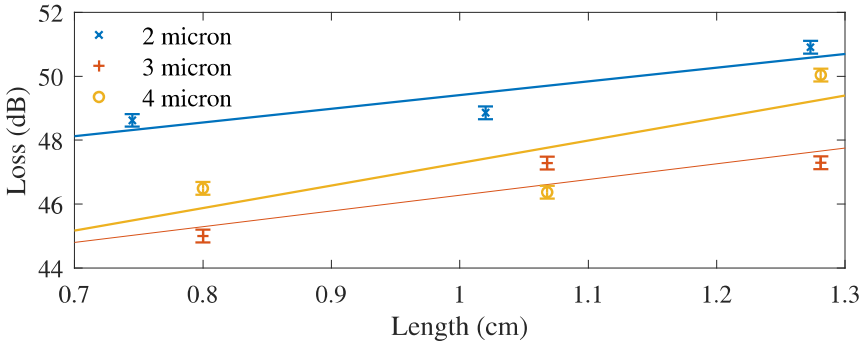


FIGURE 4.6: Lowest recorded losses in lithographically-defined a-Si:H waveguides with widths of 2 µm ($(4.31 \pm 0.76)\,\mathrm{dB\,cm^{-1}}$), 3 µm ($(4.94 \pm 0.83)\,\mathrm{dB\,cm^{-1}}$) and 4 µm ($(8.47 \pm 0.98)\,\mathrm{dB\,cm^{-1}}$).

### 4.5.2 Initial Laser Writing

Straight waveguides were fabricated in three sets, with core widths of 2, 4 and 6 µm. The incident laser power was set to 50 mW, and the laser source used was a 445 nm CW diode laser (Roithner LaserTechnik ULV-445-700). Three waveguides were made at each width, and the facets were prepared by cleaving. The cleaving process was chosen over the conventional polishing process due to the frequent damage, described in more detail in Section 3.2.3.2. Transmission at 1550 nm was observed in seven waveguides: all 2 µm and 4 µm, and one of the 6 µm structures, with the total losses in the range 42 dB to 49 dB at a sample length of 1.362 cm. Successful transmission loss measurements were obtained for four waveguides: all 2 µm wide waveguides and one 4 µm, with the results shown in Figure 4.7. Figure 4.7a shows the averaged transmission of the three 2 µm waveguides, with the error bars corresponding to the standard deviation of the transmission measurements for the three waveguides. The calculated loss was $(8.5 \pm 3.7)\,\mathrm{dB\,cm^{-1}}$. The high error is thought to have arisen from the varied facet quality previously discussed, however the individual waveguide transmission and coupling losses were similar enough to allow for error analysis using the raw data. The loss from the 4 µm was $(4.46 \pm 0.84)\,\mathrm{dB\,cm^{-1}}$, as shown in Figure 4.7b, using errors of 0.2 dB. Two data points were obtained for the 6 µm waveguide, indicating $2.2\,\mathrm{dB\,cm^{-1}}$, however facet damage prevented light output at the third length and so this cannot be confirmed.

Although the losses obtained here are significantly higher than the $0.8\,\mathrm{dB\,cm^{-1}}$ reported by Oo et al. [50], transmission losses below $5\,\mathrm{dB\,cm^{-1}}$ in preliminary investigations

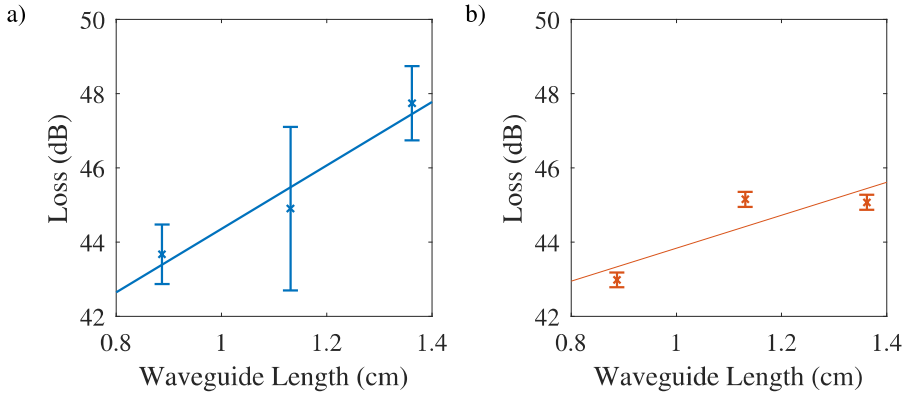


FIGURE 4.7: Transmission loss measurements in proof-of concept a-Si:H waveguides defined by laser-crystallisation of polysilicon cladding. Waveguides fabricated with core widths of a) 2 µm and b) 4 µm suggest that transmission loss is inversely correlated with waveguide width.

suggest that lower losses may be obtained following optimisation of crystallisation conditions and waveguide geometries. The calculated losses in these waveguides are inversely proportional to the waveguide width, however due to the high errors and low volume of data this cannot be confirmed. If further data matches this trend, as would be expected as this aligns with theory [42], it would suggest that the interaction between the guided mode and the laser-written cladding boundary has a greater effect on the transmission loss than the interaction between the mode and the upper and lower surfaces of the waveguide. Most significantly, the lowest loss is comparable with that obtained from lithographically-defined waveguides, indicating that the material quality is relatively consistent between samples, and that loss from the interface between the core and cladding is roughly equivalent to the loss from etched sidewalls. However, as these losses were observed in 4 µm wide laser written waveguides and 2 and 3 µm etched waveguides, the losses from etched sidewalls may be slightly lower. It was therefore anticipated that waveguides fabricated by laser writing using an improved laser source would exhibit lower losses. Such lower losses would, if observed, demonstrate the viability of this technique. The anticipated benefits of the improved laser writing conditions were a higher crystalline fraction and larger crystal grains in the polysilicon cladding, minimising losses from scattering and absorption.

### 4.5.3 Comparison to Lithographical Reference

Although the propagation losses in these initial laser-written waveguides are almost equivalent to those in the etched reference sample, the materials in which the waveguides were fabricated were not guaranteed to be identical, despite the deposition conditions being the same. Therefore, following the aforementioned change of laser source in the writing setup, laser crystallisation experiments were carried out in material deposited

simultaneously to and in the same deposition chamber as the lithography sample. This ensured that the material quality, surface roughness, hydrogen content and film thickness were all identical. Therefore, any difference in measured transmission losses can be attributed wholly to the different fabrication methods.

Due to the change in laser source, the testing of power thresholds was redone by annealing single lines at a series of increasing incident powers, at multiple scanning speeds. The widths of these lines were measured to ensure that waveguides of the desired widths could be written, as explained in Section 4.3.2. The incident power damage threshold was identified as 100 mW for both 0.1 mm s$^{-1}$ and 1 mm s$^{-1}$. Test waveguides of approximate length 1 cm with a consistent width of 4 µm were then fabricated in one section of the unpatterned chip and the total transmission was measured. The results of these optimisation tests are shown in Table 4.2.

| **Speed** (mm s$^{-1}$) | **Power** (mW) | **Loss** (dB) |
|---|---|---|
| 0.1 | 40 | 36.7 |
| | 50 | 35.2 |
| | 60 | 32.8 |
| | 70 | 34.9 |
| | 80 | 27.6 |
| | 90 | 39.6 |
| | 100 | 35.8 |
| 1 | 30 | 38.9 |
| | 40 | 38.6 |
| | 50 | 38.4 |
| | 60 | 39.9 |
| | 70 | 39.9 |
| | 80 | 36.3 |
| | 90 | 39.8 |
| | 100 | 38.2 |

TABLE 4.2: Transmission measurements of laser-defined 4 µm waveguides to determine best crystallisation parameters. Lowest losses were observed with stage speed 0.1 mm s$^{-1}$ and incident power 80 mW.

The lowest losses at both 0.1 mm s$^{-1}$ and 1 mm s$^{-1}$ were measured in waveguides written with incident power 80 mW. At all tested powers, transmission was greater with annealing at 0.1 mm s$^{-1}$ than for equal power annealing at 1 mm s$^{-1}$. Some minor instability in the stage translation at higher speeds was noticed, resulting in a 'wavy' structure as shown in Figure 4.8. It is thought that this caused the higher losses from higher annealing speeds, however this was not confirmed.

Imaging of the waveguide outputs suggests that scattering from the waveguide core into the cladding causes some of this loss. Figure 4.9 shows the infra-red camera outputs for waveguides written at four different parameter sets. Significant scattering into the cladding occurred in 50 mW tests, seen as scattering along the material plane to either

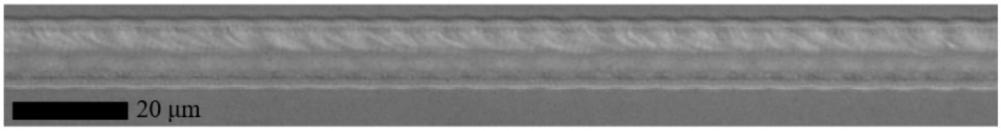


FIGURE 4.8: Periodic oscillations in the beam position relative to the sample surface cause an uneven structure in the laser-crystallised stripes, likely increasing scattering loss during propagation.

side of the output spot. Slight scattering was seen in the 80 mW, 0.1 mm s$^{-1}$ output, suggesting that lower losses may be obtained if confinement can be improved.

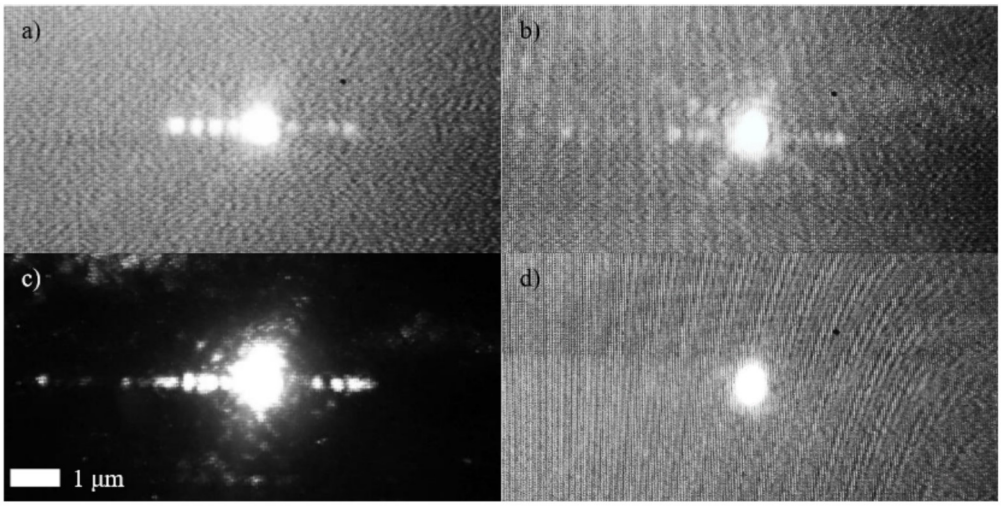


FIGURE 4.9: Infra-red camera images of light at the output facet of waveguides written at a) 0.1 mm s$^{-1}$, 50 mW, b) 0.1 mm s$^{-1}$, 80 mW, c) 1 mm s$^{-1}$, 50 mW, d) 1 mm s$^{-1}$, 80 mW. Cladding-guided light is seen in a)-c).

As the highest transmission was observed with 0.1 mm s$^{-1}$ writing speed, but end-facet observations indicate best light confinement with 1 mm s$^{-1}$, both speeds were used for fabrication of the waveguides for comparison measurements. Laser writing was used to fabricate waveguides with widths of 2, 3 and 4 µm with incident power of 80 mW and speeds of both 0.1 and 1 mm s$^{-1}$. Cutback loss measurements were carried out on these, the results of which are shown in Table 4.3. Although transmission was observed through 2 µm laser-written waveguides, the unreliability of the cutback method prevented complete measurements from being obtained, as no output was achieved at multiple sample lengths. Of the waveguides where complete measurements were obtained, the lowest loss was $(10.74 \pm 1.39)$ dB cm$^{-1}$ in a 4 µm waveguide written at 0.1 mm s$^{-1}$, shown in Figure 4.10.

These losses are significantly higher than those obtained in either the lithographically-defined baseline sample or the initial proof-of-concept work, suggesting that the changes to the laser source did not result in the anticipated improvement in waveguide quality.

| **Width** (µm) | **Writing Speed** ($mm\,s^{-1}$) | **Loss** ($dB\,cm^{-1}$) |
|---|---|---|
| 3 | 0.1 | $14.58 \pm 0.96$ |
| 4 | 0.1 | $15.55 \pm 1.39$<br>$10.78 \pm 1.39$ |
| 4 | 1 | $19.35 \pm 0.49$<br>$14.27 \pm 1.07$<br>$14.12 \pm 0.93$ |

TABLE 4.3: All losses obtained from laser-written waveguides fabricated with the IPG GLR-10W laser.

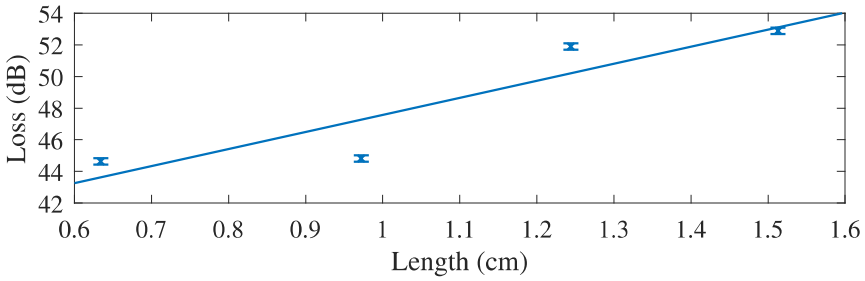


FIGURE 4.10: Lowest loss ($(10.78 \pm 1.39)\,dB\,cm^{-1}$) from the laser-written a-Si:H waveguides fabricated with the IPG GLR-10W laser.

This in turn indicates an incomplete understanding of the crystallisation and loss mechanisms relevant to this novel structure, warranting further investigation into these. The primary question concerns the sources of loss, expected to be scattering and absorption in the transition region from the polysilicon cladding to the a-Si:H core. The process of CWLA in planar silicon films is known to produce larger crystal grains at higher incident power, but the studies investigating this have been primarily concerned with the crystallinity at the centre of the crystallised region. In this work, the behaviour at the outer extent of the laser-annealed track is of greatest significance, as these have the greatest interaction with the guided mode. The crystal sizes in this area are typically small, due to the change in crystallisation dynamics from liquid-phase to solid-phase crystallisation as the temperature decreases further from the laser focus point. SPC typically results in crystal grain sizes below 1 µm, resulting in high losses. However, the gradual increase in grain sizes may result in the waveguiding dynamics being more comparable to those of a graded-index system than the step-index profile used for confinement simulations. This may increase the interaction between the mode and the high-loss material, adversely impacting waveguide performance. It may therefore be advantageous to carry out laser processing on these systems at lower power, ensuring SPC occurs across the entire laser track and improving consistency of the crystallinity across the cladding areas. Alternatively, the same benefits may be achievable with a top-hat beam profile giving a more uniform heat distribution. It may be possible to obtain larger grains in the cladding by

using multiple exposures to write the cladding, using a low-power exposure to induce non-destructive hydrogen out-diffusion and then growing large crystals with a second, higher power exposure. These process refinements were not investigated due to time constraints, but are left as a guide for suggested avenues of further work.

## 4.6 Material Characterisation

The primary sources of transmission loss in these waveguides were anticipated to be the dehydrogenation of previously passivated dangling bonds due to thermally-induced hydrogen out-diffusion in the core and scattering in microcrystalline polysilicon in the transition region between core and cladding. It is therefore important to understand the extent of the crystallisation, as well as to check the presence of hydrogen in the waveguide core. Preliminary estimations of the waveguide viability were obtained using Raman spectroscopy, assessing the change in crystallinity and hydrogen content in the material across the laser written lines. Sequential Raman spectra were taken along a line perpendicular to the waveguide, as shown in Figure 4.11, recording the signal strength at each point of the polysilicon peak, in the range of $510\,\mathrm{cm}^{-1}$ to $520\,\mathrm{cm}^{-1}$, and the amorphous Si-H bond, which has a peak position of $\sim 2000\,\mathrm{cm}^{-1}$.

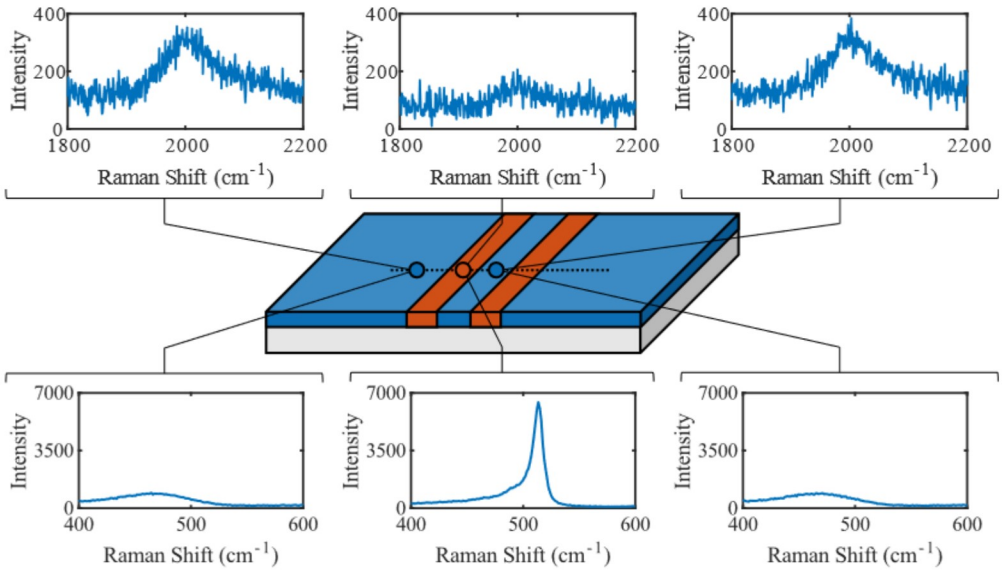


FIGURE 4.11: Intensities of the Si-H $2000\,\mathrm{cm}^{-1}$ (top) and Si-Si $520\,\mathrm{cm}^{-1}$ (bottom) Raman peaks across a laser-defined waveguide in hydrogenated amorphous silicon. High content in both core (blue, inner) and bulk (blue, outer) indicates hydrogen out-diffusion has not occurred, while low content in the cladding (orange) results from thermal out-diffusion.

The laser-annealed cladding is marked by a decrease in the hydrogen content, and the hydrogen content in the core can be compared to the baseline as-deposited concentration

outside the processed area. The hydrogen content at each investigated point was evaluated by measuring the intensity of the Si-H peak, and comparison was made between all points across the waveguide. The intensity of the polySi peaks were also compared across the waveguide. It was anticipated that the Si-H peak would not be present in the waveguide cladding where the polySi peak is strongest, and that it will return to its full intensity within the waveguide core. Similarly, the polysilicon peak was only expected to be present in the laser-written stripes, and will return to the bulk amorphous level in the core. However, as the boundary between the amorphous core material and the crystalline cladding will not be sharp due to the Gaussian shape of the processing beam, it was expected that there will be an effective minimum waveguide width, below which the core will remain amorphous but will be dehydrogenated by the lateral conduction of heat in the Si film.

To investigate the change in material composition, waveguides were written with incident power 80 mW, speed 0.1 mm s$^{-1}$ and widths of 2 µm and 5 µm. The widths were confirmed by optical microscopy, and Raman spectra were captured at a series of points across the waveguides with a separation of 1 µm. The intensities of the Si-Si and Si-H peaks were evaluated along these cross-sections using a Matlab script. For each point, the peaks were fitted with a Voigt profile as described in Section 3.2.1. The fitted Voigt peaks were integrated between the points at which the peak intensity dropped to $1/e^2$ of the maximum. If the peak was broad and weak enough that the intensity did not decrease to that extent in the selected data range, it was assumed that there is no peak present. The intensities were then normalised to aid in comparison, as the Si-Si peak exhibits a significantly stronger signal than the Si-H peak. The resulting cross-sections are shown in Figure 4.12.

These cross-sections support the prediction that losses in these waveguides are most likely to occur in the transition region between the polysilicon cladding and a-Si:H core. At both widths, there is a section $\sim 3$ µm across at each border of the crystallised paths in which the material has not been fully crystallised, but thermal out-diffusion of hydrogen has occurred. Therefore, dangling bonds still exist, however they are no longer passivated and will therefore contribute to absorption losses. When comparison is made to the mode simulations shown in Figure 4.5, it can be seen that there is a non-negligible proportion of the electric field in these regions. Additionally, the intensity of the Si-H bond in the core of the 2 µm waveguide is seen not to return to the level seen in the untreated film, unlike in the 5 µm waveguide where a plateau is observed. This indicates that the suggested minimum width of a waveguide manufactured by this process should greater than 2 µm, as this reduced H content will increase transmission losses across the entire waveguide core, rather than only at the edges of the mode.

In narrow waveguides, the low hydrogen content in the waveguide core indicates high transmission loss as the dangling bonds in amorphous silicon are no longer passivated, while losses in wider waveguides are expected to be lower as there is a region several

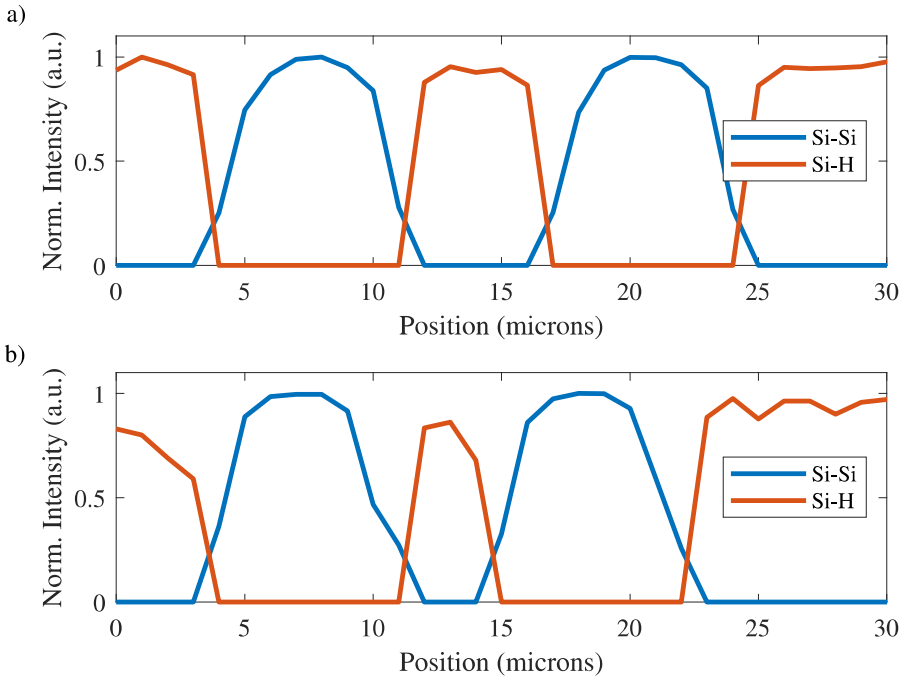


FIGURE 4.12: Raman intensities of the amorphous Si-H and polycrystalline Si-Si peak across a) a 5 µm laser-defined waveguide and b) a similar 2 µm waveguide.

microns across in which the H content is unaffected. This is consistent with loss measurements carried out on these structures, indicating that the predicted sources of loss, absorption and scattering, are correct.

To determine the uniformity of the crystallised tracks, the Lorentzian FWHM of the polySi peak was calculated for points across the laser-written cladding. The FWHM indicates the crystalline quality as the presence of amorphous material broadens the peak due to the increased variation in bond length. The FWHM was expected to be higher at the extremes of the crystalline area and lower at the centre due to the increased temperature at the centre of the crystalline volume during laser writing, which influences grain growth, as discussed in Section 2.2. Figure 4.13 shows the change in polySi FWHM across an arbitrarily selected section of a crystallised track.

This shows that the material properties of the polysilicon tracks are as expected, with a consistent material quality across the central region, with a FWHM of $\sim 4.25\,\mathrm{cm}^{-1}$, and that the amorphous fraction increases at either side. The difference between the polysilicon and c-Si reference in the track ($\Delta_{\mathrm{FWHM}} \approx 1.55\,\mathrm{cm}^{-1}$) suggests that the crystals are small, as the peak is broadened by the amorphous fraction while still being clearly associated with the $\sim 520\,\mathrm{cm}^{-1}$ crystalline peak shift and not the $\sim 480\,\mathrm{cm}^{-1}$ amorphous peak. A similar material structure to this was observed by Martinez-Jiminez et al., in their work on direct laser writing in planar a-Si [49]. Due to the unavailability of facilities, no selective etching was undertaken on these samples, however such investigation

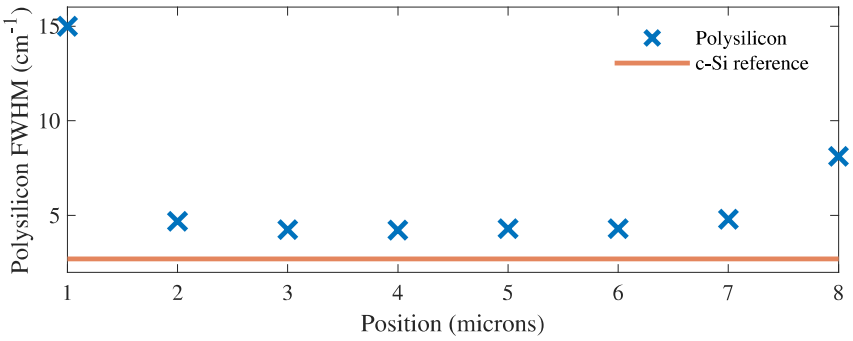


FIGURE 4.13: Polysilicon Lorentzian FWHM across a laser-written track compared to the 2.7 cm$^{-1}$ FWHM of a crystalline reference.

of the material structure of the transition regions may give valuable insight into how crystallinity might be improved in these areas.

## 4.7 Complex Patterning

To study the use of the laser-definition process for the more complex structures that are common to photonic systems, S-bend waveguides and Y-junctions were fabricated with a range of dimensions. As the lowest transmission measurements were seen in waveguides written at 0.1 mm s$^{-1}$ with incident power 80 mW and waveguide width 4 µm, these parameters were used for the laser crystallisation process.

Similarly to the straight waveguides, a program was created to automatically generate G-code scripts for the complex structures. The process flow for writing these programs is shown in Figure 4.14, with details specific to each structure described in the following sections. The waveguide structure must be defined, then the intended laser spot path must be broken down into simple geometric components. For S-bend structures, this consists of straight lines, mostly in either the positive or negative $y$-direction, and semicircular sections, written either clockwise or anticlockwise. For Y-junctions, the more complex structure requires the calculation of the angle to be swept by the circular motion. Then, each component is defined in terms of appropriately selected user input parameters, which must also accommodate the limitations of the fabrication process such as the known laser spot size as discussed in Section 4.3.2.1. A pseudocode is written, outlining which component is to be defined in what order, and what input information is needed for the relevant G-code command. This is then converted into a fully functional code, which is tested digitally and then by fabricating a sample waveguide to check for errors.

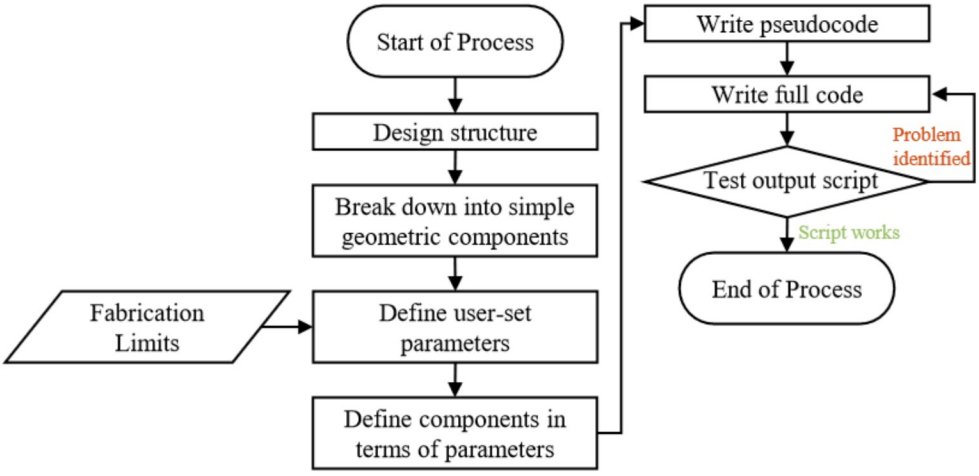


FIGURE 4.14: Flowchart showing the process of creating the program to auto-generate G-code scripts.

### 4.7.1 S-Bend Waveguides

In order to assess longer lengths, bending losses and more complex structures, a double S-bend structure was used as shown in Figure 4.15a, with the structure broken into nine distinct sections. A number of different total length waveguides were created on each sample as indicated in Figure 4.15b. To define the laser paths, a program was created requiring six input parameters. This follows a largely similar principle to the straight waveguide writing process described in Section 4.3.2.1. The first four variables, similarly to the straight waveguides described above, are the coordinates of points A and B, the laser track width $w_{\mathrm{LAS}}$ and the waveguide core width $w_{\mathrm{WG}}$. The additional parameters are the desired bend radius $r$ of the semicircular sections and the added length relative to a straight waveguide between points A and B. In order to simplify the program, the nominal positions of sections $S_1$, $S_2$, $S_8$ and $S_9$ were kept fixed. Actual positions for the two laser tracks for each guide were dependent on the desired core width and measured laser track width as for the straight guides above. The total waveguide lengths were changed by increasing lengths $S_3$, $S_5$ and $S_7$, thus increasing the separation of $S_4$ and $S_6$, and waveguides with 2 mm length increments were created. Nominal bend radii of the core were kept the same on all 4 semi-circular bends. However, the radii for the two laser paths either side of the core around these bends were dependent on the core width and laser track width, these defined by $r_{\mathrm{inner}} = r - \sigma$ and $r_{\mathrm{outer}} = r + \sigma$, as shown in Figure 4.15c. These parameters were then used to generate CNC code for controlling the stage movement. It should be noted that this structure has a minimum additional length compared with a straight A to B waveguide, when $S_3$ and $S_7$ are zero length and $S_5$ is reduced accordingly. For $r = 100\,\mu\mathrm{m}$ this is $\sim 1.7\,\mathrm{mm}$.

Initial S-bend structures were written with a bend radius of 20 µm, this having been chosen as bends of this approximate size are common in silicon photonics [40], [116]. A

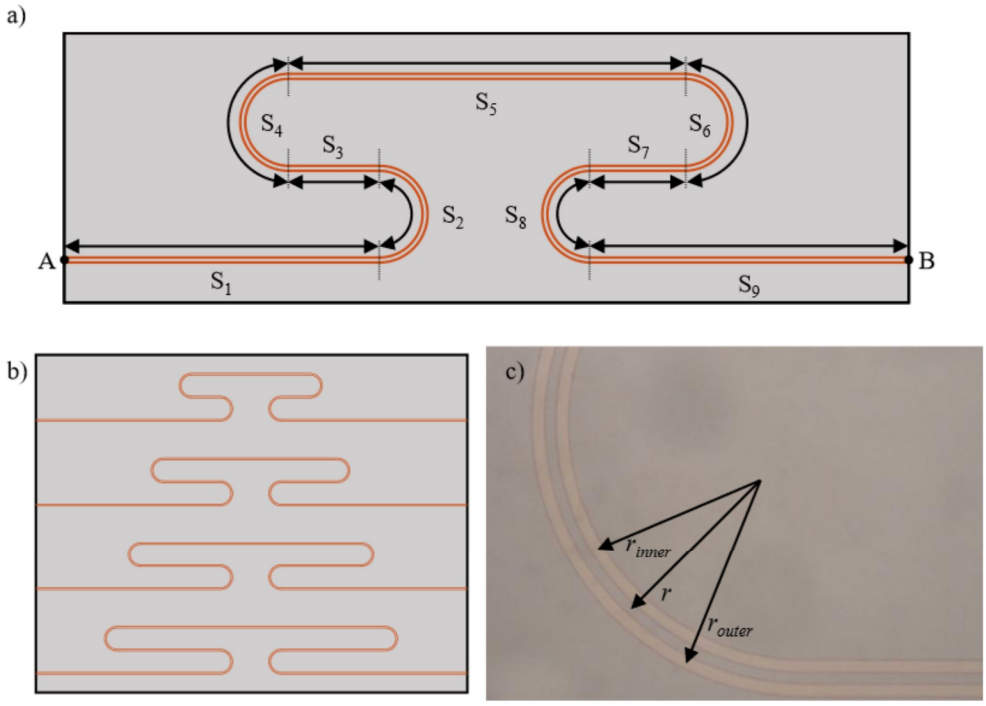


FIGURE 4.15: a) An S-bend waveguide structure broken down into distinct sections. The radius of the semicircular sections is kept constant across a set of waveguides, to ensure that the bending loss contribution is constant. b) The total waveguide length can be changed by increasing the separation of $S_4$ and $S_6$. c) To fabricate bends, the waveguide bend radius $r$ is used to calculated the radii of the inner and outer cladding, $r_{\text{inner}}$ and $r_{\text{outer}}$. The background image is of a fabricated waveguide bend.

microscope image of one such bend is shown in Figure 4.16a. However, no transmission was observed through these, attributed to the narrow bend radius and the low refractive index contrast between a-Si:H and polysilicon ($\Delta = 6.5\%$) compared to that between silicon and air ($\Delta = 70\%$). S-bends with a larger radius of 100 µm were fabricated with added waveguide lengths of 2, 4, 6, 8 and 10 mm, and transmission measurements attempted. Sections of the shortest of these waveguides are shown in Figure 4.16b. These also showed no transmission, although some light was seen to be guided in the planar film. This is assumed to result from two main factors. The first of these is the bend radius. Extrapolation of data presented by Okamoto [117] indicates that for a refractive index contrast of 6.5%, a 750 µm bend radius is the approximate cutoff for low bending losses, and so future work should use waveguides with these dimensions. However, this is large enough that high-density photonic components are likely not feasible in this material. More accurate calculation of the minimum bend radius would also be possible using commercial mode-solver programs. To make accurate simulations of this, greater detail of the waveguide structure would likely be required, as previously discussed. The second cause of loss is thought to be increased scattering and absorption at the core-cladding interface in the bend sections of the waveguide. This is based on the results of Raman spectroscopy measurements as discussed in Section 4.6.

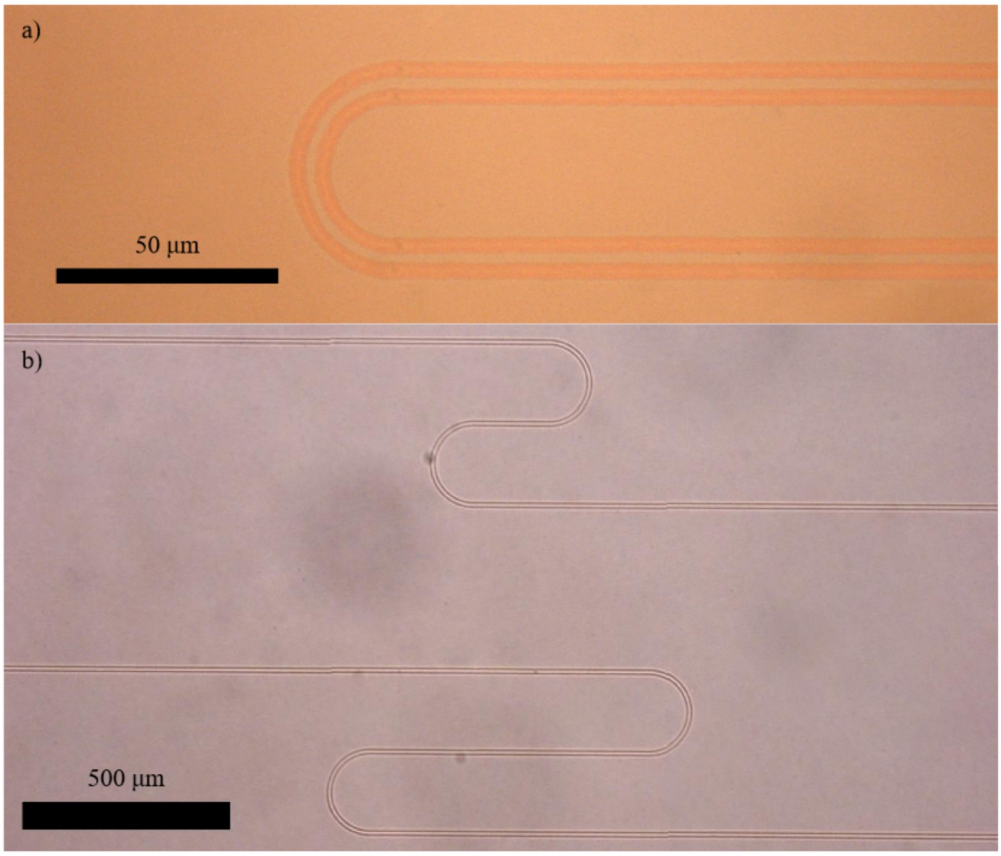


FIGURE 4.16: a) A curved section of a 20 µm bend radius s-bend waveguide. b) S-bend structures with a 100 µm bend radius, demonstrating the addition of waveguide length by increasing the separation of the bends.

### 4.7.2 Y-Junctions

The final structure, a Y-junction, requires several parameters that differ from those of the previous waveguides. The 'start' and 'end' points $A$ and $B$ are still used, however the Y structure splits the waveguide into two channels and so $B$ is chosen at the central point between these. The shape of the junction itself is defined, in addition to the waveguide width and the crystallised path width, by three primary parameters, which are shown in Figure 4.17. The first of these is the final separation of the two arms of the splitter, designated $h$, the second is the total length of the junction structure $l$, and the third is the radius $r$ of the curved sections of the splitter. With these set, the remaining variables such as the arc angle $\theta$ are derived. When creating the 'point' at the inside of the junction, care must be taken to ensure that the stages change direction at the correct position, avoiding blocking the second junction arm. Additionally, the 'blunt' divider at the connection results from the circular heating profile and may be disadvantageous to light guiding.

Y-junctions were created with arm separations of 50 µm, 75 µm and 100 µm, a bend

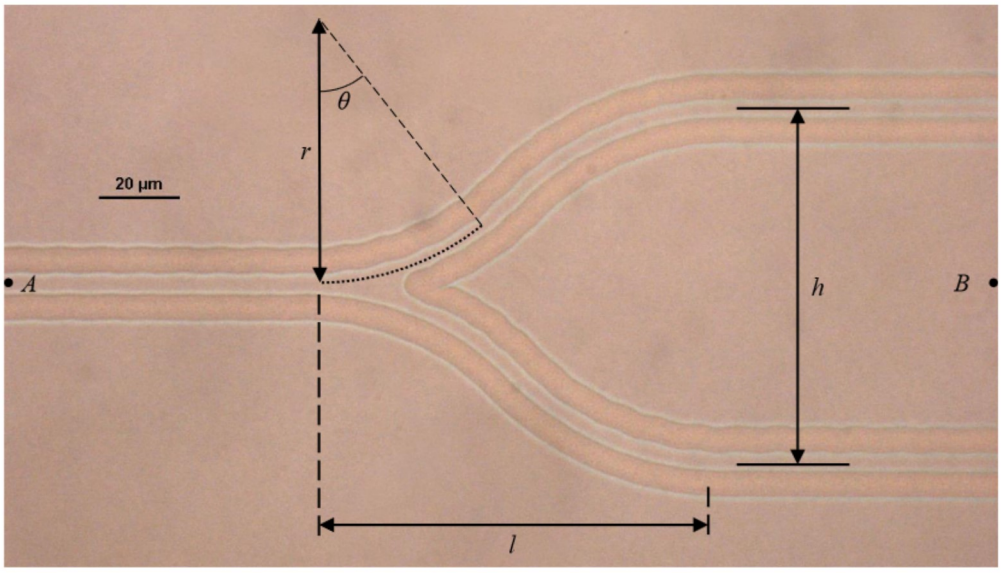


FIGURE 4.17: The Y-junction structure with the user-defined variables of junction arm separation $h$, junction length $l$ and curve radius $r$. From these, the full component geometry can be calculated.

radius of 75 µm in 45° arc sections, and a waveguide width of 4 µm. This width was selected as it demonstrated the lowest transmission loss in cutback measurements. Microscope images of these are shown in Figure 4.18. Similarly to the S-bend structures no guided mode was seen at the output, however scattered light was seen along the output facet distributed across the a-Si:H film. This scattered output demonstrates the lack of confinement that was suspected in the S-bend waveguides, and that was seen to a lesser extent in the end-on IR camera images of the optimisation test waveguides shown in Figure 4.9. Further investigations into these structures would first require the demonstration of lower losses in straight waveguides, and due to time constraints this has been left to future work.

## 4.8 Conclusions

A novel method of waveguide definition in typically low-loss a-Si:H has been presented, using a versatile localised laser-crystallisation process. Proof-of-concept experiments demonstrated transmission losses below 4.5 dB cm$^{-1}$, however comparison between etched and laser-defined waveguides in otherwise identical material showed a significant disparity between the two methods. The lowest observed loss in lithographic waveguides was 4.31 dB cm$^{-1}$ compared to 10.78 dB cm$^{-1}$ in laser-written waveguides. The higher loss in the second set of laser written waveguides is attributed in part to the different heat transfer from the different laser source. Raman spectroscopy showed that a transition region exists at the boundaries of the laser-written stripes, in which the silicon has not been crystallised but the hydrogen content has been reduced by thermally-induced

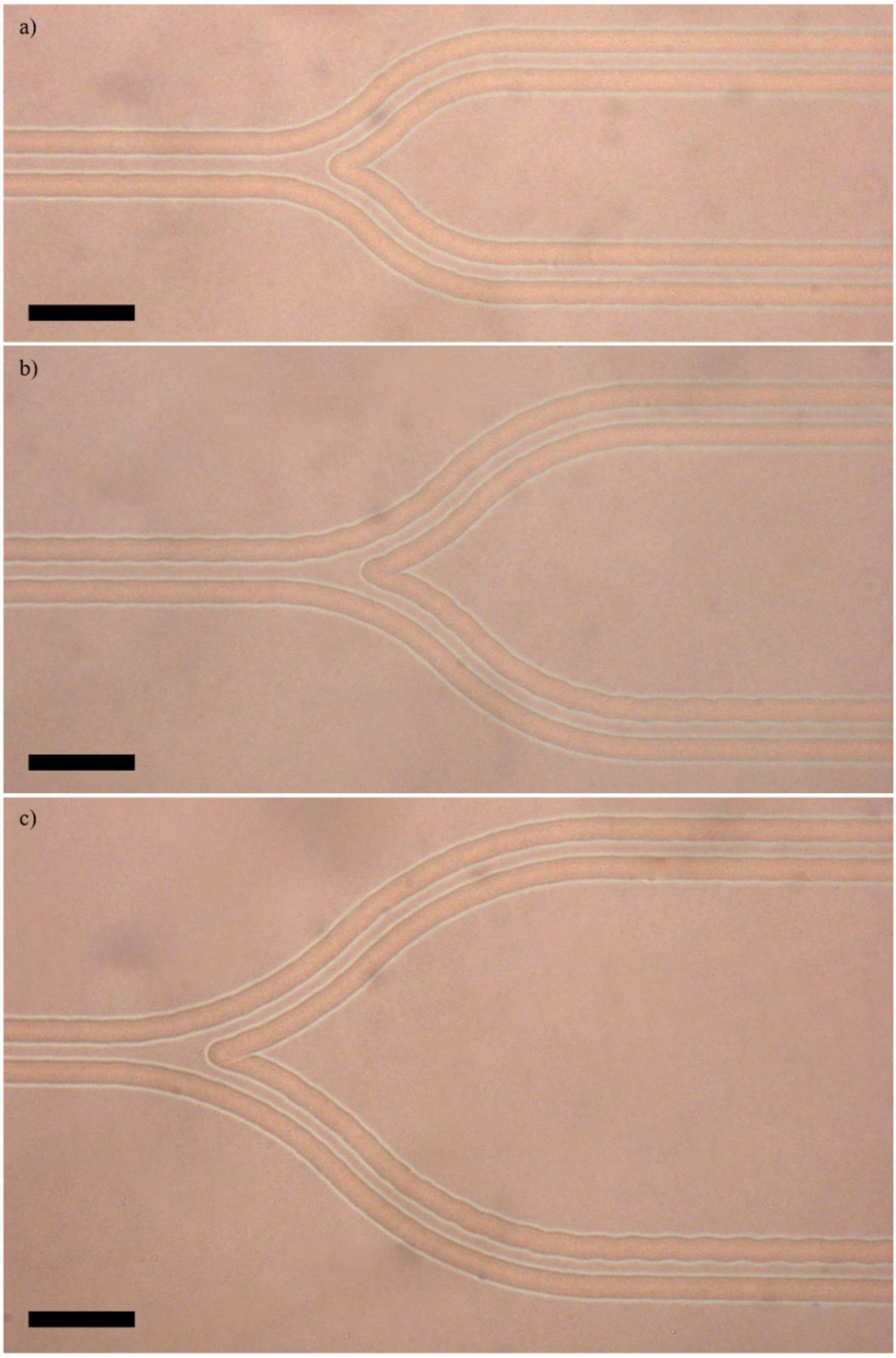


FIGURE 4.18: Y-junction structures with arm separations of a) 50 µm, b) 75 µm and c) 100 µm. Scalebar 20 µm.

outdiffusion. Visible differences in the material under optical microscopy confirmed the presence and width of these regions, implying that a minimum waveguide width

is imposed by this process. The unpassivated defect sites in the amorphous material and the micro-crystalline polysilicon at the core/cladding boundary are suspected to be the primary sources of loss in these structures. Complex structures were fabricated to demonstrate the versatile nature of this process, however high transmission losses prevented the successful demonstration of waveguiding in them.

# Chapter 5

# Polysilicon Wire Waveguides by Laser Annealing of Amorphous Silicon

## 5.1 Introduction

In the work reported in this chapter, continuous-wave laser annealing was used to fabricate polysilicon waveguides from low-temperature deposited amorphous silicon. The existing work in the field of polysilicon photonics is outlined, identifying areas of importance for development. Then, the fabrication processes are described, followed by the methods used for material and optical characterisation. Finally, the results of the experimental work undertaken are presented.

## 5.2 Motivation and Existing Work

The earliest reported use of polycrystalline silicon as a waveguiding material was in 1996, when Foresi et al. demonstrated waveguide losses in excess of $35\,\mathrm{dB\,cm^{-1}}$ [36]. Since then, losses have been reduced to $5.31\,\mathrm{dB\,cm^{-1}}$ by Franz et al. [35], and the substrate temperatures have been reduced to below the 450 °C limit for BEOL integration with the standard CMOS process flow. Additionally, optical components such as ring resonators and electro-optic modulators have been demonstrated. The progression of losses in polysilicon waveguides is shown in Figure 5.1.

The development of polysilicon as an alternative waveguiding material to crystalline silicon was suggested as a means of avoiding the limitations in silicon-based optical interconnections [36]. Specifically, the authors of this early work were trying to address

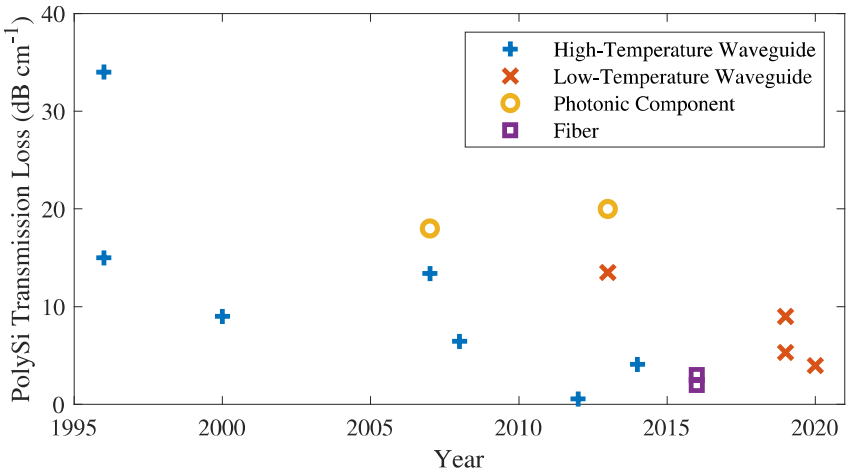


FIGURE 5.1: Advancement in losses in polycrystalline silicon. Initial results were obtained using high-temperature oven annealing to promote crystal growth, reducing transmission losses sufficiently to enable the demonstration of effective optical components. Aside from reported losses of $0.5\,\mathrm{dB\,cm^{-1}}$ in high-temperature $10\,\mu\mathrm{m}$ wide waveguides [42], the reported losses in deposited silicon have now been surpassed by localised laser crystallisation of low-temperature deposited amorphous silicon.

the requirement in SOI systems that the optical interconnects and electronics share a Si layer. This limitation exists as c-Si cannot be deposited, preventing multilayer fabrication and therefore necessitating a mono-layer architecture. The use of polysilicon bypasses these issues, while also avoiding the disadvantages of having to turn to alternative materials. The high refractive index contrast between polysilicon and silica reduces the device footprint as a higher index contrast reduces the waveguide dimensions necessary for confinement, a major drawback to previous considerations of glass or lightly-doped silicon waveguides. Although low-loss a-Si:H can be fabricated at low temperatures, the poor electron mobility prevents use in optoelectronic components which rely on a high mobility to function. Therefore, polysilicon, which exhibits a higher electron mobility, has been investigated with the goal of reducing the transmission loss.

In the first studies by Foresi et al., a-Si films were deposited using low pressure chemical vapour deposition (LPCVD) and crystallised in an oven annealing process at 600 °C. Reduction in surface roughness was seen to have a significant effect on the transmission losses, with a decrease from $77\,\mathrm{dB\,cm^{-1}}$ to $34\,\mathrm{dB\,cm^{-1}}$ following the chemical mechanical polishing (CMP) of the upper waveguide surface. This reduced the root-mean-square (rms) surface roughness from 20.1 nm to 6.8 nm. These results, in combination with the derivation of scattering loss by Payne et al. [104], discussed in Section 2.3, indicates that the minimisation of surface scattering is an important element of waveguide fabrication.

A further study by the same research group demonstrated an additional reduction in polysilicon losses to $15\,\mathrm{dB\,cm^{-1}}$ [28]. This was achieved by the hydrogenation of dangling bonds in the amorphous grain boundaries by electron-cyclotron resonance, after

the 600 °C annealing step. Grain sizes were measured between 0.18 µm and 0.4 µm by transmission electron microscopy, with the largest grains occurring in films deposited at the lowest temperatures. Although no correlation was observed between grain size and optical loss in this range, the significant reduction in loss from the hydrogenation step (34 dB cm$^{-1}$ to 15 dB cm$^{-1}$) is a clear indicator that absorption at dangling bonds is a significant contributor to optical loss in polysilicon. As these dangling bonds are most common in grain boundaries, it can be assumed that the losses in polysilicon waveguides can be improved by increasing grain sizes, thereby reducing the amorphous content and the absorption from dangling bonds.

Losses were further reduced to 9 dB cm$^{-1}$ by Liao et al [37], by carrying out a secondary annealing step at 1100 °C. It was observed that this induced several changes which contributed to the reduction in loss. Average crystal grain size was increased, from 0.2 µm to 0.28 µm, in tandem with the thinning of amorphous grain boundaries. In addition, a decrease in material strain was observed and assumed to have contributed to the lower losses. However, the influence of strain on transmission loss was not determined.

These early studies provide a strong indication of the primary sources of loss to be targeted in ongoing work, specifically the material surface roughness and the amorphous fraction. Surface roughness is a consequence of fabrication techniques, and can be significantly reduced by post-processing stages such as CMP of the upper surface. The presence of amorphous material at the polysilicon grain boundaries induces loss by multiple mechanisms, most importantly absorption of light at dangling bonds and Rayleigh scattering due to the index change. Telecommunications wavelength light with wavelength 1550 nm and energy 0.8 eV is transmitted well by c-Si as the bandgap is 1.1 eV. However, the presence of dangling bonds in amorphous material introduces defect states in the bandgap, increasing absorption as discussed in Section 2.3. Providing a comparison to crystalline silicon, Foresi et al. measured transmission losses in c-Si waveguides with identical dimensions to their polysilicon samples. The c-Si losses were measured as 1 dB cm$^{-1}$, indicating that the crystallinity of polysilicon must be greatly improved to be considered as a viable material for integration in electrical/photonic systems.

Subsequent to this work, transmission losses of 6.45 dB cm$^{-1}$ were reported by Fang et al. in oven annealed polysilicon [39], with surface roughness of 0.4 nm, achieved by CMP of the substrate surface before deposition. By calculating scattering losses from the formulation by Payne & Lacey [104], they determined that scattering from the upper and lower surfaces at an rms roughness of 0.4 nm contributed only 0.05 dB cm$^{-1}$, indicating that the remaining surface scattering loss originated from the waveguide sidewalls. This is reinforced by the observation that lower losses were obtained in wider waveguides, in which the interaction between the mode and the sidewalls is lower. These conclusions present a target of $\sigma < 0.5$ nm for the roughness of all surfaces of polysilicon waveguides, at which point the difference between measured transmission loss and comparable c-Si

reference samples may be assumed to originate solely from scattering and absorption at grain boundaries and in-grain defects.

These observations were confirmed by a study of the relation between waveguide width and transmission loss by Kwong et al. [42]. The deposition of a 250 nm a-Si film by low-pressure CVD, followed by a two-step annealing at 600 °C and 1000 °C, produced polysilicon with grain sizes of $\sim$300 nm. Waveguides with widths between 400 nm and 10 µm were fabricated by lithography, with identical structures also made in a c-Si film for comparison. It was observed in both materials that loss was inversely proportional to width, with the lowest polysilicon losses of 0.56 dB cm$^{-1}$ measured in a 10 µm wide waveguide and losses in the comparable c-Si waveguide were 0.31 dB cm$^{-1}$. In few-micron polysilicon waveguides, losses of $\sim$ 5 dB cm$^{-1}$ were recorded, still lower than in any other reported losses at the time. These low losses in wider waveguides result from the ability of these structures to support higher-order modes. Light scattered at internal grain boundaries will, in narrow waveguides, enter radiative modes, whereas in wide waveguides the scattered light can enter higher-order modes that are still guided.

To fully prove the potential of polysilicon for photonics applications, both passive and active components must be demonstrated, in addition to ongoing research into reduction of transmission losses. Preston et al. manufactured ring and racetrack resonators in oven annealed polysilicon [38], following the process flow of Liao et al. The measured rms roughness was 0.7 nm, a significant improvement over previous reports where CMP of the surface had not been used. Propagation losses in the ring resonators were estimated as 18 dB cm$^{-1}$ which, although higher than previously achieved in polysilicon, have the added impact of bending losses from the 40 µm radius rings. Grain sizes of 0.3 µm were measured by scanning electron microscopy investigation, comparable with previous reports. Following this, active devices were developed on the same platform, with the successful demonstration of both an all-optical [40], and electro-optic modulator [41]. The successful demonstration of functional optical devices marked a major milestone in the development of polysilicon for optics. Although the high-temperature manufacture process utilised to this point is suitable for FEOL integration, this imposes the requirement that all polysilicon deposition takes place before the metallisation and ion implantation stages of the CMOS process flow. The use of laser crystallisation was suggested for back-end compatibility, which would make use of the extensive research into excimer laser annealing, as previously discussed in Section 2.2.2, and allow the substrate temperatures to be reduced below 450 °C.

The first photonic components in CMOS back-end compatible polysilicon, fabricated in films crystallised by ELA, exhibited comparable performance to those manufactured in a high-temperature process flow. For all-optical modulators, loaded quality factors ($Q = \lambda_0/\Delta\lambda$ for a resonance wavelength $\lambda_0$ and bandwidth FWHM $\Delta\lambda$) were measured as 11,200 in back-end incompatible polysilicon [40], and 2,900 for CMOS compatible material [45], still sufficient for high-speed optical modulation. Electro-optic modulation

was also demonstrated in ELA polysilicon, exhibiting a modulation frequency of 3 Gbps [46], compared to 2.5 Gbps in oven-annealed polysilicon [41], and 40 Gbps in c-Si [118]. As stated by Lee et al. [46], "this method frees silicon photonics from its dependence on SOI and allows true monolithic integration with bulk CMOS electronics, DRAM, and even flexible substrates."

Masaud et al. investigated the low-temperature deposition of polysilicon [44], avoiding the additional crystallisation stage used in previous works. This deposition of 220 nm polysilicon films by HWCVD at a substrate temperature of 240 °C produced material with an average grain size of 85 nm, significantly smaller than previous reports from other techniques, and an rms roughness of 8.5 nm on the top surface. Sidewall roughness was measured as 4 nm, and cutback loss measurements demonstrated transmission losses between 16.9 dB $cm^{-1}$ and 13.5 dB $cm^{-1}$, in waveguides ranging in width between 400 nm and 600 nm. Simulations of the loss from surface scattering indicated that the upper and side surfaces contributed 9.2 dB $cm^{-1}$ and 3.1 dB $cm^{-1}$ respectively. Although the manufacturing process utilised was compatible with back-end CMOS integration, the requirement for CMP steps before waveguide manufacture limits the viability compared with other techniques such as laser annealing.

Although excimer laser annealing typically offers grain sizes of $\sim$1 µm, the development of continuous-wave laser annealing in the microelectronics industry has seen reported grain sizes of up to 600 µm [25]. The CWLA process was applied to fiber structures by Healy et al., who applied a focused 488 nm laser directly to an a-Si core and scanned the laser spot along the fiber length. This process utilised the different thermal expansion coefficients of the Si core and the $SiO_2$ cladding to create a strain-induced bandgap modification from 1.11 eV to 0.59 eV, enabling detection of light in silicon at wavelengths up to 2100 nm [33]. XRD crystallography indicated crystal grain sizes of up to 200 µm in the fiber core, and cutback loss measurements showed transmission losses of 5.6 dB $cm^{-1}$. The large grain growth was attributed to the high thermal confinement from the fiber geometry, and it was estimated that alterations to the laser-writing approach would allow significantly larger grain sizes to be achieved.

Losses of 3 dB $cm^{-1}$ were demonstrated in tapered polysilicon core fibers [119]. Tapering involves a similar melting and crystallisation dynamic to localised crystallisation by CWLA, despite the different method for introducing heat to the system. The core is fully melted during the tapering process, allowing it to flow and crystallise inside the cladding. Importantly for low-loss materials, the softening of the fiber cladding acts to reduce the strain induced during solidification, avoiding the previously observed bandgap modification. The crystallinity of the core was investigated by Raman spectroscopy, and seen to be polycrystalline in nature. The crystal boundaries will therefore have contributed to the losses, suggesting that with improvement to the crystallisation dynamics, losses could be further reduced to levels comparable with crystalline silicon.

Combining elements of the tapering and laser annealing processes, Healy et al. used a $CO_2$ laser to crystallise a silicon-core fiber drawn by the 'molten-core' method [34]. The primary loss mechanism in the as-drawn polysilicon-core fibers was identified as the absorption at internal grain boundaries. During crystallisation, the heating laser wavelength was absorbed by the silica cladding, causing a controlled localised heating of the fiber cladding, melting the core through heat transfer. As in tapered fibers, the softening of the cladding minimised the induced strain. The molten zone was then moved along the length of the fiber, resulting in single-crystal growth along the full scanned length, as determined by XRD crystallography. This single-crystal nature was determined to be a result of the core confinement and full melting, which minimised the formation of nucleation sites at the trailing edge and promoted growth of the existing crystal region. The formation of a nucleation site requires undercooling of a liquid volume, and sufficient time for a cluster of atoms to condense and induce crystallisation of the surrounding material. The confinement in the fiber geometry avoided nucleation sites forming from external influences, while the suppression of internal nucleation resulted from the combination of high power and high scanning speed. The high thermal gradient minimised the undercooled volume, and the high speed reduced the available time for formation of the nucleation site. Cutback loss measurements indicated transmission losses of $\sim 2\,\mathrm{dB\,cm^{-1}}$ at 1550 nm, the low loss resulting from the single-crystal nature of the fiber core.

As mentioned in the previous chapter, the application of CWLA to planar amorphous silicon has been studied by Martinez-Jiminez et al., who demonstrated optical transmission at 1550 nm with losses of $9\,\mathrm{dB\,cm^{-1}}$ [49]. Direct laser writing of polysilicon tracks in a planar a-Si film was used to define the waveguide paths, and was followed by selective etching of the amorphous material to isolate the waveguides prior to transmission loss measurements. Scanning electron microscopy and XRD crystallography indicated that the material at the edges of the crystallised paths consisted of nanometer-size crystals due to the lower temperatures being insufficient to melt the silicon, and therefore crystallisation occurred in the solid-phase regime. These crystals acted as nucleation sites for the growth towards the core of the treated region, as discussed in Section 2.2.2.2. These small crystals and the consequent high amorphous fraction resulted in high losses, suggesting that full melting of the treated region, and therefore avoiding seeding from the outer edges, may result in significant improvement to the optical quality.

To improve thermal confinement, Franz et al. carried out etching steps in a-Si deposited at low temperatures by HWCVD, defining waveguide structures before laser crystallisation. This allowed full melting of the waveguide, eliminating the seeding of crystals from the non-melted fringes and encouraging grain growth along the scanning axis. Crystal grains of up to 1.8 mm were observed, far larger than in previous reports. Surface roughness after crystallisation was 0.52 nm and this, along with the large grain size, enabled losses of $5.31\,\mathrm{dB\,cm^{-1}}$ [35]. These represent the lowest transmission losses

to date in CMOS compatible polysilicon, and are the target for loss reduction in the work described in this chapter. Low transmission losses will enable the development of polysilicon waveguides for optical applications. In particular, the observation and characterisation of nonlinear optical effects is desirable due to the broad range of applications of nonlinear photonics.

## 5.3 Waveguide Manufacture

In this section, the manufacture of polysilicon waveguides studied in this project will be described, expanding on the general processes outlined in Section 3.1. In summary, a 400 nm film of amorphous silicon was deposited by HWCVD, then strip waveguide structures were patterned using electron-beam lithography. These a-Si strips were crystallised under a focused CW laser beam. Throughout this process, the goal was to keep the bulk of the substrate at a temperature below 450 °C to ensure compatibility with the back-end-of-line CMOS process flow.

### 5.3.1 Deposition of Amorphous Silicon

The substrate material for the polysilicon waveguides was a commercial crystalline silicon wafer with an oxide layer for optical isolation. This platform was chosen for its similarity with the CMOS systems with which these waveguides are intended to be compatible. A 5 µm oxide layer was grown by thermal oxidation, a process chosen for its capacity to produce high-quality silica. Although the growth temperatures are high, low-temperature CVD silica layers would be suitable choices for practical integrated systems.

After the growth of the oxide layer, the chip was cleaned with acetone, isopropyl alcohol and deionised water, then all residues were removed with a plasma asher. Hot-wire CVD was carried out using an Escherkon Nitor 301, as shown in Section 3.1.1.1. The HWCVD process was chosen due to its capacity for producing low-hydrogen films at low temperatures. Other processes, such as plasma-enhanced CVD and low-pressure CVD, typically produce films with a high hydrogen content during deposition at low temperatures, however the presence of hydrogen has been shown to introduce the risk of sample damage during the following crystallisation stage [79]. The substrate was heated to encourage uniform material adhesion, and the temperature was set to 230 °C to ensure the CMOS thermal budget was not exceeded. A five minute warming period was allowed to ensure the substrate reached the set temperature before deposition began, ensuring a constant deposition rate throughout the process. To remove potential contaminants, the deposition chamber was evacuated to a pressure of $10^{-6}$ mbar.

The tungsten filament was heated to a temperature of 1730 °C with a current of 41 A and a voltage of 26 V. The silane precursor was passed over the filament at a flow rate of 40 standard cubic centimetres per minute (sccm), causing thermal decomposition to $H_2$ and Si. The molecular hydrogen was removed from the deposition chamber by the vacuuming systems while the Si adhered to the sample surface. The deposition rate was monitored by checking the film thickness after a short initial deposition period, and the remaining deposition time was adjusted accordingly to give a material thickness of 400 nm, which was checked after deposition with an ellipsometer.

### 5.3.2 Electron-Beam Lithography

The electron-beam exposure was carried out following a positive pattern which isolates the waveguides with a 5 µm wide channel. This ensures thermal confinement for full melting of the strips during laser processing. The lengths of the waveguides were 20 mm, to give sufficient length for cutback loss measurements followed by nonlinear characterisation. Waveguide widths of 1, 1.5, 2, 3 & 4 µm were investigated. Figure 5.2 compares a section of the digital lithography mask and a microscope image of an etched waveguide. The cross-hatched areas of the mask show the region to be exposed to the electron beam during the patterning step, and match the dark regions of the microscope image of the etched waveguide which are the channels etched down to the silica BOX layer.

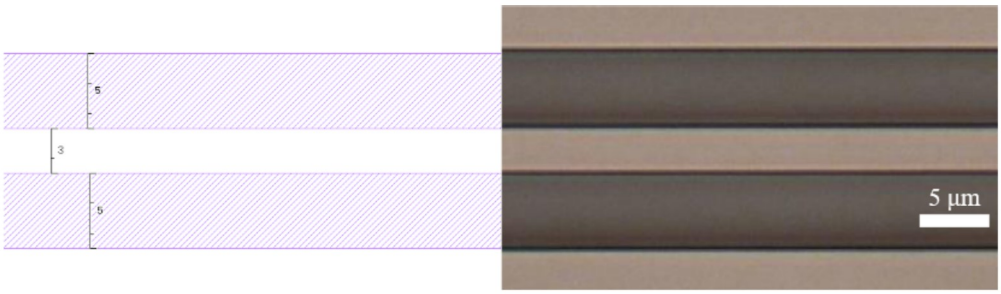


FIGURE 5.2: Comparison between digital electron-beam lithography mask (left) and etched sample (right). The hatched areas are exposed to the electron beam and subsequently etched to the oxide layer. A 3 µm wide wire is isolated by 5 µm wide trenches.

The resist development removes the exposed areas, in which the resist is chemically altered by the incident electron beam to become soluble. Once the resist is developed, an ICP-RIE process removes the exposed silicon as described in Section 3.1.2. The process uses two gases, each with a specific purpose. Sulphur hexafluoride ($SF_6$, flow 25 sccm) reacts with silicon, removing the exposed material, while octofluorocyclobutane ($C_4F_8$, flow 59 sccm) acts as a passivation for the etched sidewalls, preventing lateral etching of the film and therefore providing higher etching accuracy. These chemicals and flow rates gave an etching rate of around 190 nm $s^{-1}$.

### 5.3.3 Laser Crystallisation

Following definition by e-beam lithography, the a-Si wires were crystallised by direct CW laser melting, as shown in Section 3.1.3. By scanning the focused laser spot along the waveguide, the amorphous material was melted and recrystallised as polysilicon. The incident power was set close to the ablation threshold, as this has been shown to increase the crystal size [100]. The lithographic definition of the waveguides, as discussed in Section 5.3.2, was carried out to improve thermal confinement and ensure complete melting of the waveguide volume. The trenches between the waveguide and the planar a-Si acted as horizontal thermal isolation, and the low thermal conductivity of air and silica relative to silicon (see Table 5.1) reduced the vertical heat transfer away from the waveguide.

| **Material** | **Thermal Conductivity** ($\mathrm{W\,m^{-1}\,K^{-1}}$) | **Thermal Expansion Coefficient** ($\mathrm{K^{-1}}$) |
|---|---|---|
| Air | 0.026 [120] | - |
| $SiO_2$ | 1.3-1.5 [121] | $0.55 \times 10^{-6}$ [122] |
| Si | 148 [120] | $2.6 \times 10^{-6}$ [123] |

TABLE 5.1: Thermal conductivity and thermal expansion coefficient of silicon, silica and air.

It has been shown in simulations of comparable lower temperature systems that silica acts as an effective insulator in a fiber geometry [33]. In a quasi-steady state with a maximum temperature of 1600 K, temperatures dropped to below the CMOS thermal budget at a distance of under 1 µm from the core/cladding interface. The systems studied in this project were at a significantly higher temperature, estimated to be nearly 3540 K, the boiling point of silicon. This is due to the laser crystallisation being carried out close to the ablation threshold. However the BOX layer thickness was 5 µm, and therefore the thermal transfer to the substrate is unlikely to be a barrier to CMOS integration. A further investigation of this would be of value, but has not been carried out due to time constraints.

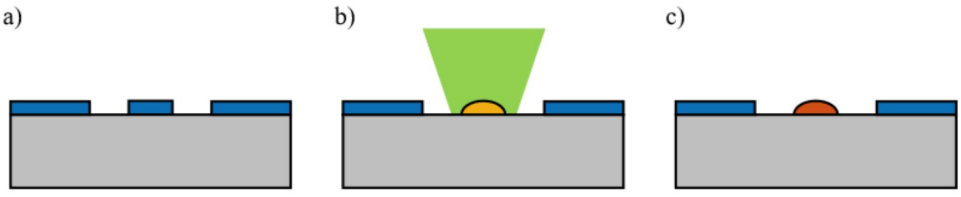


FIGURE 5.3: Cross-section schematic of wire structures during laser crystallisation. a) Amorphous silicon with etched channels providing thermal isolation. b) During laser crystallisation, the wire is locally melted and reshapes due to surface tension. c) The semi-elliptical cross-section is maintained after crystallisation.

The differing thermal expansion coefficients of silicon and silica, as listed above, must also be considered when carrying out laser crystallisation. As observed in fiber systems by Healy et al. [34], the presence of silica material adjacent to laser-crystallised silicon can induce thermal stress, altering the optical properties. This may, in future work, be applicable to bandgap tailoring in these waveguide structures, but at the present time this has not been investigated. However, strain was observed in Raman spectroscopy measurements, resulting from the greater expansion of the waveguide relative to the oxide layer. This is discussed further in Section 5.4.2.

The fully molten volume reshapes due to surface tension, as shown in Figure 5.3. The waveguide reshaping carries the benefit of reducing the surface roughness, as the upper surface maintains the surface tension-induced smoothness during solidification. Atomic force microscopy (AFM) measurements before and after crystallisation have shown an improvement in the rms roughness (Figure 2.7) from 3.4 nm to 0.5 nm, reducing the estimated scattering loss from 15 dB cm$^{-1}$ to 0.4 dB cm$^{-1}$. Figure 5.4a shows the AFM measurement of an arbitrarily selected area of as-deposited amorphous silicon, and Figure 5.4b shows an AFM measurement of a section of a polysilicon waveguide. The occasional high points on the polysilicon surface are believed to be residue from the polishing procedure used on the sample studied. Figure 5.4c and d show scanning electron microscopy (SEM) images from an as-etched and annealed waveguide respectively. Here, the reshaping effect of the melting during crystallisation is clearly seen from the altered structure before and after laser writing. The surface contaminants in the post-crystallisation SEM image are polishing residue, supporting the assumption that this is true of the AFM image. This also suggests that the true rms roughness would be lower than the calculated 0.5 nm.

In some instances, it was observed that the etching process did not fully remove the amorphous material in the isolating channels. When this occured, several unwanted effects were observed during the crystallisation process. Most significantly, the shape of the crystallised region was significantly different from the desired structure shown in Figure 5.4. The non-etched material acted as a channel along which heat flowed out of the central waveguide region, negating the benefits of the etching stage. Furthermore, different results were seen from the reshaping of the molten material. As a thin layer of Si remains in the etched channels, which is not fully melted due to the lower power at the edges of the incident beam, the silicon flattens out and spreads, instead of taking the approximately semi-circular shape described above. This is displayed in Figure 5.5, showing a crystallised area that had not been fully etched during the lithography process. The outer edges of the a-Si are crystallised by SPC, likely resulting in poor crystal size as discussed in Section 2.2, and the reduction in film thickness made light injection unfeasible.

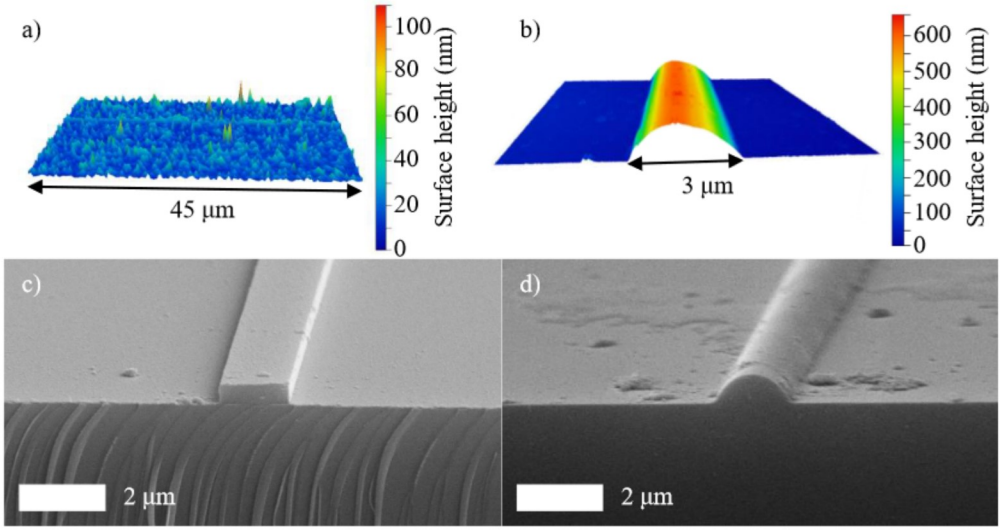


FIGURE 5.4: Atomic force microscopy image of a) as-deposited amorphous silicon and b) a crystallised waveguide. A smooth waveguide surface is seen with a measured root-mean-square roughness of 0.5 nm. Scanning electron microscopy c) before and d) after laser crystallisation shows the change in cross-section. Surface contamination in d) is the residue of wax adhesive used in the polishing process.

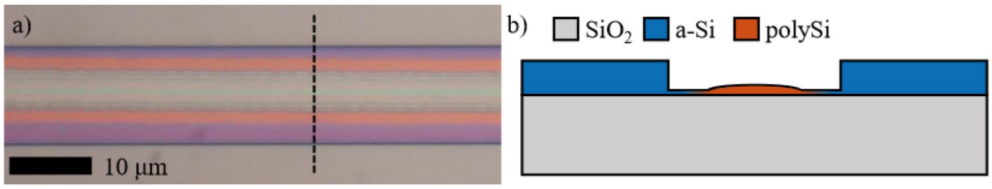


FIGURE 5.5: a) Microscope image and b) diagram cross-section along the dashed line of a laser-crystallised waveguide with insufficient channel etching. The a-Si strip flattens when melted, as it is not 'contained' by surface tension.

## 5.4 Material Characterisation

Investigations of the material quality of the polysilicon waveguides were carried out to provide additional quantitative data feedback on the crystallisation parameters used. Visual inspection of the waveguide surfaces with an optical microscope was used to identify the presence of major defects and scattering points, and is a quick method to assess the surface roughness and the consistency of the waveguide shape. It was also used for a rapid initial assessment of the viability of each waveguide for transmission measurements. Raman spectroscopy data provided information on the amorphous and crystalline fraction in the examined volume, and XRD crystallography was used to directly measure crystal grain sizes. All of these factors contribute to the losses of a waveguide due to surface scattering, and the absorption and scattering of light at amorphous grain boundaries.

### 5.4.1 Visual Inspection

Microscope imaging of the waveguide upper surface provides quick identification of defects in the waveguide structure and qualitative feedback on the anticipated transmission quality. Imperfections in the structure induce losses due to either scattering or absorption, or in some cases, such as ablation, will prevent transmission entirely. The ideal structure, shown in Figure 5.6, is a smooth waveguide with no deviation in the surface along the whole observed length. The lighter central region fading to the darker edges is characteristic of the curved shape when seen under top-down illumination, as a greater proportion of the incident light is reflected by the upper surface. The darker channels to either side of the waveguide are the $SiO_2$ BOX layer which is exposed by e-beam lithography.

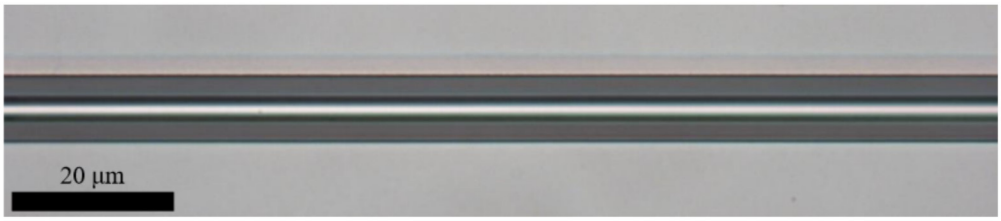


FIGURE 5.6: Microscope image of a well-crystallised polysilicon waveguide, with a smooth and consistent surface along the full length. Losses in this waveguide were measured as $4\,\mathrm{dB\,cm^{-1}}$.

Visible defects in the waveguide structure were common due to the sensitive nature of the laser crystallisation process. The most frequently observed defects are detailed here, with remarks on the source of each and its impact on waveguide transmission. Example microscope images of these are shown in Figure 5.7. Although the most severe defects are seen easily, some such as minor structural imperfections or embedded defects are best observed under differential contrast interference microscopy (DCIM), as shown in Figure 5.7b and c.

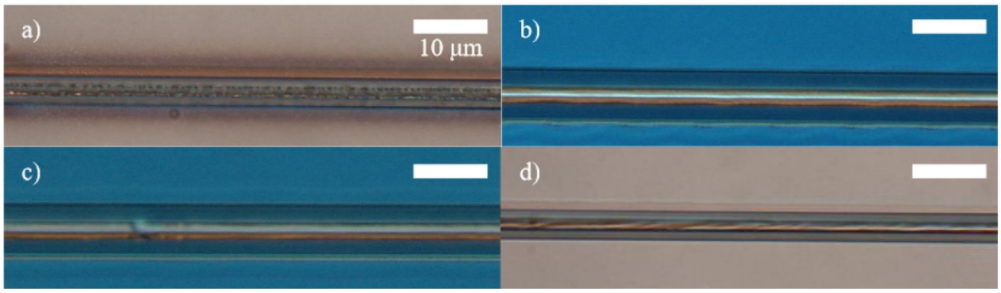


FIGURE 5.7: Defects observed in polysilicon waveguides following laser processing. a) Ablation, b) 'wavy' structure, c) embedded defect, d) uneven surface structure.

In the most extreme examples, the waveguide material may be completely removed during laser processing, as shown in Figure 5.7a. These ablation cases resulted either from a significant excess of power, or the ignition of surface contaminants. In either case,

the damage resulted in total loss of coupled light, rendering a waveguide unusable. Particulates scattered around the waveguide were observed after ablation, indicating that the removed material was then redeposited in the vicinity. For closely-spaced waveguides, these may result in scattering losses in adjacent waveguides. Large (300 µm) spacings have avoided this, however in on-chip applications the gaps would be smaller to maximise use of the chip real estate. To avoid this damage occurring, the laser power was tested before each laser crystallisation step and carefully monitored throughout. Care was also taken to remove surface contaminants: three-step ultrasonic bath cleaning with acetone, isopropyl alcohol and deionised water removed organic and inorganic particulates, a pressurised dry air line allowed zero-contact removal of dust immediately before crystallisation, and the laser writing system was within a closed perspex container throughout the processing. In some cases this did not remove all contaminants, and so for maximum protection, the entire process would ideally be carried out in a cleanroom environment, avoiding all contact with a high-particulate atmosphere, or in an inert chamber to entirely eliminate environmental effects.

A commonly observed defect was a regular oscillation in the waveguide following laser crystallisation (Figure 5.7b). Unlike the ablation of material, this did not prevent transmission measurements being undertaken, however the impact on the losses has not been characterised due to time constraints. This irregular structure is expected to have a detrimental effect on transmission due to enhanced scattering. The oscillations were observed to be periodic in time, with spatial frequency dependent on the stage movement speeds. These oscillations have since been eliminated using vibration isolation systems on the optical table on which the crystallisation setup is mounted.

On occasion, waveguide defects were observed where some embedded material was deforming the waveguide or would be blocking the path of light through it, as shown in Figure 5.7c. This is assumed to be instances where surface contaminants have not ignited and induced ablation, but have instead been incorporated within the liquid silicon during melting. However, these defects can be avoided by a systematic check of the waveguide surface using the positioning and monitoring camera immediately before starting the crystallisation process. Residual surface contaminants could be identified using this, and appropriate measures to avoid damage, such as further cleaning, could be taken.

In some waveguides, an inconsistent cross-section and a corresponding uneven surface structure was observed (Figure 5.7d). Distinct from the previously mentioned sidewall oscillations, these faults generally resulted in losses too high to take transmission measurements. Resulting from incomplete melting during laser processing, these areas do not have the surface tension induced shape shown in Figure 5.3. This is caused by insufficient heat transfer to the waveguide, due to either insufficient laser power or improper focusing resulting in a larger beam spot, and therefore lower intensity. These defects

were observed following system realignments or alterations, when the correct focus position had not been accurately determined, but were fixed by redetermining the z-axis position for laser focus and the total power at laser focus.

### 5.4.2 Raman Spectroscopy

The optical quality of polycrystalline silicon is dependent on the crystalline fraction, as a lower amorphous content reduces absorption. Raman spectroscopy can be used to make an assessment of the crystalline fraction by comparison with a pure crystalline silicon reference sample, as a rapid, non-contact, non-destructive characterisation process. The characteristics of interest in this process are the peak position and the FWHM of the polycrystalline Raman response. This peak has contributions from both the amorphous and crystalline spectra, which are shown in Figure 5.8. The amorphous peak is broad and centred at approximately $480\,\mathrm{cm}^{-1}$, while the crystalline peak has a FWHM of $2.7\,\mathrm{cm}^{-1}$ and is centred at $520\,\mathrm{cm}^{-1}$. The peak position indicates the material strain, which results from the difference in thermal expansion coefficients between the silicon and the silica BOX layer as discussed in Section 5.3.3. The strain in the waveguide changes the material bond lengths, which in turn influences the Raman shift. A study to comprehensively determine the influence of material strain on transmission loss would be of value, as it would help to guide further development of this technique. The FWHM indicates the crystalline fraction, as the unstructured nature of amorphous material results in a greater variety of bond lengths.

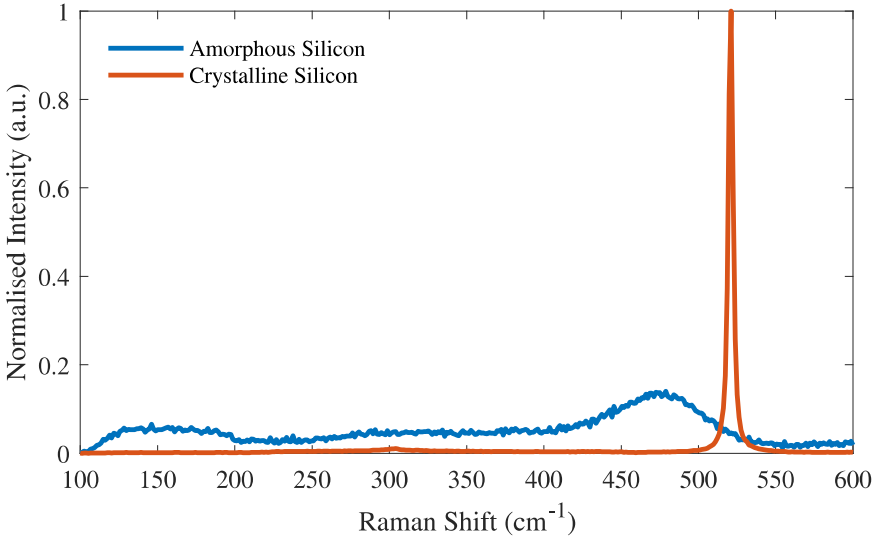


FIGURE 5.8: Comparison of Raman spectra of amorphous and crystalline silicon, both normalised to the crystalline peak intensity.

As an example, comparison between the crystalline spectrum and the spectra of high and low crystallinity polysilicon is shown in Figure 5.9. The data and fits show the

Voigt peaks, before the separation of Lorentzian and Gaussian influences. High-quality polysilicon exhibits a Voigt peak of similar width to c-Si, shifted to lower wavenumbers by strain. Low-quality polysilicon has a broader peak, resulting from the greater variation in bond length from increased amorphous content.

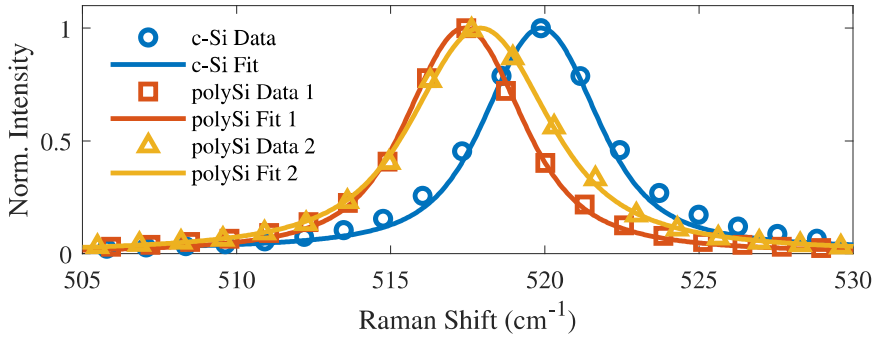


FIGURE 5.9: Raman peaks for unstrained crystalline silicon (c-Si Data) and strained polysilicon with high (Data 1) and low (Data 2) crystallinity. The strain and amorphous content broaden the polysilicon peaks and shift the peak position to a lower wavenumber. A greater amorphous fraction results in a broader peak.

### 5.4.3 X-Ray Diffraction Crystallography

To investigate crystal grain sizes, X-ray diffraction crystallography was carried out at the Diamond Light Source facility. X-ray diffraction crystallography allows direct detection of individual crystal grains, providing useful information regarding their size and orientation. As the optical loss is adversely affected by the presence of amorphous boundaries between grains, it is useful to determine the relation between crystallisation conditions and grain size.

As described in Section 3.2.2, an X-ray beam with a focused spot diameter of 2 µm was directed onto the waveguides with a grazing incidence, maximising the intersection between the beam and the waveguide. The beam energy was set to 16.8 keV and the diffracted beam was captured by a detector screen positioned to intersect with one quadrant of the Debye cone. Calibration patterns, as shown in Figure 5.10, were captured experimentally from a silicon crystal powder and were used to accurately determine the sample-detector separation. The spacing of each crystallographic plane is known, as is the wavelength of the incident beam. From these, the diffraction angle from each plane is known from Equation 3.3. By fitting the diffraction rings using the DAWN (Data Analysis WorkbeNch) program [124], the distance from the X-ray beam impact site to the detector screen can be calculated.

After calibration, XRD spectra were captured for a series of points along each waveguide separated by 50 µm. The spot size perpendicular to the waveguide was ∼3 µm, sufficient to cover the entire waveguide width. The grazing incidence extended the spot along the

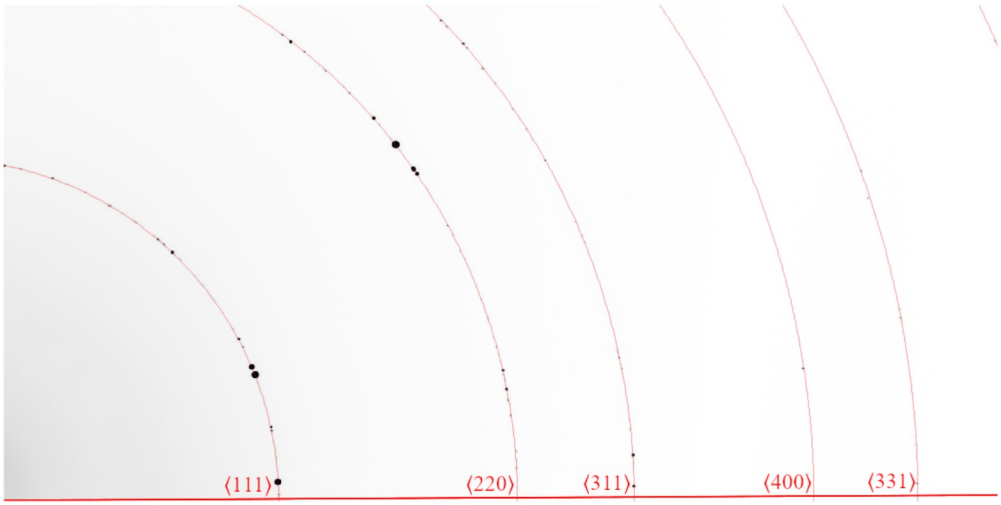


FIGURE 5.10: Theoretically calculated x-ray diffraction rings (red), showing the expected scattering angles of crystallographic planes, overlaid onto the experimental polycrystalline calibration pattern. Dark spots show high signal intensity.

waveguide to nearly 50 µm in length, maximising the number of crystals that would be detected. The number of distinct crystal signals within each scanned area was recorded to measure the local crystalline quality. Additionally, by tracking the presence of diffraction signals in consecutive points along each waveguide, the length of each crystal was measured with a resolution equal to the step length between measurements, in this case 50 µm. Figure 5.11 shows examples of the diffraction patterns from a monocrystalline (a) and polycrystalline (b) region respectively. In these images, darker areas represent greater signal strength. The solitary signal from a ⟨3 1 1⟩ plane in the monocrystalline image shows as a high intensity signal as it is the only crystal in the investigated region. In the polycrystalline image, there are eight spots with lower intensities, as the diffracted beam is split across many directions. The apparent vertical division in each image (the straight lighter line approximately central to the image) is believed to be a "shadow" of the sample.

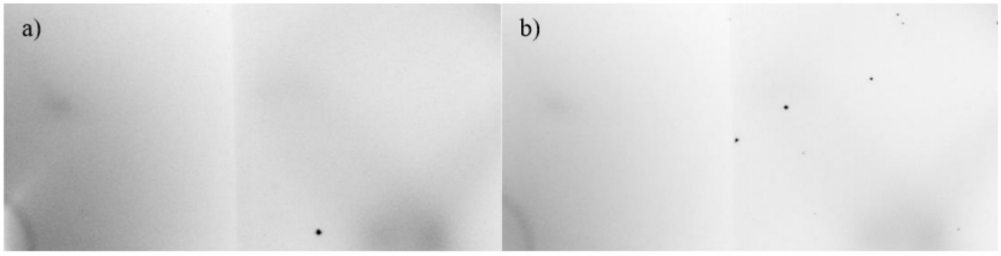


FIGURE 5.11: Diffraction patterns from a) a monocrystalline region with crystal orientation ⟨3 1 1⟩ and b) a polycrystalline region with crystals visible from the ⟨2 2 0⟩, ⟨3 1 1⟩, ⟨4 0 0⟩, ⟨3 3 1⟩ and ⟨4 4 2⟩ orientations.

## 5.5 Optical Characterisation

The defining characteristic of waveguide quality is the optical performance, which is determined by measuring the linear transmission at the wavelength of interest. Optical loss measurements by the cutback method were used to determine the transmission and coupling losses of waveguides manufactured by the methods described above, using a CW laser source emitting at the conventional telecommunications wavelength 1550 nm.

### 5.5.1 Transmission Loss Measurements

To obtain linear loss measurements, the procedure described in Section 3.2.3 was followed. As this has already been detailed, a summary is presented here. A CW diode laser emitting at 1550 nm was collimated and focused into a waveguide input facet using a 60× focusing objective. The facets were checked by optical microscopy after cleaving, and the facet with the smoothest surfaces and fewest defects was chosen for input coupling. The waveguide output light was collected and re-collimated using a 40× objective lens and passed through an aperture to isolate the waveguide output. This was directed onto an infrared-sensitive camera to allow initial optimisation of coupling, then a power detector was used to give more accurate feedback for fine-tuning. The input and output powers were recorded, and the loss calculated using Equation 2.3. This process was repeated at multiple waveguide lengths, and a linear best-fit line was fitted to the resulting graph of length against loss.

## 5.6 Laser Crystallisation Work

During this project, two different CW laser sources were used for the crystallisation stage of waveguide fabrication. The first was a Coherent Innova $Ar^+$ gas laser emitting at 488 nm, however following a critical failure this was replaced by an IPG Photonics GLR 10W fiber laser emitting at 532 nm. Different sets of results were achieved with each, and these have been separated in the following sections.

Using the $Ar^+$ gas laser, initial fabrication work was carried out with the main focus being on optimising the material quality, as studied by Raman spectroscopy and XRD crystallography. Although optical transmission measurements were attempted, damage during the polishing stage of the cutback process prevented the collection of sufficient data from any samples.

While awaiting a replacement of the failed $Ar^+$ laser, the use of other laser sources was investigated including a frequency-doubled 244 nm $Ar^+$ gas laser and a 445 nm Roithner Lasertechnik diode laser. However, the former was installed in a laser writing system designed for other applications and with limited availability, while the latter

did not provide enough power to the sample surface to melt the a-Si wires. Therefore, neither were used further for this work after initial tests. Additionally, investigations into alternative methods for facet preparation during cutback were carried out, and it was determined that cleaving was more suitable. The polishing and cleaving processes, with the associated advantages and drawbacks of each, have been discussed in Section 3.2.3.2.

Following the installation of the 532 nm fiber laser, crystallisation work resumed. Cutback loss measurements were achieved, and nonlinear propagation was observed and characterised. Further Raman spectroscopy measurements were taken to establish a connection between material and optical characterisation results, although no XRD measurements were taken as access to the Diamond Light Source facility was no longer available.

The fabrication conditions and characterisation results from waveguides produced using the two different lasers are detailed in the remainder of this chapter.

### 5.6.1 Argon-Ion Laser

For early crystallisation work, electron-beam lithography was used to define waveguides structures with widths of 1, 1.5 & 2 µm in 400 nm thick HWCVD a-Si films. Crystallisation was carried out using the apparatus described in Section 3.1.3, with a 488 nm wavelength incident beam focused though a 10×, 0.25 NA objective. The stage scanning speed was 0.1 mm s$^{-1}$ for all waveguides. Short testing sections were written at a range of powers and these were examined with a microscope to initially determine the material quality.

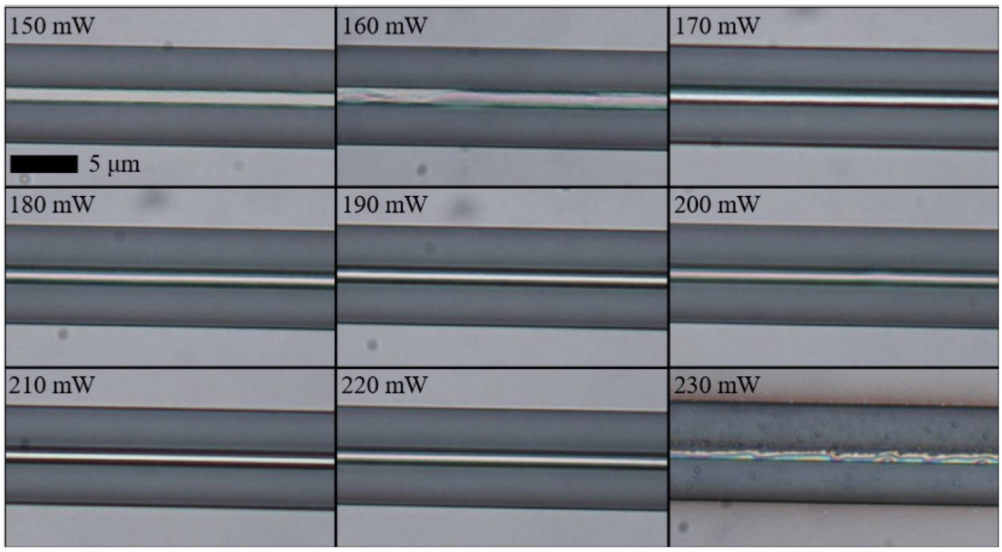


FIGURE 5.12: Microscope images of laser-crystallised 1 µm waveguides at powers from 150 mW to 230 mW.

An example of the optical microscopy observations is shown in Figure 5.12. This shows images of test sections of 1 µm waveguides crystallised with incident powers between 150 mW and 230 mW in 10 mW increments. At 150 mW, no significant change to the waveguide structure is seen, indicating that the transferred power was insufficient to induce melting. At 160 mW, reshaping is irregular and inconsistent, and therefore higher powers are expected to fully melt the silicon strip. Between 170 mW and 220 mW the waveguide shape is smooth and uniform, and so this power range was selected for further investigation. Tests at 165 mW and 225 mW were also carried out to more accurately determine the upper and lower thresholds for crystallisation. Finally, laser processing at 230 mW is seen to ablate the amorphous material, and scattered particles are visible as a grainy texture in and around the etched channel. For both 1.5 µm and 2 µm waveguides, complete melting began at 190 mW and ablation did not begin under maximum incident power (240 mW) unless triggered by some form of surface contamination.

Following these tests, full-length waveguides were written with powers across the range in which full melting was observed, and the material quality was measured using Raman spectroscopy following the method described in Section 5.4.2. From studies of the dynamics of continuous-wave laser annealing by Michaud et al. [100], it is expected that the Lorentzian peak FWHM will approach that of crystalline silicon as the power is increased. They observed that for a constant laser scanning speed, crystal grain size correlates with the incident laser power. Grain size is, in turn, connected to the amorphous content of polysilicon, and an increased amorphous fraction will broaden the Raman response due to a greater variation in bond length. Figure 5.13 shows the lowest measured FWHM for the different waveguide widths and annealing powers, showing that good crystallinity can be obtained using this process across a wide range of conditions. The lowest FWHM are seen in the 1 µm and 1.5 µm waveguides, and it is thought that this results from the higher thermal confinement from the smaller dimensions. However, it seems likely that similar results would be obtained from 2 µm structures under the correct conditions.

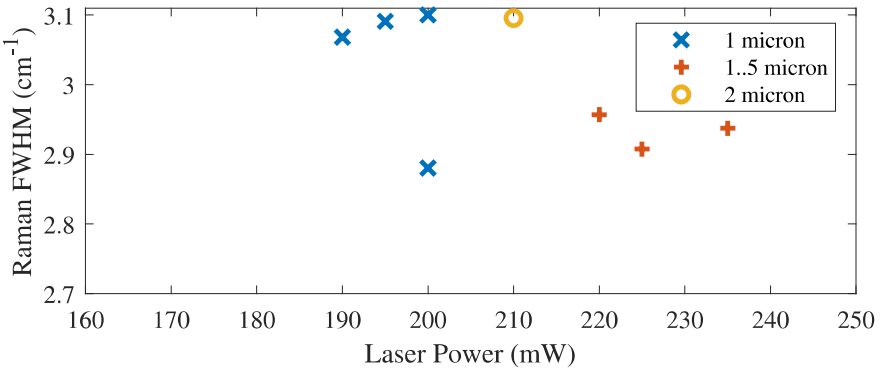


FIGURE 5.13: Lowest Raman FWHM in 1 µm, 1.5 µm and 2 µm waveguides, compared to annealing power.

Higher FWHM, not shown here, were obtained across the entire range of tested powers, suggesting that the results from Raman spectroscopy may be highly dependent on the exact positioning of the excitation laser during measurements. The excitation laser was focused to a spot diameter of $\sim 1\,\mu m$, and so will not fully encompass grains larger than this. On a single waveguide, Raman spectra taken at the middle and ends of a crystal grain, as shown in Figure 5.14, will exhibit different responses due to the different amorphous fraction. This image was taken using scanning electron microscopy, following the selective etching of amorphous silicon by a standard Secco etch process. The etching solution consists of potassium dichromate ($K_2Cr_6O_7$), which oxidises amorphous silicon, and hydrofluoric acid (HF) which etches silica. Scanning electron microscopy then requires a gold coating to avoid charge accumulation, and so this is a fully destructive process and was therefore only carried out on a few selected samples in this project.

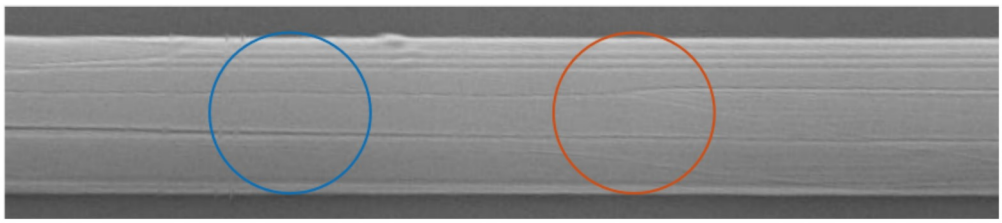

FIGURE 5.14: Selective etching of amorphous silicon reveals the grain boundaries, seen here under scanning electron microscopy. Circled regions are mid-grain (blue) and end-grain (orange) points, which will return Raman spectra with different widths.

Some waveguides were selected for investigation by XRD at Diamond Light Source. The waveguides investigated were early samples for which loss measurements were not successfully obtained due to sample damage during the cutback loss measurement process. Two notable results from these investigations were the observation of a locally monocrystalline section of a waveguide as shown in Figure 5.15, and the presence of a single crystal grain extending over 1.6 mm shown in Appendix B. These maps mark the presence of distinct crystal grains at points separated by 50 µm. The monocrystalline region in Figure 5.15 is a section of a larger crystal that spans a total length of 650 µm (Crystal 5), with no concurrent signals observed in a 200 µm region towards one end.

Both the monocrystalline section and the long crystal were observed in a waveguide of width 2 µm, crystallised at $0.1\,mm\,s^{-1}$ with an incident power of 90 mW through a 20× magnification focusing objective, which produced a spot diameter of 2.5 µm. The lower power requirement for high-quality crystallisation is due to the smaller spot diameter from the higher magnification objective and the resulting higher intensity. The large grain size is consistent with previous large-grain observations from CWLA processes within our research group, in which crystals with approximate lengths of 1.6 mm and 1.8 mm were recorded [79], and is more than 6 orders of magnitude larger than reported grain sizes from excimer laser annealing.

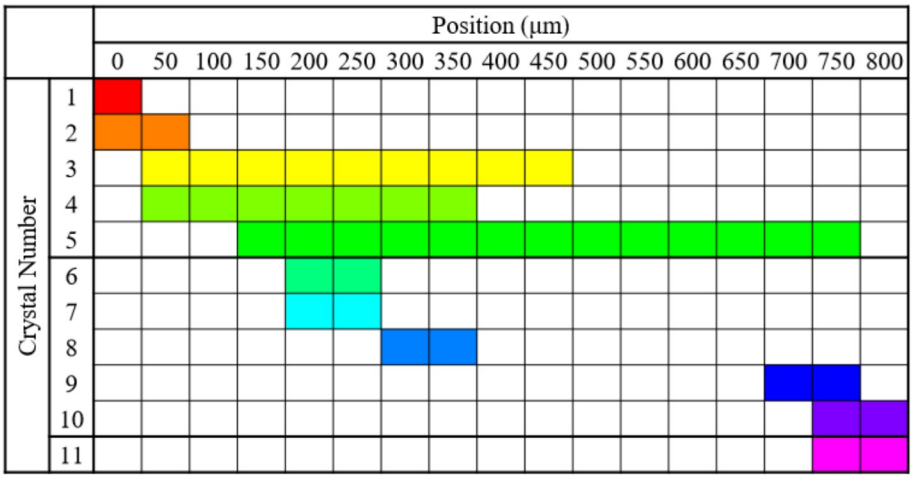


FIGURE 5.15: Map of crystals detected adjacent to a 650 µm long crystal, with a 200 µm long monocrystalline region from 500 µm to 650 µm.

The growth of single grains on this scale, and the demonstration of monocrystalline regions in polySi waveguides manufactured by CWLA, clearly demonstrates the potential viability of this method for the creation of optical-quality polysilicon.

### 5.6.2 Fiber Laser

Following the replacement of the laser source with the high-stability 532 nm fiber laser, samples were fabricated with increased waveguide widths of 2, 3 and 4 µm. This was done to improve waveguide durability, as cleaving had been observed to damage smaller waveguides more frequently. The deposition and etching process and parameters remained unchanged, but the laser crystallisation conditions were affected by the change in wavelength from 488 nm to 532 nm, as this affects the absorption. Following material and optical characterisation of waveguides crystallised with a range of conditions, the parameters which produced lowest loss were identified as 0.1 mm $s^{-1}$ scanning speed and incident power 285 mW with a waveguide width of 3 µm. A sample was fabricated with all waveguides 3 µm wide and processed with these conditions.

In a similar manner to the work in Section 5.6.1, optical microscopy was used to determine the power thresholds for reflow and ablation by examining the results of the crystallisation of short test sections. Incident laser power $P_{Sample}$ was controlled in two ways - a coarse setting of the laser output power $P_{Las}$ in 100 mW increments, and adjusting the angle of the half-wave plate $\theta_{\lambda/2}$ in the beam path in 5° steps. The relation between $P_{Las}$ and $P_{Sample}$ is shown in Table 5.2.

| $\theta_{\lambda/2}$ | $P_{Sample}$ $P_{Las} = 600\,\mathrm{mW}$ | $P_{Las} = 700\,\mathrm{mW}$ |
|---|---|---|
| 20° | 121 mW | 141 mW |
| 25° | 182 mW | 213 mW |
| 30° | 240 mW | 280 mW |
| 35° | 285 mW | 330 mW |
| 40° | 336 mW | 392 mW |
| 45° | 358 mW | 417 mW |

TABLE 5.2: Variation in incident power at sample surface with laser output power and half-wave plate angle. Lost power at maximum transmission (45°) results from other components in the optical system.

In this section, reference will be made to sample sets, individual chips, groups of waveguides and individual waveguides. To ensure consistency, these will be referred to according to the labels assigned during experimental work, and so the labelling system is explained here and shown in Figure 5.16. A label consists of up to four elements separated by a period, for example "21.1.E.5". The first element, here '21', designates the sample number, and corresponds to a set of samples (typically 2 cm × 4 cm wafer chips) on which the deposition of the optical silicon layer was carried out simultaneously. The second element, here '1', indicates which of the chips in that sample set is being referred to, as the deposition was usually done on between 2 and 4 chips at once. The lithography masks used defined sixty waveguides on each chip, in six groups of ten, and so the third element of the label designates which group is being referred to - in this instance the label 'E' designates the fifth of six groups. Finally, the fourth element, in this example '5', corresponds to a waveguide within the group.

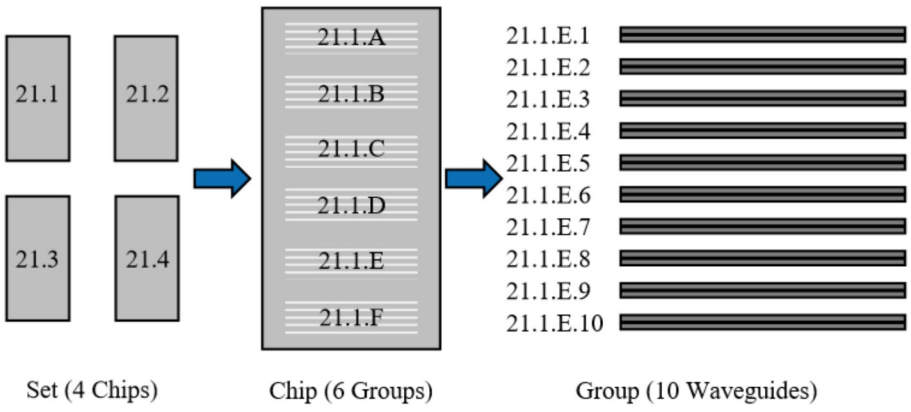


FIGURE 5.16: Distinction between a set of chips, the groups on a chip, and waveguides in a group.

#### 5.6.2.1 Sample Set 21

Following the lithographical definition of waveguides with widths 2 µm, 3 µm and 4 µm, crystallisation was carried out on test sections at speeds of 0.1 mm s$^{-1}$ and 1 mm s$^{-1}$ with $P_{Las} = 600$ mW and $\theta_{\lambda/2}$ between 20° and 45° in 5° increments, giving incident powers listed in Table 5.2. Microscope images of the test sections are shown in Figure 5.17. At $v = 0.1$ mm s$^{-1}$, annealing at 182 mW or higher resulted in full melting and reflow for all waveguide widths, and ablation occurred at $P_{Sample} \geq 336$ mW. At 1 mm s$^{-1}$, the reflow threshold was 240 mW, and ablation was not observed in the tested power range. The waveguide width was not seen to cause any change in the incident power thresholds for reflow or ablation, however the incident power steps of $\sim 50$ mW are significantly higher than in previous work. Examination of the test sections by optical microscopy showed that the best results were obtained with 285 mW at 0.1 mm s$^{-1}$ and 358 mW at 1 mm s$^{-1}$, and so waveguides were fabricated with these conditions.

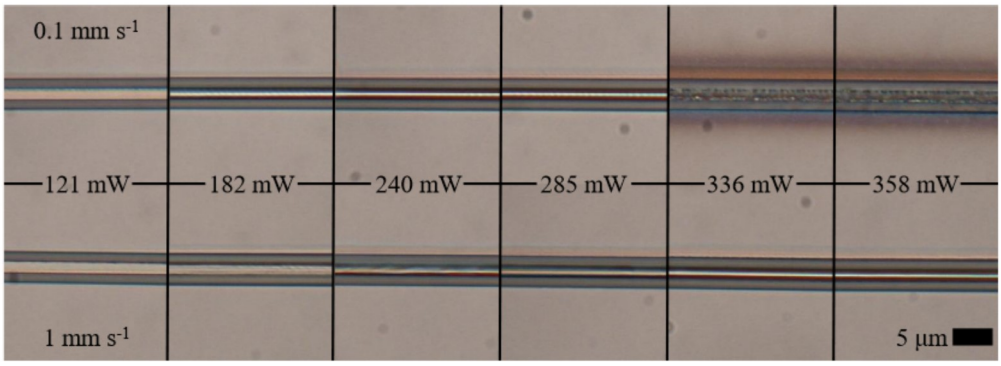


FIGURE 5.17: Annealing tests on 3 µm waveguides at 0.1 mm s$^{-1}$ (top row) and 1 mm s$^{-1}$ (bottom row).

Raman spectroscopy was used to investigate the material quality, as described in Section 5.4.2. The highest crystalline fraction was observed in a 3 µm waveguide crystallised with incident laser power 285 mW and scanning speed 0.1 µm, with a FWHM of 2.72 cm$^{-1}$ and peak position 517.5 cm$^{-1}$. Comparison of this Raman peak to a crystalline reference is shown in Figure 5.18. The peak position is attributed to residual stress as discussed above, while the FWHM indicates that the measured region of the waveguide is nearly pure c-Si. To determine the uniformity of the material produced by this process, a series of 137 spectra were collected along a waveguide at 1 µm intervals. The polySi peaks for each point are shown in Figure 5.19a. The FWHM of each spectrum was calculated, and an average deviation from the mean of 4.1% was found, indicating a high uniformity over the measured length. The FWHM at each point is shown in Figure 5.19b. The selected point at 135 µm is a fitting error, as it shows a FWHM lower than the c-Si reference (horizontal black line at 2.7 cm$^{-1}$). The initial 15 points are also high due to fitting errors and were therefore ignored for the calculation of the deviation, but have been included for completeness.

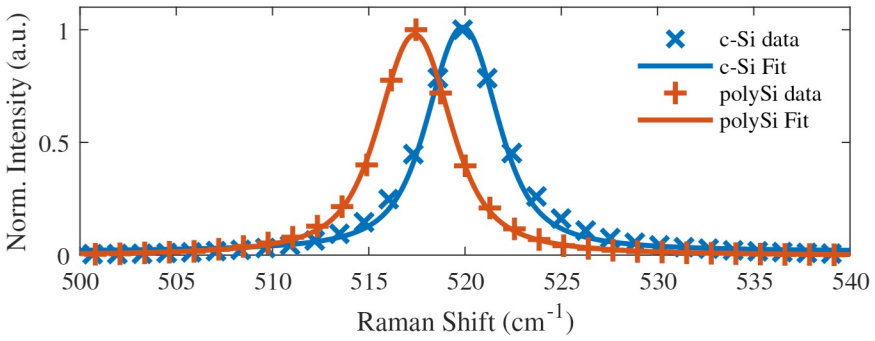


FIGURE 5.18: Comparison of Raman spectra from a crystalline reference (FWHM 2.7 $\mathrm{cm}^{-1}$) and a highly-crystalline polysilicon waveguide (FWHM 2.72 $\mathrm{cm}^{-1}$).

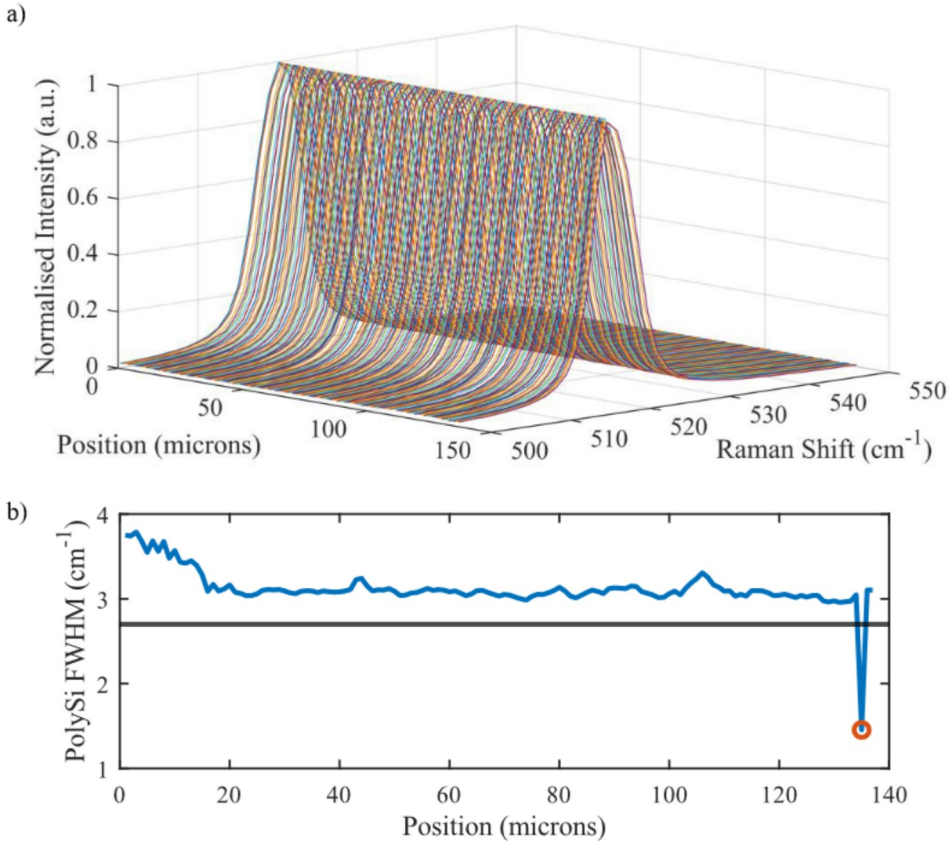


FIGURE 5.19: a) Raw data and b) calculated FWHM of 137 Raman spectra taken along a polysilicon waveguide at intervals of 1 µm. The FWHM are compared to the c-Si reference (horizontal black line). The high FWHM at points 1-15 and the low value at point 135 are known to result from fitting errors.

Following laser crystallisation and initial material quality assessment by Raman spectroscopy and microscope inspection, the optical transmission losses of the waveguides at 1550 nm was measured by the cutback process. Facets were prepared by mechanical cleaving and the input and output powers were measured using the setup shown in Figure 3.10. At each step of the cutback process, approximately 3 mm was removed from

the output facet end of the sample, keeping the input facet constant to minimise the variation in the coupled input power. This process was repeated at a range of waveguide lengths, and the transmission and coupling loss were calculated from the gradient and y-intercept of the linear fit to the data. The lowest observed losses for each set of parameters used when processing this sample were: $(3.98 \pm 0.73)\,\mathrm{dB\,cm^{-1}}$ in a 3 µm waveguide crystallised at $0.1\,\mathrm{mm\,s^{-1}}$ with $P_{Sample} = 285\,\mathrm{mW}$, $(10.06 \pm 0.33)\,\mathrm{dB\,cm^{-1}}$ for a 4 µm waveguide crystallised with $0.1\,\mathrm{mm\,s^{-1}}$ and 285 mW, and $(10.53 \pm 0.33)\,\mathrm{dB\,cm^{-1}}$ for 4 µm, $1\,\mathrm{mm\,s^{-1}}$ and 358 mW. These loss measurements are shown in Figure 5.20. Optical coupling was also attempted on non-crystallised a-Si waveguide structures, however no output light was observed at any waveguide length. As total losses of up to 50 dB were measured in polySi waveguides, the total loss in a-Si is assumed to be significantly higher than this.

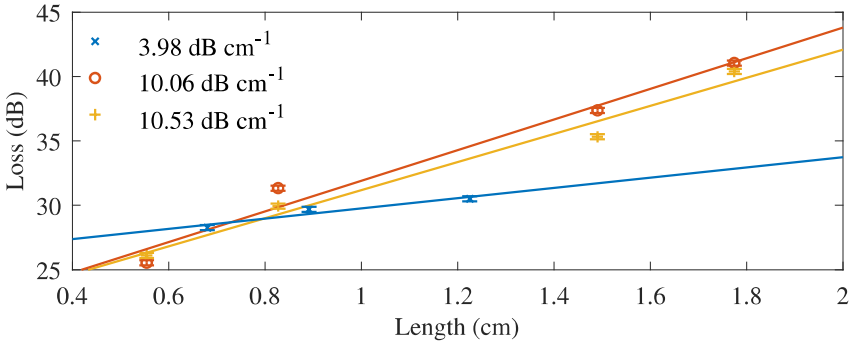


FIGURE 5.20: Lowest measured linear losses from each processing parameter set, with waveguide widths of 3, 4 and 4 µm respectively.

As previously reported, the largest crystal growth under CWLA occurs when material temperatures approach the ablation threshold [100]. This carries associated risks, discussed in Section 5.4.1, whereby minor fluctuations in the incident power, or external surface contaminants, cause damage to the waveguide during crystallisation. This, as well as the damage which occurred during the polishing process, meant that transmission losses were not obtained for the majority of manufactured waveguides. Additionally, the cutback method assumes a constant overall coupling loss. The inconsistencies from the cleaving process, and the accumulation of scattering points on the waveguide surface, meant that many waveguides produced inconsistent and unreliable results. Finally, the sensitivity of the material quality to the crystallisation conditions meant that low transmission losses were observed in only a small number of waveguides. Full loss data from all successfully characterised waveguides is presented in Appendix A, which lists the dimensions, processing conditions, and transmission and coupling losses of each.

The measurement of the lowest losses in waveguides with initial width 3 µm, crystallised with incident power 285 mW and laser scanning speed $0.1\,\mathrm{mm\,s^{-1}}$ is contrary to the observations of Healy et al. in fiber geometries, who observed the lowest losses in fibers annealed at higher speeds [34]. Based on this fiber work, and on investigations by

Michaud et al. who identified an optimum scanning speed of $7\,\mathrm{cm\,s^{-1}}$ [100], higher scanning speeds were investigated. Laser crystallisation was carried out on planar regions to determine an approximate incident power threshold at speeds of $1\,\mathrm{mm\,s^{-1}}$ and $10\,\mathrm{mm\,s^{-1}}$, however at these speeds an oscillation in the beam path was observed. This was more significant at higher speeds, and so only $1\,\mathrm{mm\,s^{-1}}$ was selected for further investigation. Waveguides with width $2\,\mu\mathrm{m}$ were crystallised at $1\,\mathrm{mm\,s^{-1}}$ with incident powers of up to 392 mW, however the lowest measured loss in these waveguides was $(9.22 \pm 0.76)\,\mathrm{dB\,cm^{-1}}$. These losses are believed to result from the fluctuations in the beam position during crystallisation, that likely resulted in an uneven surface and therefore high scattering. A microscope image of an unstable waveguide surface is shown in Figure 5.21a, and the measured $(9.22 \pm 0.76)\,\mathrm{dB\,cm^{-1}}$ losses are shown in Figure 5.21b.

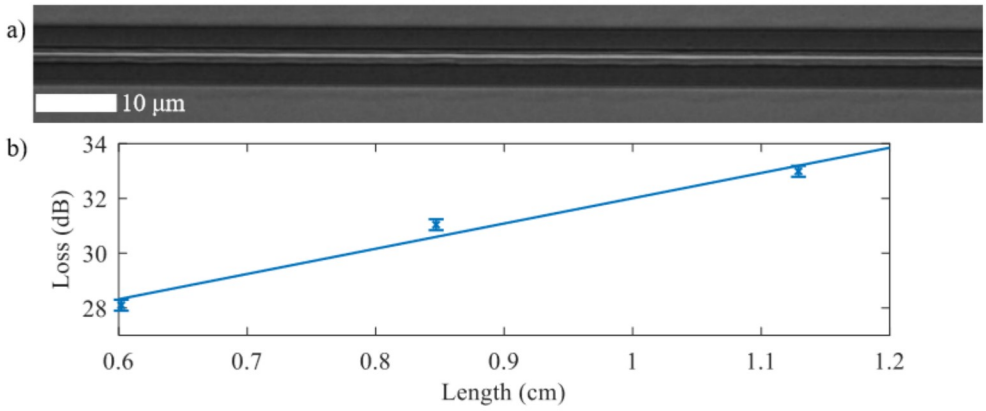


FIGURE 5.21: a) Waveguide structural instability and b) measured loss in a $2\,\mu\mathrm{m}$ waveguide crystallised at $1\,\mathrm{mm\,s^{-1}}$ and incident power 358 mW.

As discussed in Section 5.4.1, the inconsistent beam position is now known to be a technical issue with the equipment in use at the time, and so the use of higher annealing speeds remains a possible avenue of further investigation. Although the problem has been resolved, this was only achieved after the work reported in this thesis had concluded. Additionally, the amorphous silicon deposition stage for these samples was significantly before the crystallisation stage ($>$ 6 months). The effect of such a delay between deposition and crystallisation is unknown, however such an investigation may offer a greater understanding of the connections between amorphous and polycrystalline material quality. Additionally, Healy et al. partly attribute their large crystal grains and associated low losses to the confinement offered by the fiber geometry. To study this in the planar systems examined in this work, the low-temperature deposition of a silica layer on top of the a-Si wires before crystallisation would simulate the fiber confinement, however the laser crystallisation process will need alteration for optimum waveguide performance.

#### 5.6.2.2 Sample Set 23

To help verify the previously observed low transmission losses in the polysilicon waveguides, a second set of waveguides was fabricated with an etched width of 3 µm. These were then crystallised at 0.1 mm s$^{-1}$ with $P_{Sample} = 285$ mW. The waveguides were then studied using Raman spectroscopy and by taking optical transmission measurements.

Cutback transmission measurements at $\lambda = 1550$ nm indicated the lowest reported losses in polysilicon, with transmission below 4 dB cm$^{-1}$ in five waveguides. Although this was only observed in a small number of waveguides (full results in Appendix A) due to the manufacturing sensitivities previously discussed, these results show that polysilicon manufactured by laser crystallisation of amorphous silicon can exhibit transmission approaching values associated with single-crystal silicon waveguides. Figure 5.22 and Table 5.3 show the results from the low-loss waveguides, confirming initial observations discussed in Section 5.6.2.1.

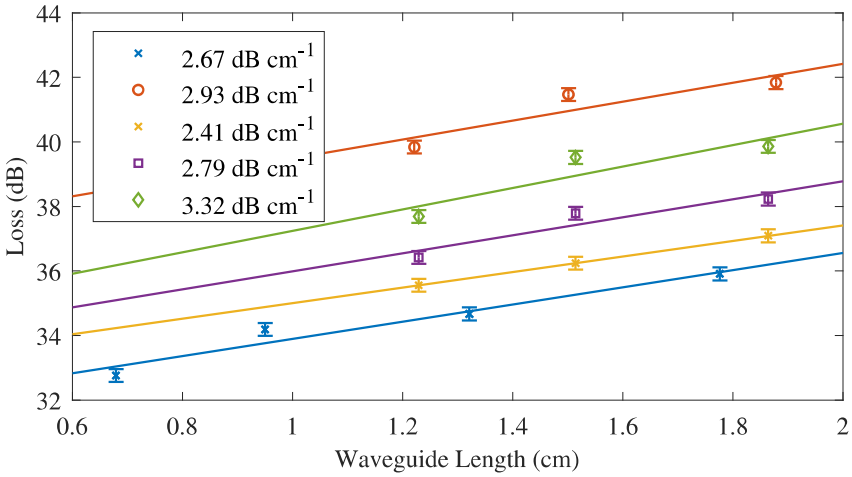


FIGURE 5.22: Linear losses observed in 3 µm waveguides processed at 0.1 mm s$^{-1}$ with incident power 285 mW.

| **Waveguide ID** | **Propagation Loss** (dB cm$^{-1}$) | **Coupling Loss** (dB) |
|---|---|---|
| 23.1.C.4 | $2.67 \pm 0.36$ | 31.23 |
| 23.2.B.6 | $2.93 \pm 0.61$ | 36.56 |
| 23.2.E.7 | $2.41 \pm 0.63$ | 32.59 |
| 23.2.E.8 | $2.79 \pm 0.63$ | 33.13 |
| 23.2.E.9 | $3.32 \pm 0.63$ | 33.91 |

TABLE 5.3: Transmission and coupling losses in waveguides with $\alpha_{\mathrm{dB}} < 5$ dB cm$^{-1}$. For all waveguides, the width was 3 µm, incident power was 285 mW and scanning speed was 0.1 mm s$^{-1}$.

As increased crystal grain size correlates with a decreased material fraction of amorphous silicon, there should in turn be a connection between the grain size and both the linear

loss and the Raman FWHM recorded for a polysilicon waveguide. Increased amorphous content results in a higher density of dangling bonds and defect sites at which light can be scattered or absorbed, and the greater variation in Si-Si bond length will broaden the Lorentzian material response. By extension, a correlation is expected between the linear loss and the Raman peak shape, albeit with some inherent uncertainty as discussed above due to the large crystal grains. To investigate this, Raman spectroscopy measurements were carried out on waveguides from groups 23.2.C and 23.2.E, the linear losses of which are listed in Appendix A and ranged from $2.4\,\mathrm{dB\,cm^{-1}}$ to $13.7\,\mathrm{dB\,cm^{-1}}$. These were compared to the Raman Lorentzian FWHM, which was calculated using the method described in Section 5.4.2. The results where a FWHM below $3.15\,\mathrm{cm^{-1}}$ was found are shown in Figure 5.23.

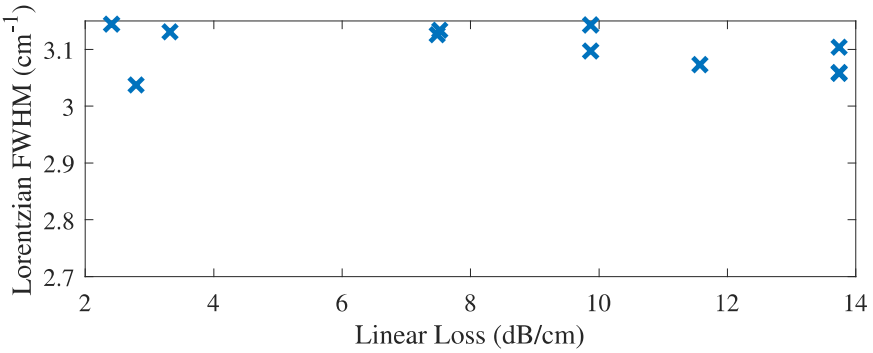


FIGURE 5.23: Linear loss and Raman FWHM in polysilicon waveguides of width 3 µm crystallised with $P_{Sample} = 285\,\mathrm{mW}$ and $v = 0.1\,\mathrm{mm\,s^{-1}}$.

No direct pattern was observed, contradicting expectations. Low FWHM were observed in low and high loss waveguides, indicating that a single Raman measurement cannot be relied upon to give an accurate picture of a waveguides performance. Multiple spectra were captured on two waveguides, with losses of $(9.87 \pm 0.66)\,\mathrm{dB\,cm^{-1}}$ and $(13.74 \pm 0.66)\,\mathrm{dB\,cm^{-1}}$, to compare the variation in the FWHM of these to that calculated in a low-loss waveguide previously. An average deviation of $\sim 5\%$ from the mean of $3.19\,\mathrm{cm^{-1}}$ was seen in the FWHM. This is higher than the previously calculated 4.1% variation in a waveguide of loss $\sim 4\,\mathrm{dB\,cm^{-1}}$, suggesting that crystal grain boundaries occur with greater frequency, increasing the proportion of spectra that are taken on grain ends. Therefore, the Raman FWHM may be significantly different on the same waveguide depending on whether the investigated region is at the end of or the middle of a crystal grain. This increased presence of grain boundaries will also increase scattering and absorption, corresponding to the higher measured linear loss in these waveguides. However, the variation present in Raman results ultimately mean that the only conclusive indication of a waveguide's suitability for photonic applications is its linear loss.

## 5.7 Conclusions

By carrying out localised continuous-wave laser annealing of low-temperature deposited amorphous silicon, the fabrication of high-quality back-end-of-line CMOS compatible polysilicon waveguides has been achieved. Large-grain polysilicon has been observed from material characterisation by Raman spectroscopy and X-ray diffraction crystallography. The lowest FWHM of the polysilicon Raman peak was $2.72\,\mathrm{cm}^{-1}$, compared to the monocrystalline reference value of $2.7\,\mathrm{cm}^{-1}$, indicating nearly fully crystalline material. XRD measurements showed crystals with lengths of up to 1.6 mm, consistent with previous measurements of waveguides fabricated by the same process [35]. Transmission loss measurements at $\lambda = 1.55\,\mu\mathrm{m}$ demonstrated losses of $(2.41 \pm 0.63)\,\mathrm{dB\,cm}^{-1}$ in a 3 µm wide waveguide crystallised with a scanning speed of $0.1\,\mathrm{mm\,s}^{-1}$ and incident power 285 mW. Furthermore, losses below $4\,\mathrm{dB\,cm}^{-1}$ were measured using the same parameters in a further five waveguides, demonstrating the repeatability of this manufacturing process. These are the lowest transmission losses in comparable polysilicon waveguides, and approach the $< 2\,\mathrm{dB\,cm}^{-1}$ observed in monocrystalline silicon. Other waveguides were fabricated by the same technique using different dimensions and processing parameters, with the resulting losses summarised in Table 5.4. In comparison to the observed losses below $4\,\mathrm{dB\,cm}^{-1}$, the lowest loss reported in waveguides of comparable dimensions fabricated by oven annealing was $\sim 5\,\mathrm{dB\,cm}^{-1}$ in high-temperature oven-annealed polysilicon [42], and the previous lowest reported loss in low-temperature laser-crystallised polysilicon was $5.31\,\mathrm{dB\,cm}^{-1}$ [35]. The reduction in losses by this technique are attributed to increased laser stability, larger waveguide dimensions and improved uniformity of material quality. Further optimisation of the crystallisation process is anticipated to reduce the polysilicon losses to around $1\,\mathrm{dB\,cm}^{-1}$.

| **Waveguide Width** (µm) | **Laser Power** (mW) | **Scanning Speed** ($\mathrm{mm\,s}^{-1}$) | **Loss** ($\mathrm{dB\,cm}^{-1}$) |
|---|---|---|---|
| 2 | 358 | 1 | 9.2 |
| 3 | 285 | 0.1 | 2.4 |
| 4 | 258 | 0.1 | 10 |
| 4 | 358 | 1 | 10.5 |

TABLE 5.4: Lowest measured losses in waveguides fabricated by direct CW laser annealing across a range of waveguide and laser processing parameters.

# Chapter 6

# Nonlinear Optics in Polysilicon Waveguides

With significant recent advances in reducing the optical loss of polysilicon and the development of BEOL-CMOS-compatible manufacturing techniques, the logical continuation is to examine the suitability of these waveguides for nonlinear optical processing to expand their potential range of applications. Following the measurement of record low losses in polysilicon, as reported in Chapter 5, this chapter will detail the work undertaken to demonstrate and characterise third-order nonlinear propagation in polysilicon waveguides, in addition to presenting the necessary theoretical background.

## 6.1 Introduction

Silicon as a material is well-suited to nonlinear photonics. Its high linear refractive index compared to standard cladding materials enables excellent confinement of light in waveguides with a small cross-section, easing access to the high optical intensities required for nonlinear propagation [125], [126]. When combined with the high nonlinear refractive index, the suitability of silicon for nonlinear applications is clear.

The applications of nonlinear photonics in silicon are broad ranging in scope and impact. A multitude of effects have been demonstrated in recent years in both fiber and on-chip geometries, including signal processing [59], [127]–[131], sensing for chemical and biological applications [132]–[134], lasing and light amplification [11], [57], [135]–[137], and supercontinuum generation [62], [138]–[141].

As thorough as these investigations have been into the use of c-Si platforms for nonlinear photonics, the high linear losses have thus far prevented such work in polysilicon-based planar waveguides. As previously discussed in Section 5.1, the development of

CMOS-compatible polysilicon as a low-loss optical material would enable a wide array of improvements to existing optoelectronic systems due to its enhanced deposition flexibility.

The low polysilicon losses reported in the preceding chapter are, however, low enough that the observation of nonlinear effects was anticipated. This chapter will detail the relevant background theory, experimental work and results of third-order nonlinear measurements on polysilicon waveguides.

## 6.2 Theory of Nonlinear Optics

Nonlinear optical processes result from the changes to the material polarisation in the presence of a high-intensity electric field. Two effects are of interest to this thesis, the third-order nonlinear processes of two-photon absorption (TPA) and self-phase modulation (SPM). This section will discuss the theory behind these effects and their effect on an optical pulse, and introduce a nonlinear figure of merit that is used to compare the nonlinear properties of a material.

In the low-intensity regime, Equation 6.1 expresses the linear relation between the polarisation $\mathbf{P_0}$ of a material and an applied external electric field $\mathbf{E}$:

$$\mathbf{P_0} = \varepsilon_0 \chi^{(1)} \mathbf{E}, \tag{6.1}$$

where $\varepsilon_0 = 8.854 \times 10^{-12}\,\mathrm{F\,m^{-1}}$ is the vacuum permittivity and $\chi^{(1)}$ is the first order electric susceptibility of the medium. The susceptibility is a complex term and is related to the complex refractive index by $\chi^{(1)} + 1 = n^2$. The real part relates to the real refractive index, while the imaginary part is associated with the attenuation coefficient, by the relations

$$n(\omega) = 1 + \frac{1}{2}\mathrm{Re}\left(\tilde{\chi}^{(1)}(\omega)\right) \tag{6.2a}$$

$$\alpha(\omega) = \frac{\omega}{nc}\mathrm{Im}\left(\tilde{\chi}^{(1)}(\omega)\right), \tag{6.2b}$$

where $\tilde{\chi}^{(1)}(\omega)$ is the Fourier transform of $\chi^{(1)}(t)$.

At higher electric field intensities, the linear relationship is no longer accurate, and the full expression

$$\mathbf{P} = \mathbf{P_0} + \delta\mathbf{P_{FC}} + \mathbf{P_{NL}}, \tag{6.3}$$

must be used [142]. The complete expression for polarisation $\mathbf{P}$ is the summation of $\mathbf{P_0}$, the free carrier contribution $\delta\mathbf{P_{FC}}$ and the nonlinear polarisation

$$\mathbf{P_{NL}} = \varepsilon_0 \left[ \chi^{(2)}\mathbf{E}^2 + \chi^{(3)}\vdots\mathbf{E}^3 + \dots \right] \tag{6.4}$$

$\chi^{(j)}$ is the $j^{th}$ order susceptibility, a tensor of rank $j+1$. The magnitude of $\chi^{(j)}$ decreases as $j$ increases, so progressively higher intensities are required to access higher order nonlinear effects. Furthermore, $\chi^{(2)}$ is suppressed due to symmetry in centrosymmetric structures such as silicon. Therefore, only the $\chi^{(3)}$ term is of interest in this thesis. Expansion of the $\chi^{(3)}$ term from Equation 6.4 results in a series of terms which can be grouped by the effects that they cause. These effects are SPM, cross-phase modulation (XPM), third-harmonic generation (THG) and four-wave mixing (FWM). The term giving rise to SPM also results in TPA. XPM, THG and FWM are not considered in this work, as they either require multiple pump wavelengths or phase matching to be efficient at the intensities used in this work.

The effects of TPA and SPM can be introduced via modification to the complex refractive index as

$$n = n_0 + n_2 I - i\frac{\lambda}{4\pi}\left(\alpha_0 + \beta_{\mathrm{TPA}} I\right) \tag{6.5}$$

where $I$ is the pulse intensity, $n_0$ is the linear refractive index, and $\lambda$ is the pulse wavelength. SPM is associated with the nonlinear Kerr coefficient $n_2$, while TPA is connected to the TPA coefficient $\beta_{\mathrm{TPA}}$. These are related to the real and imaginary parts of the third-order susceptibility by

$$n_2 = \frac{1}{cn_0^2\varepsilon_0}\frac{3}{4}\mathrm{Re}\left(\chi^{(3)}\right) \tag{6.6a}$$

$$\beta_{\mathrm{TPA}} = \frac{\omega}{c^2 n_0^2 \varepsilon_0}\frac{3}{2}\mathrm{Im}\left(\chi^{(3)}\right) \tag{6.6b}$$

where $c$ is the speed of light, $n_0$ is the linear refractive index, and $\omega$ is the frequency of the electromagnetic wave which is inducing the nonlinearity.

### 6.2.1 Two-Photon Absorption

The simultaneous absorption of two photons can excite an electron across the bandgap from the valence to the conduction band, as shown in Figure 6.1. Where these photons have the same wavelength, this is referred to as degenerate TPA.

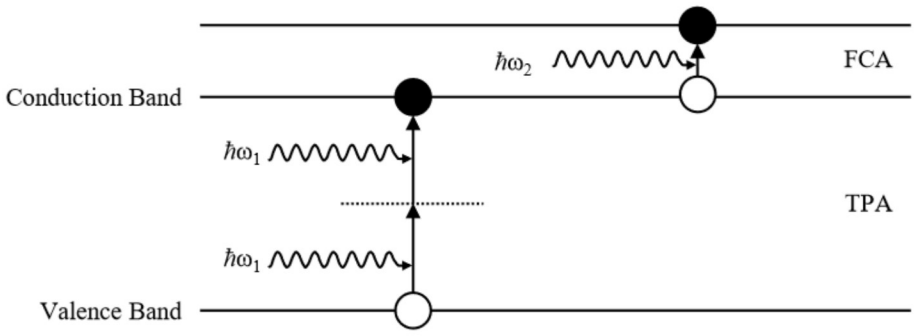


FIGURE 6.1: Energy level diagram for degenerate two photon absorption, in which two photons of equal energy are absorbed to excite an electron across the bandgap, making it available for further excitation by free-carrier absorption.

Once in the conduction band, the absorption of further photons can cause additional excitation, in a process known as free-carrier absorption (FCA). The total change in intensity from these processes is given by

$$\frac{dI(z,t)}{dz} = -\beta_{\mathrm{TPA}} I^2(z,t) - \sigma_{\mathrm{FCA}} N(z,t) I(z,t) \tag{6.7}$$

where $I(z,t) = |A(z,t)|^2/A_{\mathrm{eff}}$ is the intensity of a pulse $A(z,t)$ over the effective mode area $A_{\mathrm{eff}}$, $\sigma_{\mathrm{FCA}}$ is the FCA coefficient, and the free-carrier density $N(z,t)$ is found by solving the rate equation

$$\frac{\partial N(z,t)}{\partial t} = \frac{\beta_{\mathrm{TPA}}}{2h\nu} I^2(z,t) - \frac{N(z,t)}{\tau}. \tag{6.8}$$

Here, $h\nu$ is the photon energy and $\tau$ is the free-carrier lifetime. In Equation 6.7, the first term is loss from TPA, while the second is loss from FCA. The first term in Equation 6.8 represents the excitation of electrons by TPA into the conduction band, increasing the population available for FCA. The second term is the relaxation of those excited carriers back to the valence band. The net effect of TPA and FCA is an intensity-dependent reduction in the optical intensity of a transmitted signal. Higher intensities cause greater absorption, due to both the increased rate of excitation across the bandgap due to TPA and the consequent increased availability of conduction-band free carriers which can absorb through FCA.

### 6.2.2 Self-Phase Modulation

The phenomenon of SPM arises from the change to the refractive index at high intensities caused by the nonlinear Kerr coefficient. This nonlinear contribution results in a phase shift, generating new frequency components as a pulse propagates. These

new components then generate an additional phase shift, and the pulse broadens as it propagates. To calculate the resulting spectral broadening, the nonlinear Schrödinger equation (NLSE) must be solved [62].

$$\frac{\partial A(z,t)}{\partial z} = -i\frac{\beta_2}{2}\frac{\partial^2 A(z,t)}{\partial t^2} + i\gamma|A(z,t)|^2 A(z,t) - \frac{1}{2}(\sigma+\alpha)A(z,t) \tag{6.9}$$

where $\beta_2$ is the group velocity dispersion parameter, $\alpha$ is the linear loss, $\sigma$ is the net free carrier contribution [143], and the nonlinear parameter $\gamma$ is given by

$$\gamma = \frac{k_0 n_2}{A_{\text{eff}}} + i\frac{\beta_{\text{TPA}}}{A_{\text{eff}}} \tag{6.10}$$

where $k_0$ is the wavenumber of the pulse.

The first term in the NLSE governs the dispersion of an optical pulse, as described in Section 2.4.3, the second applies the nonlinear effects of SPM and TPA, and the third covers the reduced pulse intensity from linear loss and free-carrier absorption. The defining characteristic of SPM is the nonlinear Kerr coefficient $n_2$. To simulate the broadening of a pulse as it travels through a waveguide, the nonlinear Schrödinger equation is solved using the split-step Fourier transform method described by Agrawal [144]. For this work, a Matlab code was used in which the value of $n_2$ was varied to obtain an accurate fit to the experimental data. Equation 6.9 can be broken down into three terms, the dispersion ($\hat{D}$), nonlinear ($\hat{N}$) and loss ($\hat{L}$) components, such that

$$\frac{\partial A(z,t)}{\partial z} = \hat{D} + \hat{N} + \hat{L}, \tag{6.11}$$

where

$$\hat{D} = -i\frac{\beta_2}{2}\frac{\partial^2 A(z,t)}{\partial t^2} \tag{6.12a}$$

$$\hat{N} = i\gamma|A(z,t)|^2 A(z,t) \tag{6.12b}$$

$$\hat{L} = -\frac{1}{2}(\sigma+\alpha)A(z,t) \tag{6.12c}$$

To calculate the pulse evolution, the length of the waveguide is broken down into short sections. In each section, the three terms of the NLSE are applied to the pulse. The dispersion and nonlinear terms act to alter the pulse profile, and the loss term reduces the intensity. The modified pulse is then used as the input for the calculations for the following length section of the waveguide. The value of $n_2$ is iteratively modified in the

code to obtain a close fit to the observed experimental spectral broadening for all input powers.

### 6.2.3 Nonlinear Figure of Merit

SPM results in the spectral broadening of an optical pulse, and is desirable due to the resulting applications in supercontinuum generation and signal processing steps such as signal regeneration [145] or wavelength conversion [146]. In contrast, TPA decreases the signal intensity, which most commonly degrades the performance of a nonlinear device. It is, however, sometimes useful for applications such as all-optical modulation [147]. To provide a measure for the overall quality of a material for nonlinear applications, the nonlinear figure of merit is defined as

$$\mathrm{FOM_{NL}} = \frac{1}{\lambda}\frac{n_2}{\beta_{\mathrm{TPA}}}. \tag{6.13}$$

In crystalline silicon at standard telecommunications wavelengths, the figure of merit has been measured between 0.32 and 0.86 [148]–[150]. These values provide a target range against which nonlinear measurements in this thesis will be compared. Higher values of the $\mathrm{FOM_{NL}}$ are indicative of better nonlinear performance, as the limitations resulting from TPA will be lower relative to the broadening from SPM.

## 6.3 Experimental Process

Nonlinear characterisation was carried out using a similar setup to that used for the linear loss measurements, however the CW laser was replaced with a pulsed source to obtain the necessary high intensities required to observe nonlinear propagation.

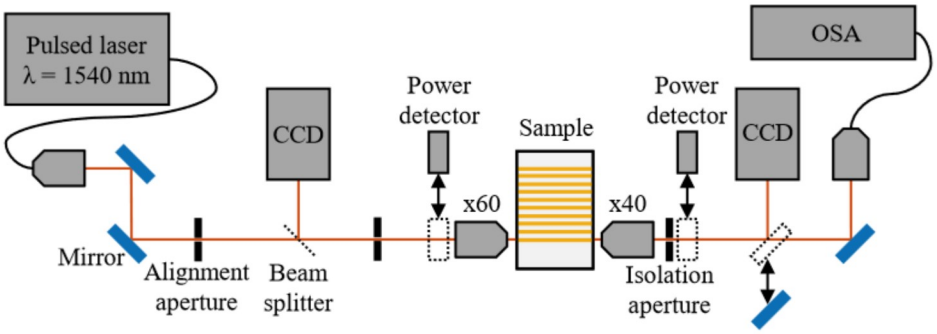


FIGURE 6.2: Setup for nonlinear characterisation of waveguides. 1540 nm pulsed light is coupled into waveguides. Two-photon absorption measurements use powermeters before and after the waveguides, while the output is directed into an optical spectrum analyser to observe self-phase modulation.

The laser source used was a Onefive ORIGAMI pulsed laser, emitting at 1540 nm. This is close enough to the wavelength used for linear loss measurements that the measurements remain valid. The pulses have a hyperbolic secant profile, with a temporal FWHM of 750 fs and a repetition rate of 40 MHz. This pulse repetition rate allows free carrier accumulation to be ignored in calculations, as the material relaxation time ($\tau_c \approx 1$ ns) is significantly faster than the pulse interval (25 ns). The nonlinear transmission setup is shown in Figure 6.2. As before, CCD cameras before and after the coupling objectives were used for beam focusing and coupling, and power detectors before the input objective and after the output isolation aperture were used to measure input and output powers. The most significant change is the option to couple the output light into an optical spectrum analyser (OSA). This enabled the recording of the spectral composition of the pulses after transmission.

### 6.3.1 Nonlinear Loss Measurements and Simulations

As described in Section 6.2.1, the influence of $\beta_{\mathrm{TPA}}$ on pulse transmission is dependent on the pulse intensity. Therefore, an estimation of $\beta_{\mathrm{TPA}}$ can be obtained from measurements of the output power of a waveguide at a range of input powers. As the transmitted intensity increases, the absorption from TPA and FCA will also increase according to Equation 6.7. Measurement of the TPA characteristics was carried out using the setup shown in Figure 6.2. The powermeters were used to record the average input ($P_{\mathrm{in,av}}$) and output ($P_{\mathrm{out,av}}$) power. The input power was varied using an attenuator, with $P_{\mathrm{in,av}}$ ranging from $\sim$0.1 mW to $\sim$65 mW. As the transmitted intensity increases, the loss from TPA and FCA increases, producing a characteristic curve which is approximately linear at low powers and nonlinear at high powers. These measurements can then be compared with the curve obtained from simulations of the pulse intensity along the waveguide length. For short waveguide lengths, the dispersion can be ignored, producing a simplified NLSE which only describes the temporal evolution of the pulse intensity. This takes the same form as Equation 6.7, plus a term for the linear loss, giving Equation 6.14. Ignoring spectral broadening, the equation

$$\frac{dI(z,t)}{dz} = -\alpha I(z,t) - \beta_{\mathrm{TPA}} I^2(z,t) - \sigma_{\mathrm{FCA}} N_c(z,t) I(z,t) \tag{6.14}$$

can be solved along the waveguide length using the split-step Fourier method [52]. As stated before, $N_c$ is calculated using Equation 6.8. The simulations of the intensity change were carried out using a script developed within the Nonlinear Semiconductor Photonics group.

Within the script, the peak power coupled into the waveguide is calculated from the measured input average power, the pulse FWHM and repetition rate, and the estimated insertion loss. The pulse intensity is then calculated using an effective mode area, in

this case $A_{\text{eff}} = 0.6\,\mu\text{m}^2$ based on finite element method mode field calculations by Dr Joseph Campling.

The total waveguide length is then broken down into discrete sections. For the initial section, the input intensity and a user-set value of $\beta_{\text{TPA}}$ are input and used to calculate the free-carrier density, using Equation 6.8, which is in turn used to calculate the free-carrier loss contribution using the c-Si FCA coefficient $\sigma_{\text{FCA}} = 1.45 \times 10^{-21}\,\text{m}^2$ [151]. The total loss for this section of the waveguide length is then calculated according to Equation 6.14. The loss is used to calculate the reduced outgoing intensity from this section. This process is repeated for each section along the full waveguide length, taking the output intensity from each previous section, and the original value of $\beta_{\text{TPA}}$, as the inputs for each following section. This is carried out for a range of input powers up to a selected maximum, and compared to experimental data. The low-power fitting is predominantly dependent on the linear loss, while the high-power fitting is dependent on $\beta_{\text{TPA}}$.

### 6.3.2 Spectral Broadening Measurements and Simulations

SPM is a precursor to more dramatic effects such as supercontinuum generation, which has uses in a wide range of fields across spectroscopy, telecommunications, and beyond. SPM results from the intensity-dependent change in refractive index which occurs as a result of the high-intensity nonlinear response, as detailed in Section 6.2. The alteration to the refractive index induces a frequency-dependent phase shift, broadening the pulse envelope in the frequency domain, while normal dispersion results in broadening in the temporal domain. The observation of spectral broadening due to SPM is an important step towards demonstrating the potential of the manufacturing process detailed in Chapter 5 for more significant applications. Spectral broadening measurements were carried out by coupling the waveguide output light into an optical spectrum analyser (OSA) and using a range of input powers to study the evolution of the broader spectrum.

The spectra from the OSA were then compared to simulations which used the split-step Fourier method to solve the full NLSE as described in Section 6.2.2. The calculated $\beta_{\text{TPA}}$ from nonlinear absorption measurements, the linear loss $\alpha$ and an estimation of $n_2$ were used to calculate the evolution of the pulse along the waveguide length. The simulated output pulse shape was compared to that from the experimental data, and $n_2$ was refined to produce the closest fit to the data. The dispersion was obtained from simulations of the effective area and index, with $\beta_2$ having a value of $0.67\,\text{ps}^2\,\text{m}^{-1}$ in these simulations.

## 6.4 Results and Discussion

Nonlinear measurements were carried out on two waveguides. Waveguide 21.1.E.5 exhibited linear losses of $(3.98 \pm 0.73)\,\mathrm{dB\,cm^{-1}}$, while waveguide 23.2.E.7 showed the lowest losses ever reported in comparable polysilicon waveguides of $(2.41 \pm 0.63)\,\mathrm{dB\,cm^{-1}}$. Therefore, these were selected for further study. The nonlinear measurements were carried out at waveguide lengths of 1.537 cm and 1.229 cm respectively.

### 6.4.1 Waveguide 21.1.E.5

The nonlinear absorption resulting from two-photon absorption in waveguide 21.1.E.5, which had a linear loss of $(3.98 \pm 0.73)\,\mathrm{dB\,cm^{-1}}$, was measured by modulating the average input power between 0.1 mW and 63 mW. A simulated absorption across the same range was calculated, taking into account the coupling loss at the input facet. The coupling loss was calculated by subtracting the measured waveguide and objective losses from the total transmission loss at a given length. The coupling loss from the input and output facets was assumed to be equal, giving a single-facet loss of 14 dB. As previously discussed, this assumption is not ideal, due to the difference in magnification and numerical aperture of the focusing objectives. It also does not account for reflections at the input and output facets, or the mismatch between the area of the guided mode and the focused spot size of the input lens. Although both of these can be calculated, the angled facets that sometimes result from cleaving will make these inaccurate. A future goal would therefore be, as mentioned earlier, the improvement of the facet preparation technique, which would also allow more accurate determination of coupling loss and nonlinear simulations. However, based on FEM simulations of the input optical coupling carried out by Dr Ozan Aktas, the assumption of 14 dB is not unreasonable. An input coupling loss of 7 dB was calculated in a simplified system neglecting Fresnel reflection and assuming coupling to the fundamental mode only and a perfectly smooth facet. Therefore, the true input coupling losses will be closer to the assumed 14 dB.

Using the simulations described in Section 6.3, and by prioritising fitting at the upper and lower bounds (corresponding to the linear and nonlinear regimes), a value of $\beta_{\mathrm{TPA}} = 10 \times 10^{-12}\,\mathrm{m\,W^{-1}}$ was obtained by iteratively adjusting the values of $\alpha$ and $\beta_{\mathrm{TPA}}$ used to simulate the curve. The linear loss was constrained to a narrow range around the value obtained from cutback loss measurements, while the value of $\beta_{\mathrm{TPA}}$ was changed as needed. The data and fitted simulation are shown in Figure 6.3. An excellent fit to the linear regime is seen, confirming that the estimated linear loss from cutback measurements is accurate, and good agreement is also seen for data points in the nonlinear regime where the peak input power is over 30 W. The deviation from the fitted curve persisted across multiple measurements of the same waveguide, however the source was not identified. The equipment used to take the measurements was not

changed during the experiment, and the deviation was not seen in other measurements. It is therefore assumed that it resulted from some unknown source connected to the waveguide itself, but further investigation was not possible due to time constraints.

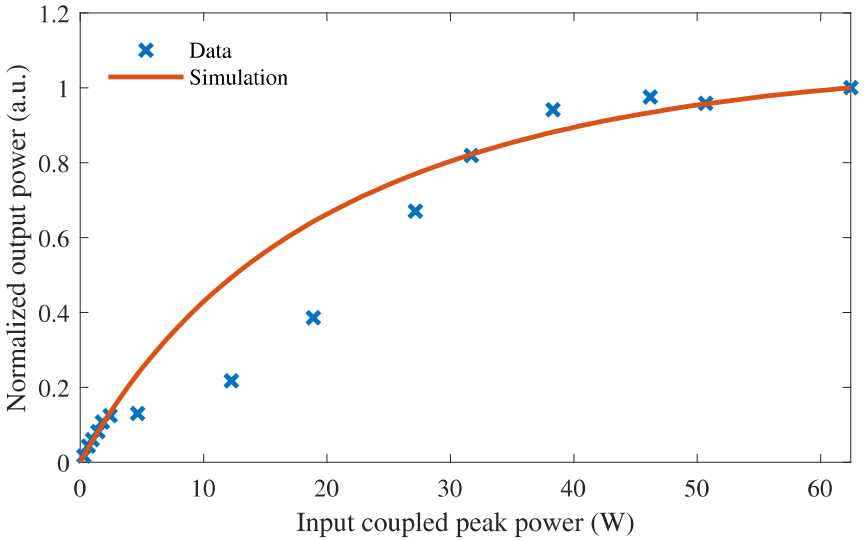


FIGURE 6.3: Nonlinear absorption in Waveguide 21.1.E.5 at length 1.537 cm. Close fitting is achieved at high and low powers with $\alpha = 4\,\mathrm{dB\,cm^{-1}}$ and $\beta_{\mathrm{TPA}} = 10 \times 10^{-12}\,\mathrm{m\,W^{-1}}$. The origin of the deviation between 5 and 25 W has not been identified.

To measure self-phase modulation, the waveguide output was directed into an optical spectrum analyser. The average input powers (as measured before the input objective) were in the range of 10 mW to 55 mW, which correspond to calculated coupled peak powers (i.e., with measured losses from the focusing objective and calculated losses from the waveguide facet subtracted) of 13 W to 72 W. The experimental data and fitted curves for the spectral measurements of the nonlinear propagation in waveguide 21.1.E.5 are shown in Figure 6.4. The simulations showed best fit with $n_2 = 4.5 \times 10^{-18}\,\mathrm{m^2\,W^{-1}}$. At peak powers above 60 W, the spectral evolution shows a characteristic dip in the intensity at the central pulse wavelength, which is a clear indicator that SPM is the driving factor behind the broadening of the pulse. The pulse peak is most affected by the phase-shift due to the intensity dependence of SPM, and therefore reduces in intensity while the surrounding frequency components increase.

To determine the nonlinear quality of the polysilicon material, the nonlinear coefficients were compared to those of crystalline silicon. The nonlinear absorption was high, with $\beta_{\mathrm{TPA}} = 10 \times 10^{-12}\,\mathrm{m\,W^{-1}}$ being higher than the values measured in c-Si, which have been reported between $4 \times 10^{-12}\,\mathrm{m\,W^{-1}}$ and $9 \times 10^{-12}\,\mathrm{m\,W^{-1}}$. The high nonlinear absorption is attributed, at least in part, to the reduction of the bandgap which results from residual strain during laser annealing, and to the amorphous material between the

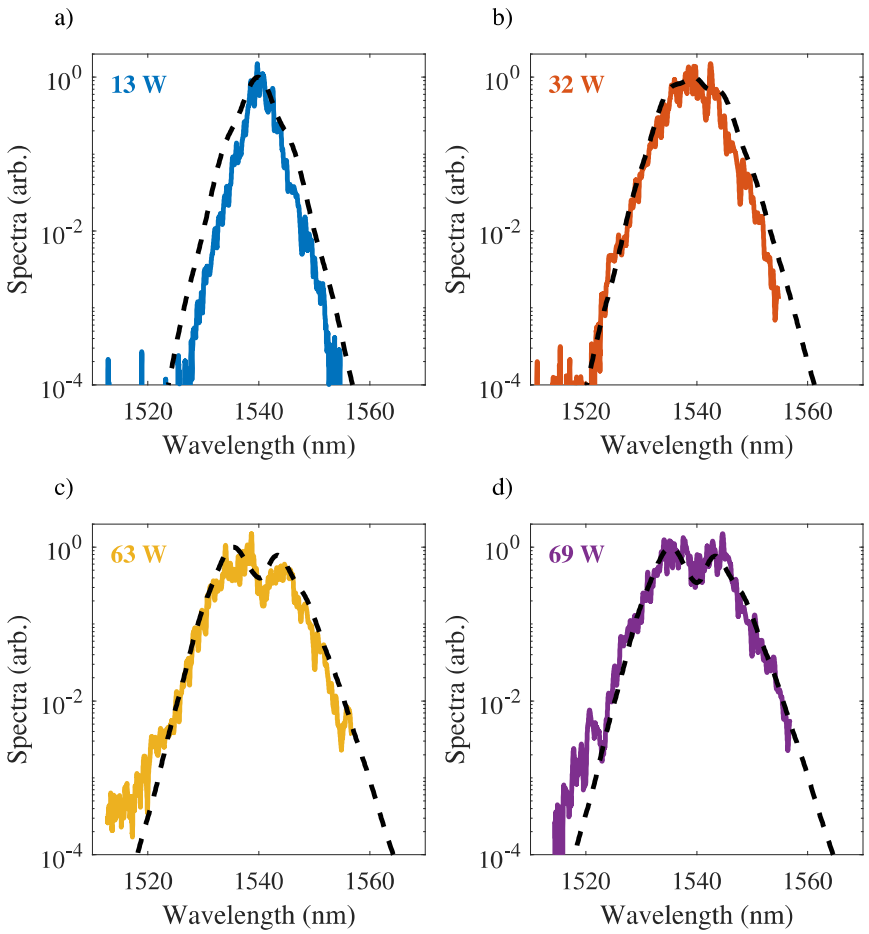


FIGURE 6.4: Simulation fit (black dashed line) to spectra showing pulse broadening in waveguide 21.1.E.5 at length 1.537 cm, and input peak powers a) 13 W, b) 32 W, c) 63 W and d) 69 W.

crystalline grains. By lowering the bandgap, the probability of TPA increases, and amorphous material introduces defect states in the bandgap which increase both the linear and nonlinear absorption. Although the strain has not been calculated, the peak shift from Raman measurements indicates that the strain is present, as discussed in Chapter 5. The high $\beta_{\mathrm{TPA}}$ is undesirable, as its effects are more significant at higher intensities where other nonlinear effects become significant, and acts to suppress these effects by reducing the total power in the waveguide. Therefore, improvement of the material quality to reduce $\beta_{\mathrm{TPA}}$ is an important avenue for future development of laser-crystallised polysilicon. The magnitude of the spectral broadening by SPM is governed by the nonlinear Kerr coefficient $n_2$. Typical c-Si values lie in the range $4.3 \times 10^{-18}\,\mathrm{m^2\,W^{-1}}$ to $6 \times 10^{-18}\,\mathrm{m^2\,W^{-1}}$, so the measured $n_2 = 4.5 \times 10^{-18}\,\mathrm{m^2\,W^{-1}}$ is within the crystalline range, albeit at the lower end. This supports previous measurements indicative of high material quality. The nonlinear FOM for this waveguide is 0.29, below the reported

values for c-Si (see Section 6.2.3), a consequence of the high $\beta_{\mathrm{TPA}}$ and low $n_2$.

### 6.4.2 Waveguide 23.2.E.7

After the demonstration of nonlinear effects in Waveguide 21.1.E.5, additional samples were fabricated as discussed in Section 5.6.2.2. As it showed the lowest transmission losses of $(2.41 \pm 0.63)\,\mathrm{dB\,cm^{-1}}$, waveguide 23.2.E.7 was chosen for further nonlinear characterisation. The values of $\beta_{\mathrm{TPA}}$ and $n_2$ were calculated from simulation fitting to experimental data as described in Section 6.3. Fitting to the nonlinear absorption curve (shown in Figure 6.5) gave a calculated $\beta_{\mathrm{TPA}} = 7 \times 10^{-12}\,\mathrm{m\,W^{-1}}$. However, in order to fit to the linear region of this data set, it was necessary to increase $\alpha$ to $3\,\mathrm{dB\,cm^{-1}}$ during the iterative fitting process. Figure 6.5b shows the difference in fitting between $2.41\,\mathrm{dB\,cm^{-1}}$ and $3\,\mathrm{dB\,cm^{-1}}$. The higher loss is closer to the experimental data. This assumed increase is not unreasonable, as there are significant uncertainties in the losses estimated via cutback due to the assumptions made about input and output coupling, and due to the cleaving process used in this work as has been previously discussed.

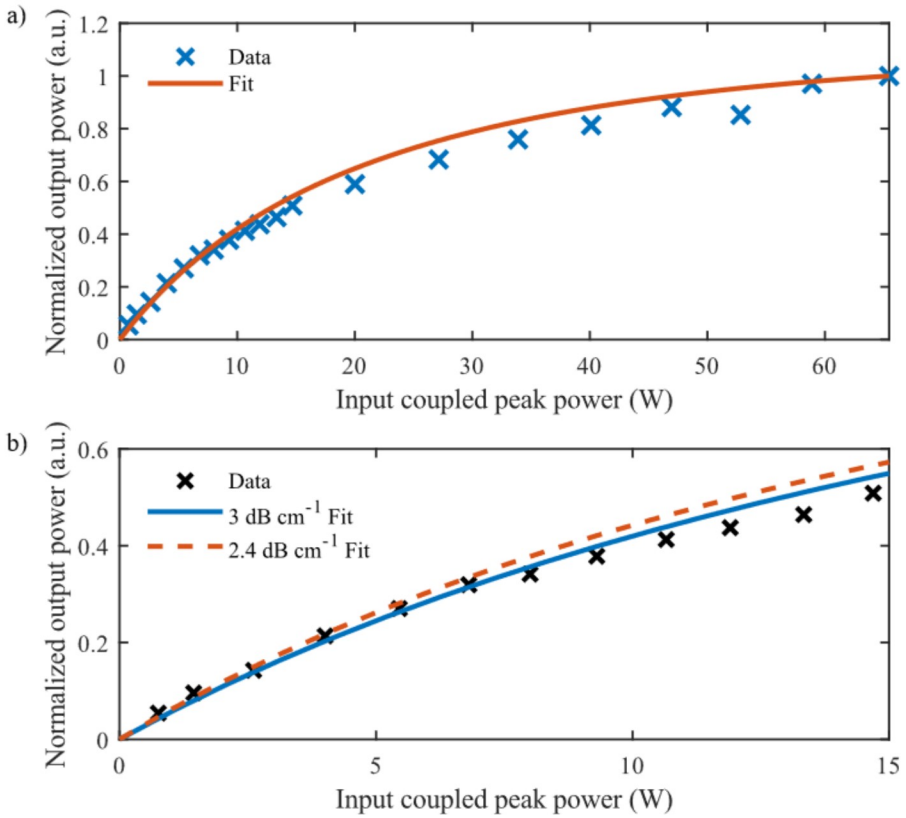


FIGURE 6.5: a) Nonlinear absorption in waveguide 23.2.E.7 at length 1.229 cm. Iterative fitting results indicate $\alpha = 3\,\mathrm{dB\,cm^{-1}}$ and $\beta_{\mathrm{TPA}} = 7 \times 10^{-12}\,\mathrm{m\,W^{-1}}$. b) Difference in linear regime fit for $\alpha = 2.41\,\mathrm{dB\,cm^{-1}}$ and $3\,\mathrm{dB\,cm^{-1}}$

SPM fitting to input peak powers from 35 W to 72 W using these parameters, shown in Figure 6.6, gave a value of $n_2 = 3.5 \times 10^{-18}\,\mathrm{m^2\,W^{-1}}$. An additional peak is visible in the higher power data at $\lambda = 1520\,\mathrm{nm}$, attributed to multimode interactions [152]. Comparison of these to crystalline references shows a high $\beta_{\mathrm{TPA}}$ and low $n_2$, likely a result of various factors, including the amorphous content of the polysilicon, the dependence of $\chi^{(3)}$ on the crystal grain orientation, and residual material stress from the crystallisation process. These would be expected to result in suppressed nonlinear effects such as spectral broadening, and so the pulse width of $>40\,\mathrm{nm}$ at maximum peak power with these coefficients suggests that improved material quality would result in significantly greater spectral broadening. The FOM with these values is 0.32, higher than was calculated for waveguide 21.1.E.5 but below the reported values in c-Si. This reduced value is caused by the low $n_2$ and high $\beta_{\mathrm{TPA}}$, as the phase shift is reduced and the nonlinear absorption is more significant than in previously measured waveguides.

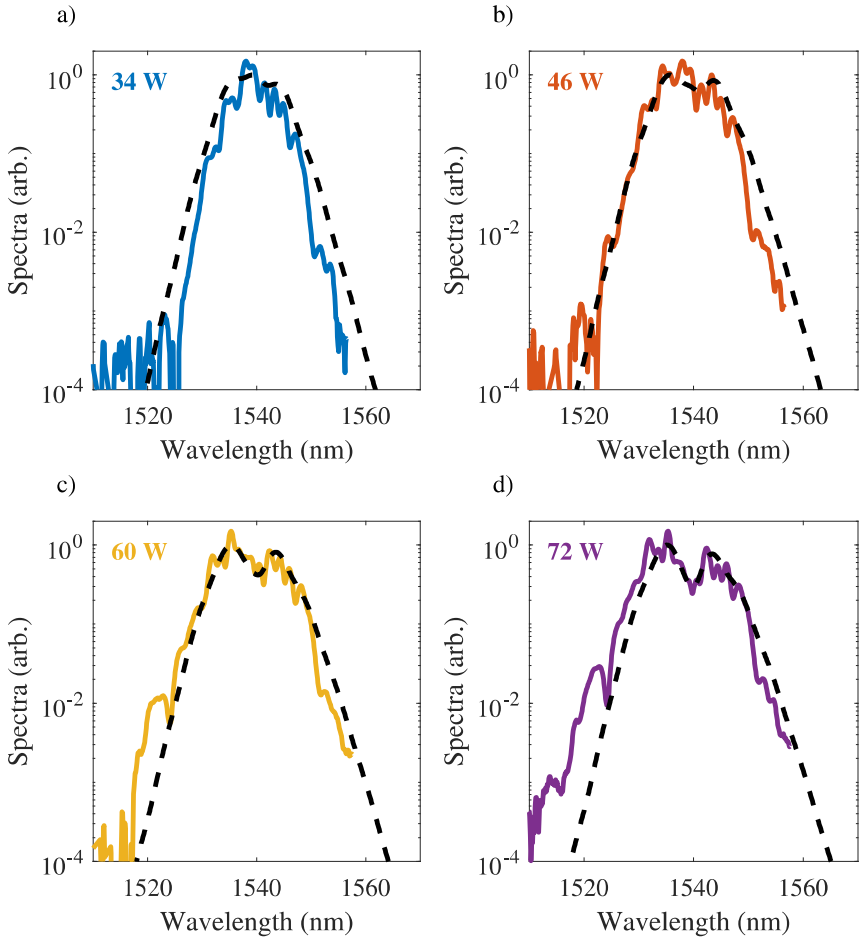


FIGURE 6.6: Simulation fit (black dashed line) to spectral broadening through waveguide 23.2.E.7 with length 1.229 cm, at peak input powers a) 34 W, b) 46 W, c) 60 W and 72 W. The additional peak around 1520 nm which occurs in c) and d) results from multimode interactions, which are not accounted for in the simulation.

## 6.5 Conclusions

The observation of low optical losses in polysilicon waveguides has made characterisation of the third order nonlinear effects TPA and SPM possible in laser crystallised polysilicon waveguides with widths of 3 µm. Such measurements are the first of their kind in polysilicon planar waveguides, marking a significant advancement in the state of the art. Values of $\beta_{\mathrm{TPA}}$ and $n_2$ have been obtained in two waveguides, with $\beta_{\mathrm{TPA}}$ between $7 \times 10^{-12}\,\mathrm{m\,W^{-1}}$ and $10 \times 10^{-12}\,\mathrm{m\,W^{-1}}$, and $n_2$ between $3.5 \times 10^{-18}\,\mathrm{m^2\,W^{-1}}$ and $4.5 \times 10^{-18}\,\mathrm{m^2\,W^{-1}}$. These ranges lie around the upper and lower extents of the recorded values for crystalline silicon waveguides, giving values of the $\mathrm{FOM_{NL}}$ of 0.29 and 0.32.

Further improvement of these values may be possible by increasing the crystalline fraction of the waveguide material to reduce the linear and nonlinear absorption at grain boundaries. As the third order susceptibility $\chi^{(3)}$ is a tensor, it is sensitive to the crystal orientation relative to the propagating wave, and so dislocations in the crystal structure and the subsequent change in orientation may also negatively impact the nonlinear propagation. Therefore, a study of this relation may demonstrate the necessity of ensuring a consistent crystal orientation along the waveguide. Preferential crystallisation such as this has been achieved in polysilicon by various methods [22], [24], [97], [98], [153], so adaptation of these may be possible. Reduction of the waveguide width to 1 µm, and losses to $1\,\mathrm{dB\,cm^{-1}}$, would be expected to enable guiding of light signals with greater intensity and lower loss, allowing the demonstration of improved nonlinear effects. This would allow the use of polysilicon waveguides in a wide range of integrated nonlinear optical applications.

To give an indication of the potential of polysilicon for nonlinear applications, simulations of the spectral broadening have been carried out with these target values for loss and waveguide dimensions. Figure 6.7a compares the simulated spectrum from Figure 6.6d to that calculated for a small-area low-loss waveguide. Keeping $n_2$ and $\beta_{\mathrm{TPA}}$ the same, but reducing linear loss to $1\,\mathrm{dB\,cm^{-1}}$ and the effective area from $0.6\,\mu\mathrm{m}^2$ to $0.2\,\mu\mathrm{m}^2$ produces a slightly broader spectrum, with evidence of enhanced phase shift from the emerging third SPM peak at the centre of the pulse. To simulate the use of such waveguides in an integrated system, the simulated coupling loss was then reduced from 14 dB to 7 dB, producing the spectrum shown in Figure 6.7b. The high coupling loss in the experimental work reported in this thesis is largely attributed to the cleaved facets, which would be avoided in an integrated system. The broad spectrum simulated here shows that with some development to reduce losses, laser-crystallised polysilicon waveguides would be suitable for a broad range of nonlinear signal processing applications.

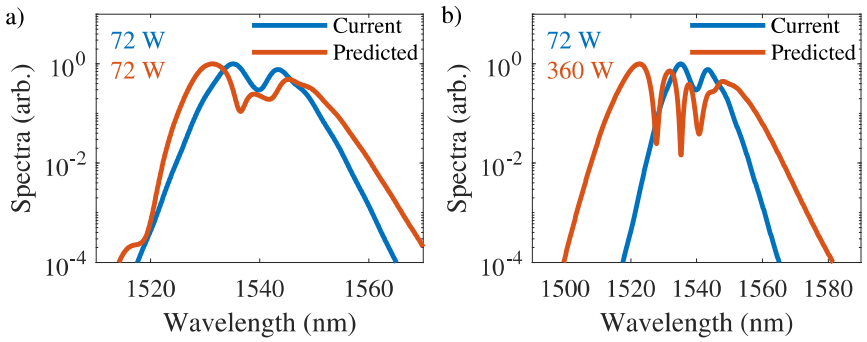


FIGURE 6.7: Comparison of simulated fit to experimental data (blue) to theoretical spectra (orange) obtained with a) $1\,\mathrm{dB\,cm^{-1}}$ loss and $0.2\,\mu\mathrm{m}^2$ effective mode area and b) enhanced coupling efficiency as might be expected in an integrated optical system. Powers shown are coupled peak powers.

# Chapter 7

# Silicon-Germanium Graded Index Waveguides

Silicon-germanium alloys have been extensively used in the fabrication of photonic components. Its composition can be tuned for applications such as photodetection and nonlinear optics, for which it offers superior capabilities in comparison to silicon. This chapter looks to extend previous investigations into SiGe for optoelectronics, by using local laser-induced compositional segregation to fine-tune the material properties.

First, the material properties and existing applications of silicon-germanium are outlined. Then the laser-writing process and material analysis of the polycrystalline written structures are described. A detailed discussion of the Raman spectroscopy data analysis is provided so that the results obtained in this manner can be compared to simulations and measurements by other methods. Raman spectroscopy is a nondestructive contact-free analysis method, so determining its accuracy compared to other methods is important for future investigations in this area. Finally, the electrical characterisation work is presented to demonstrate a practical application of the localised germanium content tuning.

## 7.1 Silicon-Germanium in Optics

Silicon photonics is a mature field, as discussed in Section 1.1, as it can make use of the favourable properties of Si such as high transmission at telecommunications wavelengths, and the existing manufacturing infrastructure available due to the use of silicon in the electronics industry. However, for some applications the properties of silicon are less ideal. Most notably, the silicon transmission window ends at $\lambda \approx 7\,\mu m$, ruling out its use for a large portion of the mid-IR spectrum, which extends from $2\,\mu m$ to $20\,\mu m$.

To access a greater proportion of the mid-IR spectral region, germanium components have been used as this material transmits to wavelengths up to $\lambda = 14\,\mu\text{m}$ [154]. Additionally, the high linear refractive index of Ge offers tighter optical confinement, and the high Kerr coefficient enables efficient nonlinear photonics [89]. Furthermore, the narrow indirect bandgap of 0.67 eV can be changed to a direct bandgap with strain engineering, offering improved suitability for light generation and lasing [155]–[157].

Silicon-germanium is a binary alloy that combines the benefits of both materials. The composition is typically denoted $Si_{1-x}Ge_x$, where $x$ is the germanium fraction, and this material has long been used in microelectronics processing as it offers advantages over conventional doped silicon thanks to the improved electronic properties which result from strain and bandgap engineering [158]. Further applications in electronics, photonics and optoelectronics have also made use of the modified bandgap, improving the detection range in photodetectors [12], reducing the energy consumption in electro-optic modulators [81], and enhancing solar cell responses [82]. Furthermore, the enhanced transmission in the mid-IR and increased nonlinear refractive index of SiGe has been used in nonlinear optics [55], [56].

However, as the alloy properties depend on the Ge content, this must be optimised for each application. For example, photodetection at $\lambda = 1550\,\text{nm}$ has been demonstrated in low-Ge materials ($x = 0.2$) [12], while solar cells manufactured with $x = 0.56$ rely on the higher Ge content to reduce the bandgap, improving absorption [82]. For on-chip nonlinear applications, graded waveguides with high-Ge regions ($0.5 < x < 1$) have been demonstrated, making use of the large nonlinear refractive index of Ge in the mid-IR [56]. For integrated chip applications, components using different Ge concentrations may be desirable, such as detectors operating in different wavelength ranges. Additionally, grating structures can be fabricated with small-scale variations in the refractive index by changing the Ge fraction. In the conventional manufacture processes such as HWCVD or low-pressure CVD (LPCVD), the composition of a deposited layer is constant across that layer, meaning that multiple deposition and lithography steps would be necessary to create an optoelectronic layer containing components with different Ge fractions, making this an expensive and time-consuming process.

## 7.2 Compositional Segregation by Laser Annealing

Compositional segregation, in which an evenly-mixed alloy is separated into regions with a high concentration of one alloy component, has been observed in SiGe under direct laser heating [159]–[163]. Weizman et al. observed that under pulsed laser annealing, lateral segregation changed the Ge fraction by up to 40% [160]. Ong et al. demonstrated the formation of a vertical graded-index SiGe waveguide during liquid-phase regrowth, indicating that heat transfer into the substrate promoted the formation of high-Si regions

[161]. Finally, CW laser processing has been used for the creation of microstructures in both fiber and on-chip geometries, demonstrated by Coucheron et al. and Runge et al. respectively [162], [163]. These structural changes are shown in Figure 7.1. Careful velocity control enabled the manufacture of Ge-rich grating structures (Figure 7.1a), and long exposure with a stationary beam was used to demonstrate the creation of micron-scale structures with high Ge content (Figure 7.1b). However, the dynamics, capabilities and controllability of the CW annealing process have not been comprehensively explored.

The change in local composition that results from laser scanning speed, as noted by Coucheron et al., leads naturally to the question of whether using different but constant scan speeds during laser annealing of planar SiGe films will influence the resulting distribution.

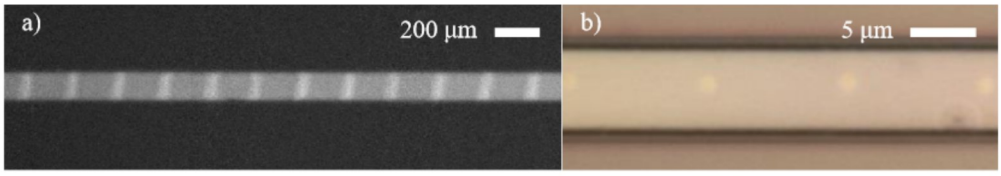


FIGURE 7.1: Laser-written periodic structures in a) SiGe-core fiber by periodic blocking of the incident laser beam [162], and b) planar SiGe structures written by 10 s stationary-beam exposure [163].

### 7.2.1 Fabrication

To investigate the applications of this, a 400 nm amorphous $Si_{0.4}Ge_{0.6}$ film was deposited by plasma-enhanced CVD (PECVD), as shown in Figure 7.2a. To ensure the compatibility of the system under study with conventional microelectronics, crystalline silicon was chosen as a substrate material. The silicon wafer was stripped of the native oxide by a 3 minute etch in 7:1 buffered HF. After cleaning, the substrate was placed in a PECVD chamber and pre-heated to the deposition temperature to ensure an even deposition rate. Film deposition was carried out with the parameters listed in Table 7.1. The precursor gases were silane ($SiH_4$) and germane ($GeH_4$).

| | |
|---|---|
| $SiH_4$ Flow | 5 sccm |
| $GeH_4$ Flow | 50 sccm |
| Chamber pressure | 300 mTorr |
| RF power | 15 mW |
| Temperature | 200 °C |

TABLE 7.1: Pressure-enhanced CVD conditions for amorphous $Si_{0.4}Ge_{0.6}$ deposition.

To induce a post-deposition compositional segregation in the SiGe film, a molten zone must be created to allow the redistribution of constituent atoms. In this study, a 488 nm laser was used to provide the energy to induce melting. The wavelength was chosen to

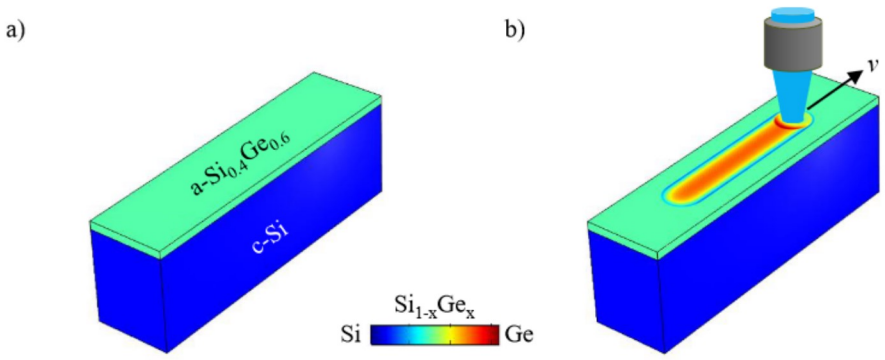


FIGURE 7.2: Fabrication of compositionally-graded stripes by direct laser writing. a) Amorphous $Si_{0.4}Ge_{0.6}$ is deposited by PECVD on a c-Si substrate, with a film thickness of 400 nm. b) Direct laser heating induces compositional segregation in the molten zone. The molten zone is moved across the sample at a speed $v$.

avoid the transfer of heat to the c-Si substrate. In pure Si, the penetration depth of 488 nm light is 485 nm and in pure Ge is 16 nm. Therefore, the starting Ge concentration will minimise direct heat transfer to the substrate.

The molten zone at the laser focus was scanned along the material surface, by moving the high-precision x/y stages according to a G-code control program as shown in Figure 7.2b. On cooling, nucleation sites form and trigger crystal growth. In planar films under continuous-wave laser annealing, these typically originate at the boundaries of the heated volume, as discussed in Section 2.2.2.2. The resulting polycrystalline SiGe has superior optical and electrical properties compared to the original amorphous material.

Polycrystalline stripes of length 1 cm were written in the amorphous film using the crystallisation setup described in Section 3.1.3, with the 488 nm $Ar^+$ laser as the heat source for melting. Initially, a 10x objective (0.25 NA), giving a focused spot diameter of 7 µm, was used to write stripes with scanning speeds of $1\,mm\,s^{-1}$ & $10\,mm\,s^{-1}$. Microscope investigation showed clear compositional differences, visible due to the colour difference between Si-rich and Ge-rich material. For a more comprehensive study, a 20x (0.4 NA) objective was used to give a spot diameter of 3 µm at focus, with which stripes were written at speeds of 0.1, 1, 5, 10, 15, 20, 25, 50 & $100\,mm\,s^{-1}$, with incident power 250 mW. High power is desired to melt the full depth of the SiGe film, however higher intensities resulted in ablation.

### 7.2.2 Material Investigations

Preliminary analysis of the composition of each stripe was carried out by optical microscopy. The natural colour of Si-rich material has a blue hue, while Ge-rich areas are more yellow-coloured. The optical microscope image shown in Figure 7.3a reveals a change from a Si-rich core at low scanning speeds to a Ge-rich core at high speeds. Additionally, at the lowest and highest speeds, a border can be seen, showing Ge-rich

material at the boundary of the 0.1 mm s$^{-1}$ stripe, and Si-rich material at the boundary of the 100 mm s$^{-1}$ stripe.

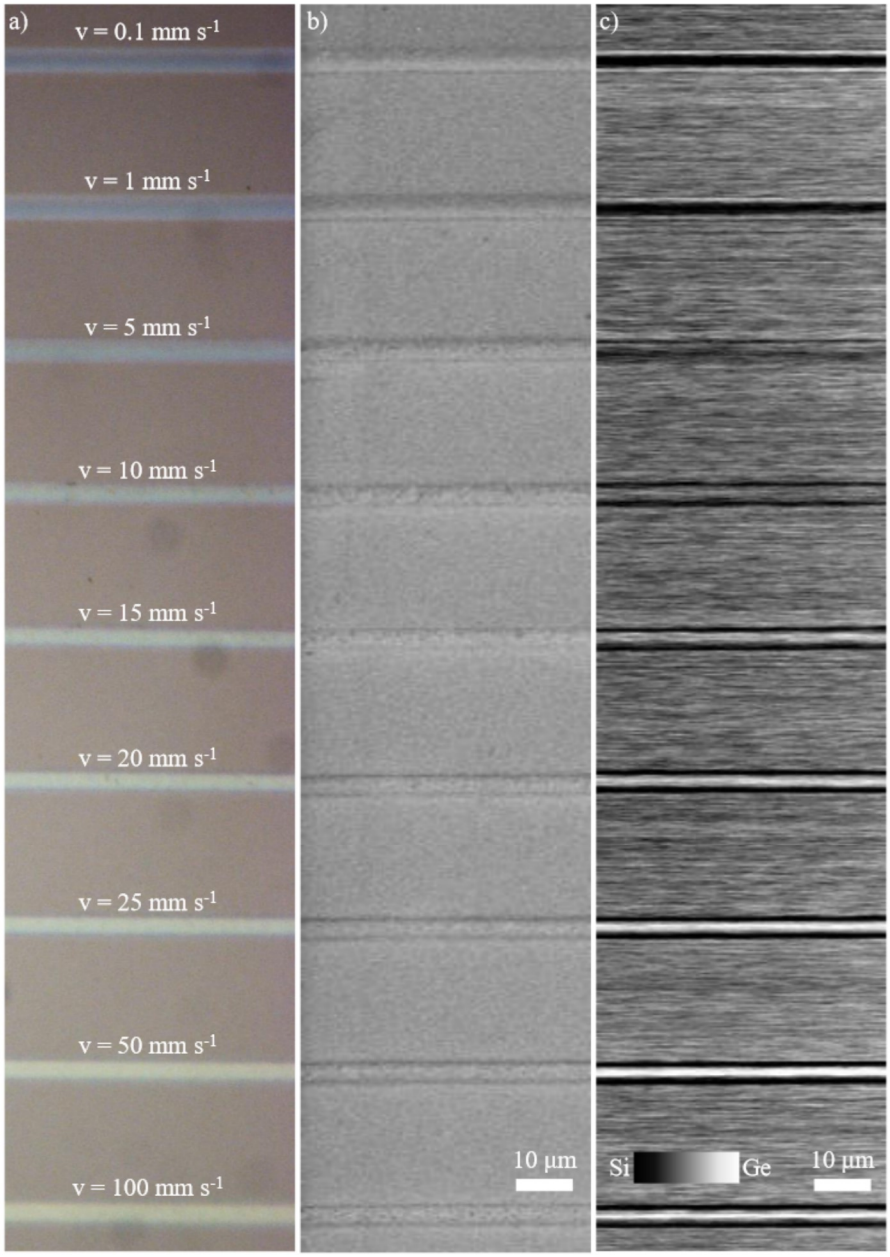


FIGURE 7.3: Laser-annealed $Si_{1-x}Ge_x$ lines written at a range of scanning speeds, imaged under a) optical microscopy, b) scanning electron microscopy and c) back-scattered electron diffraction microscopy. The Ge concentration is dependent on the laser scanning speed, with high speeds inducing higher concentration at the stripe centre.

Further investigation was carried out by scanning electron microscopy and back-scattered electron diffraction (BSED) microscopy. SEM provides topographical information about

the material surface after crystallisation, and shows minor differences based on laser scanning speed. Figure 7.3b shows an SEM image that corresponds to the optical microscope images discussed above. At low speeds ($v \leq 1\,\mathrm{mm\,s^{-1}}$), a smooth surface with an overall curve is seen. At 5, 10 & $15\,\mathrm{mm\,s^{-1}}$ some roughness is visible, suggestive of unstable crystallisation dynamics in this speed range. Finally, at speeds $\geq 20\,\mathrm{mm\,s^{-1}}$ a second shape emerges, visible due to the 'shadowed' edges of the stripe. A full investigation of the surface morphology and crystallisation dynamics is outside of the scope of this work, but may provide valuable insights if undertaken.

Figure 7.3c shows BSED micrographs of laser-written stripes, with dark regions indicating a higher Si content and light regions indicating high-Ge concentration. The spatial resolution of this technique is lower than that of optical or scanning electron microscopy, as at the electron acceleration voltage used here (15 kV) the interaction volume is greater than 1 µm, leading to underestimation of the Ge content due to the inclusion of signal from the c-Si substrate. Despite this, the measurements confirm the observations of optical microscope study. Low-speed annealing induces a Si-rich core with Ge-rich boundaries, while the reverse is true of high-speed annealing. At $5\,\mathrm{mm\,s^{-1}}$ the resulting concentration is approximately uniform and similar to that of the surrounding amorphous material, while compositional segregation occurs at higher and lower speeds.

To illustrate this phase segregation in more detail, a theoretical model was created by Dr Ozan Aktas, and used to carry out finite-element phase-field simulations using COMSOL Multiphysics. The results of these simulations for scanning speeds of 0.1, 10 & $100\,\mathrm{mm\,s^{-1}}$ are shown in Figure 7.4. At low speeds, germanium concentrates in the molten zone. At the trailing edge, SiGe solidifies in approximately equal composition to the surrounding amorphous material. Undercooling from the highly thermally conductive Si substrate leads to an increased silicon fraction at the lower edge of the polycrystalline volume while the Ge concentration at the surface is slightly higher, supporting previous observations by Ong et al. [161]. Although this is more noticeable for simulations of high-speed annealing, a minor reduction in Ge content at the underside is still visible in the simulation for $v = 0.1\,\mathrm{mm\,s^{-1}}$.

At higher scanning speeds, the high Ge concentration across the molten zone cannot be maintained, as the transport speed of molten Ge is limited by its diffusion speed. The Ge concentration is therefore higher at the trailing edge of the molten zone, increasing the proportion of Ge that is deposited during solidification. This leads to high Ge content in the middle and top of the stripe, and lower concentration in the remaining volume.

## 7.3 Analysis by Raman Spectroscopy

Raman spectroscopy is commonly used to examine the composition of silicon-germanium alloys [162], [165]–[167], as it provides a rapid, non-contact and nondestructive means for

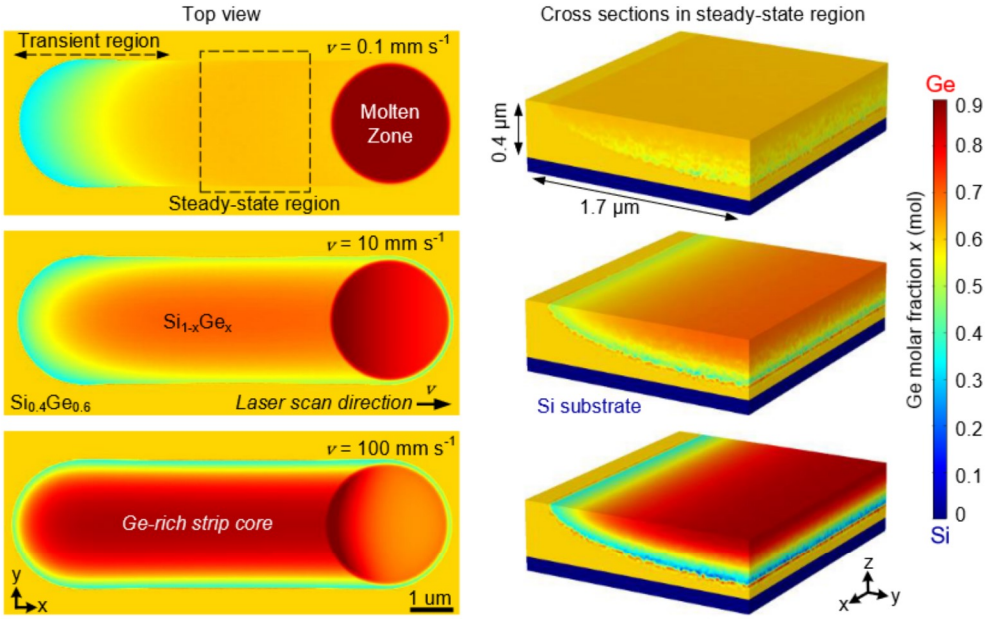


FIGURE 7.4: Finite-element phase-field numerical simulations show the influence of scanning speed on Ge fraction. Left: Top view showing the material composition at the surface. A transient acceleration period is followed by a steady-state region, and the molten zone in which the phase segregation occurs. Right: Cross-section of the steady-state region at each speed, showing the Si and Ge distribution. Reproduced with permission from [164].

determining both atomic percentage and material strain ($\varepsilon_{\parallel}$) in a single measurement. An example of the crystalline SiGe spectrum taken from a reference sample used in this work with Ge content $x = 0.62$, is shown in Figure 7.5. Table 7.2 lists reference peak positions for bonds in crystalline semiconductors, assuming pure material in the case of the Ge-Ge and Si-Si bonds, and $x = 0.5$ in the case of the Si-Ge bond. As discussed in the following section, the exact peak positions in the Raman spectrum of a $Si_{1-x}Ge_x$ sample are dependent on both the material composition and strain.

| Bond | Peak Position ($cm^{-1}$) |
|---|---|
| Ge-Ge | 280 |
| Si-Ge | 411 |
| Si-Si | 520 |

TABLE 7.2: Unstrained Raman peak positions for bonds present in a SiGe alloy.

This section will discuss the method by which the Ge content and material strain were calculated from Raman spectroscopy. A description of the data collection process and the obtained results will also be provided.

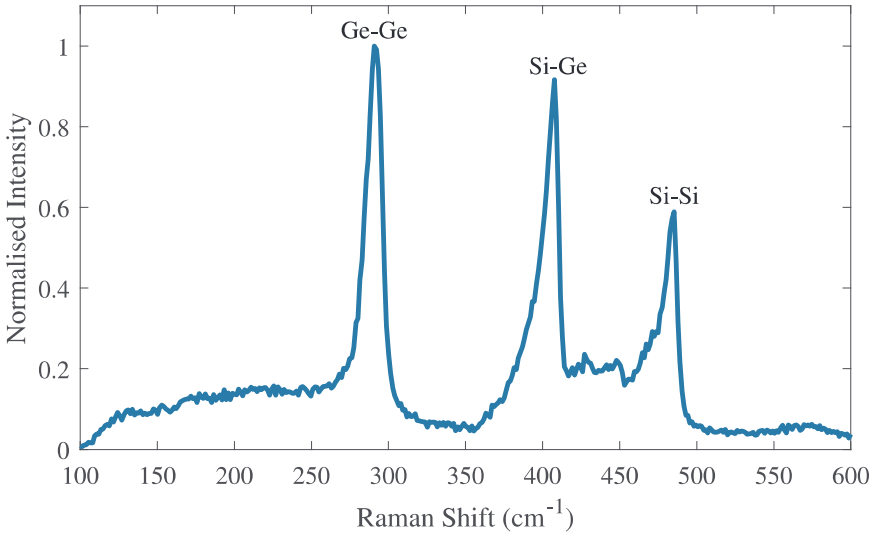


FIGURE 7.5: Raman response of strained crystalline SiGe, showing three peaks corresponding to Ge-Ge, Si-Ge and Si-Si bonds respectively.

### 7.3.1 Analysis of Raman Spectra

The experimental peak positions $\omega^{X-Y}$, where $X$ and $Y$ are either Si or Ge, can be used to calculate the Ge content $x$ and in-plane material strain $\varepsilon_{\parallel}$ by comparing each peak with the unstrained reference position $\omega_0^{X-Y}$ listed in Table 7.2. The experimental peak positions can be expressed as

$$\omega^{\text{Si-Si}} = \omega_0^{\text{Si-Si}} + A^{\text{Si-Si}}x + B^{\text{Si-Si}}\varepsilon_{\parallel} \tag{7.1a}$$

$$\omega^{\text{Si-Ge}} = \omega_0^{\text{Si-Ge}} + A^{\text{Si-Ge}}x + B^{\text{Si-Ge}}\varepsilon_{\parallel} \tag{7.1b}$$

$$\omega^{\text{Ge-Ge}} = \omega_0^{\text{Ge-Ge}} + A^{\text{Ge-Ge}}x + B^{\text{Ge-Ge}}\varepsilon_{\parallel}, \tag{7.1c}$$

where $A^{X-Y}$ connects the change in peak position with the Ge content, and $B^{X-Y}$ provides the relation between peak position and strain. To obtain values for $A^{X-Y}$ and $B^{X-Y}$, a calculated position for the Si-Ge peak is found in terms of the experimentally determined Si-Si and Ge-Ge peak positions. The process for this is described here.

First, Equation 7.1a and Equation 7.1c are rearranged to give expressions for $\varepsilon_{\parallel}$

$$\varepsilon_{\parallel} = \frac{\left(\omega^{\text{Si-Si}} - \omega_0^{\text{Si-Si}}\right) - A^{\text{Si-Si}}x}{B^{\text{Si-Si}}} \tag{7.2a}$$

$$\varepsilon_{\parallel} = \frac{\left(\omega^{\text{Ge-Ge}} - \omega_0^{\text{Ge-Ge}}\right) - A^{\text{Ge-Ge}}x}{B^{\text{Ge-Ge}}}. \tag{7.2b}$$

Equating these expressions to give

$$\frac{\left(\omega^{\text{Si-Si}} - \omega_0^{\text{Si-Si}}\right) - A^{\text{Si-Si}}x}{B^{\text{Si-Si}}} = \frac{\left(\omega^{\text{Ge-Ge}} - \omega_0^{\text{Ge-Ge}}\right) - A^{\text{Ge-Ge}}x}{B^{\text{Ge-Ge}}} \tag{7.3}$$

eliminates $\varepsilon_{\parallel}$, and this can be rearranged to give a term for $x$ that is independent of $\varepsilon_{\parallel}$:

$$x = \frac{B^{\text{Ge-Ge}}\left(\omega^{\text{Si-Si}} - \omega_0^{\text{Si-Si}}\right) - B^{\text{Si-Si}}\left(\omega^{\text{Ge-Ge}} - \omega_0^{\text{Ge-Ge}}\right)}{A^{\text{Si-Si}}B^{\text{Ge-Ge}} - A^{\text{Ge-Ge}}B^{\text{Si-Si}}} \tag{7.4}$$

A similar process can be followed to obtain an expression for $\varepsilon_{\parallel}$ independent of $x$:

$$\varepsilon_{\parallel} = \frac{A^{\text{Si-Si}}\left(\omega^{\text{Ge-Ge}} - \omega_0^{\text{Ge-Ge}}\right) - A^{\text{Ge-Ge}}\left(\omega^{\text{Si-Si}} - \omega_0^{\text{Si-Si}}\right)}{A^{\text{Si-Si}}B^{\text{Ge-Ge}} - A^{\text{Ge-Ge}}B^{\text{Si-Si}}} \tag{7.5}$$

These can then both be substituted into Equation 7.1b, giving an expression for a calculated value of the Si-Ge peak position independent of both $x$ and $\varepsilon_{\parallel}$.

$$\begin{aligned}\omega_{\text{calc}}^{\text{Si-Ge}} = \omega_0^{\text{Si-Ge}} + \frac{\left(A^{\text{Si-Ge}}B^{\text{Ge-Ge}} - A^{\text{Ge-Ge}}B^{\text{Si-Ge}}\right)\left(\omega^{\text{Si-Si}} - \omega_0^{\text{Si-Si}}\right)}{A^{\text{Si-Si}}B^{\text{Ge-Ge}} - A^{\text{Ge-Ge}}B^{\text{Si-Si}}} + \\ \frac{\left(A^{\text{Si-Si}}B^{\text{Si-Ge}} - A^{\text{Si-Ge}}B^{\text{Si-Si}}\right)\left(\omega^{\text{Ge-Ge}} - \omega_0^{\text{Ge-Ge}}\right)}{A^{\text{Si-Si}}B^{\text{Ge-Ge}} - A^{\text{Ge-Ge}}B^{\text{Si-Si}}}.\end{aligned} \tag{7.6}$$

Using Raman measurements on a SiGe sample of known composition ($x = 0.62$) from which $\omega^{\text{Si-Si}}$ and $\omega^{\text{Ge-Ge}}$ can be determined, the coefficients $A^{X-Y}$ and $B^{X-Y}$ were calculated by minimisation of the total squared error between $\omega_{\text{calc}}^{\text{Si-Ge}}$ and $\omega^{\text{Si-Ge}}$. These calculations gave the values

$$\begin{aligned} A^{\text{Si-Si}} &= -75 \quad A^{\text{Si-Ge}} = -13 \quad A^{\text{Ge-Ge}} = 19 \\ B^{\text{Si-Si}} &= -870 \quad B^{\text{Si-Ge}} = -550 \quad B^{\text{Ge-Ge}} = -510 \end{aligned} \tag{7.7}$$

Rewriting Equation 7.1 in matrix form, where $\mathbf{\Delta\Omega}$ is the matrix of the differences between measured and unstrained peak positions,

$$\mathbf{\Delta\Omega} = \begin{pmatrix} \omega^{\text{Si-Si}} - \omega_0^{\text{Si-Si}} \\ \omega^{\text{Si-Ge}} - \omega_0^{\text{Si-Ge}} \\ \omega^{\text{Ge-Ge}} - \omega_0^{\text{Ge-Ge}} \end{pmatrix} = \begin{pmatrix} A^{\text{Si-Si}} & B^{\text{Si-Si}} \\ A^{\text{Si-Ge}} & B^{\text{Si-Ge}} \\ A^{\text{Ge-Ge}} & B^{\text{Ge-Ge}} \end{pmatrix} \begin{pmatrix} x \\ \varepsilon_{\parallel} \end{pmatrix} = \mathbf{MX}, \tag{7.8}$$

where $\mathbf{M}$ is the matrix of coefficients and $\mathbf{X}$ is the vector for composition and strain. $\mathbf{X}$ can be calculated for any measured $Si_{1-x}Ge_x$ spectrum by applying inverse and transpose operators to $\mathbf{M}$, giving

$$\mathbf{X} = \left(\mathbf{M}^{\mathrm{T}}\mathbf{M}\right)^{-1}\mathbf{M}^{\mathrm{T}}\boldsymbol{\Delta\Omega}. \tag{7.9}$$

### 7.3.2 Results and Discussion

To measure the change in material composition across a laser-written stripe, a series of Raman spectra were captured using a Renishaw Invia system. The spectra were taken along an axis perpendicular to the direction of laser writing, at intervals of 0.5 µm. The illumination laser wavelength, $\lambda = 532\,\mathrm{nm}$, was selected to ensure that the penetration depth was low enough to avoid inducing a Raman response from the Si substrate. The laser was focused to a spot diameter of 1 µm, limiting the accuracy of these investigations due to the averaging of the signal across the larger volume. However, as the spot is still smaller than the width of the written stripes, these measurements are still able to indicate the change in composition. Examples of the resulting spectra from low-speed and high-speed writing are shown in Figure 7.6.

Initial study of these indicates that low-speed writing results in a silicon-rich core in the annealed region while high-speed writing induces a germanium-rich core volume with silicon-rich fringes at the extent of the crystallised area. High silicon content is shown by the proportionally high intensity of the Si-Si peak at a Raman peak shift of approximately $500\,\mathrm{cm}^{-1}$ and the strong overall intensity of the spectrum, as silicon has a lower reflectance than germanium and therefore a greater fraction of the incident beam is subjected to Raman scattering. The germanium-rich volume conversely shows a lower intensity, due to the higher reflectance of Ge at the Raman laser wavelength, and a weak Si-Si response.

Example spectra from individual points across the $25\,\mathrm{mm\,s}^{-1}$ stripe which highlight the features discussed above are shown in Figure 7.7. The amorphous region outside the stripe exhibits no crystalline Raman peaks, while a strong response is seen for the Ge-Ge, Si-Ge and Si-Si peaks in the stripe boundary. The similar intensity of each of the three peaks suggests an approximately equal proportion of Si and Ge. In the stripe core, the reduced overall intensity is indicative of a higher Ge content, as is the dominance of the Ge-Ge bond response and negligible Si-Si peak.

A MATLAB script was written to calculate $x$ and $\varepsilon_{\parallel}$ for each point in the line scans. First, a Voigt fit is applied to each peak, determining the peak position and relative intensity. Examples of these fits are shown in Figure 7.8 for scans taken at points with high ($x = 0.72$) and low ($x = 0.52$) Ge. The peak positions show clear deviations from the unstrained values of $\omega^{\text{Ge-Ge}} = 280\,\mathrm{cm}^{-1}$, $\omega^{\text{Si-Ge}} = 411\,\mathrm{cm}^{-1}$ and $\omega^{\text{Si-Si}} = 520\,\mathrm{cm}^{-1}$, with the high-Ge spectrum having a greater change. These deviations are a result of strain on the atomic bonds due to the mismatch between the lattice constants $a$ of crystalline silicon and germanium ($\Delta a = 0.277 \times 10^{-10}\,\mathrm{m}$). To precisely determine the

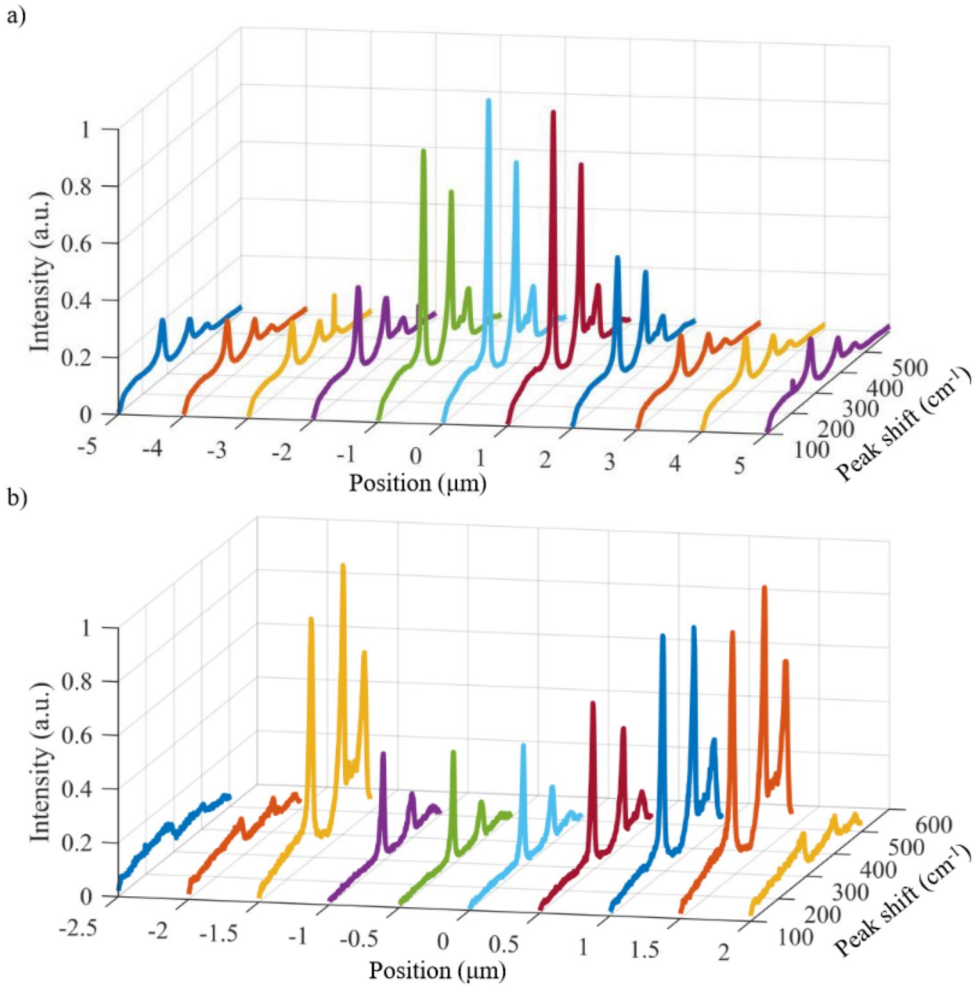


FIGURE 7.6: Cross-section Raman maps on laser stripes annealed at a) $0.8\,\mathrm{mm\,s^{-1}}$ and b) $25\,\mathrm{mm\,s^{-1}}$. The higher Ge content in the centre of the high-speed annealed strip is seen by the low overall intensity and the weak Si-Si bond signal.

average value of $x$ in the volume from which the spectrum was taken, the MATLAB script then applies the calculation process outlined in Section 7.3.1.

Figure 7.9 shows the variation in $x$ across polycrystalline stripes written with scanning speeds of $25\,\mathrm{mm\,s^{-1}}$ and $0.1\,\mathrm{mm\,s^{-1}}$. As observed from optical and BSED microscopy, and predicted by simulations, the high laser scanning speed produces a high Ge content in the core and low Ge content at the outer limits, while low scanning speeds do not raise the Ge content and show a significantly lower contrast in content between the stripe core and edges. This provides further verification that the content can be tuned based on the laser scanning speed, opening opportunities for the microscale tailoring of Ge content for specific applications in a post-deposition process. Potential uses for this technique are not limited to stripes as demonstrated in this work, but could also be used to create patterns such as diffraction gratings.

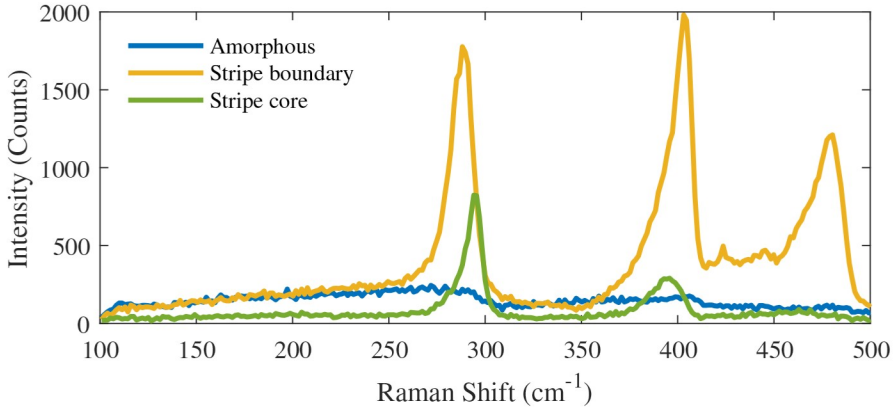


FIGURE 7.7: Overlaid Raman spectra from the 25 mm s$^{-1}$ Raman map, comparing regions of amorphous material, the high-Si boundary at the stripe edge, and the high-Ge core region. The higher reflectance of Ge reduces the total intensity of the Raman response, and the a-SiGe region shows no crystalline peaks. Line colours correspond to matching spectra in Figure 7.6b.

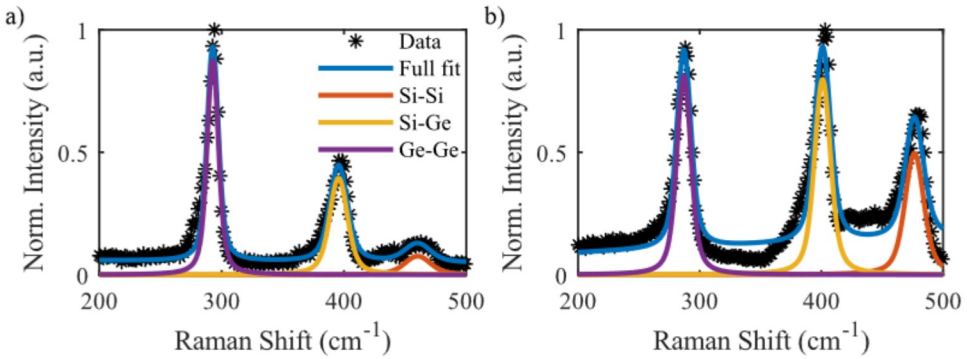


FIGURE 7.8: Fitted single-point Raman spectra for a) high-Ge ($x = 0.72$) and b) low-Ge ($x = 0.52$) following laser crystallisation of an amorphous $Si_{0.4}Ge_{0.6}$ film. Increased Ge content results in higher strain, causing an increased shift in peak position.

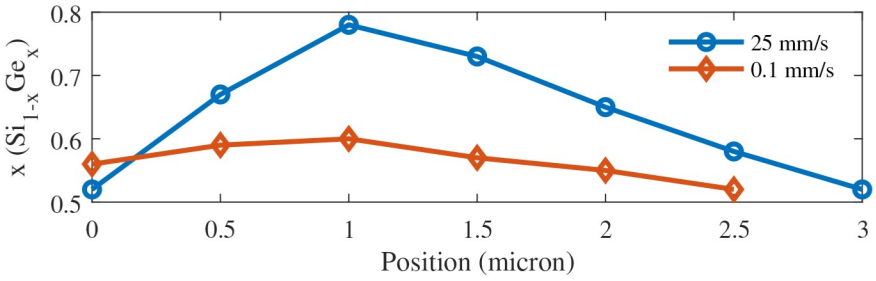


FIGURE 7.9: Ge content across stripes crystallised at high and low speeds in a-$Si_{0.4}Ge_{0.6}$. High speeds result in a significantly increased Ge content at the core, and reduced Ge content at the boundaries.

## 7.4 Optoelectronic Characterisation of SiGe Stripes

The remainder of the work outlined in this chapter was carried out by Dr Ozan Aktas, and is provided to contextualise the Raman analysis results presented in Section 7.3. The demonstration of photodetection in laser-written SiGe stripes proves the capacity of the laser-writing process for bandgap engineering.

To study the photodetective capabilities of the laser-written polySiGe stripes, they were connected to a circuit and the current-voltage (I-V) characteristics were measured with and without incident light onto the upper surface. Figure 7.10a shows the schematic arrangement of the experimental setup, and Figure 7.10b shows a photograph of the same. The sample and two stainless steel contacts were placed on high-precision x/y/z stages, and a top-down microscope system was used for imaging to ensure accurate placement of the contact points. The probes were brought into contact with the stripe with a separation of 300 µm, and the objective used in the imaging was then used to illuminate the top surface of the stripe with 800 nm wavelength pulsed laser light from a tunable source, with an average incident power of 4 µW. Figure 7.11 shows the I-V curves for stripes written at 0.1 mm s$^{-1}$ and 25 mm s$^{-1}$, with and without illumination, and the curve for the amorphous material is provided as a reference for the material characteristics before laser annealing. The crystallisation process clearly enhances the photocurrent of SiGe by approximately four orders of magnitude, with greater conductivity enhancement seen in stripes annealed at higher speeds. The average responsivity of 48 mA W$^{-1}$ is close to that reported in unpassivated SiGe photodetectors fabricated by conventional processes [12].

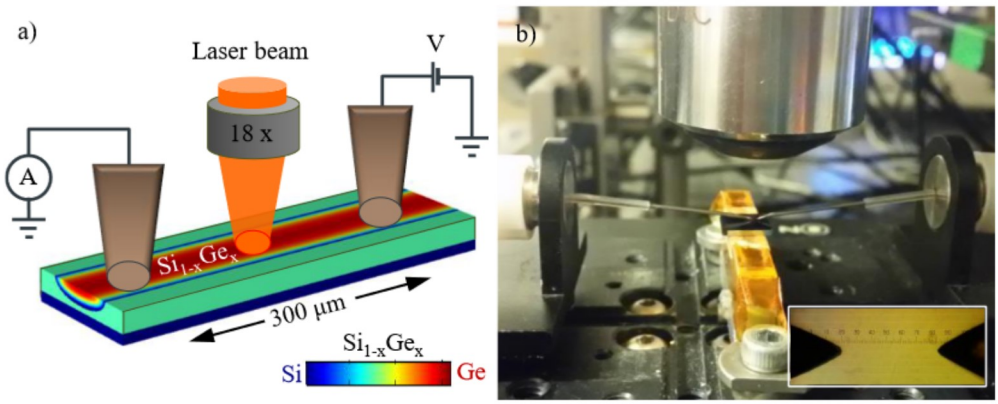


FIGURE 7.10: Experimental setup for photodetection measurements, in a) schematic view and b) photograph of the arrangement with sample and steel contacts in high-precision stages. Inset: Image captured through microscope objective used during measurements for focusing incident light.

To investigate the bandgap engineering capabilities of the laser processing technique, the influence of the illuminating wavelength on the photocurrent was measured to record any changes to the bandgap, indicated by changes to the wavelength at which there

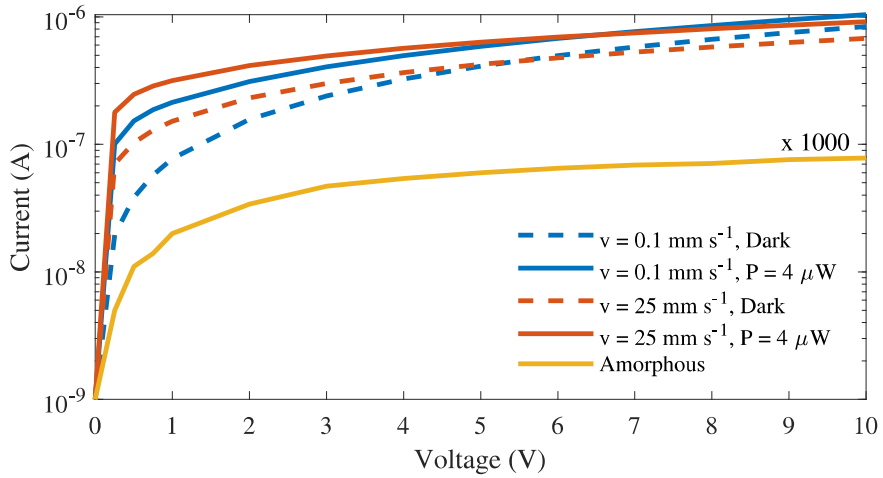


FIGURE 7.11: The current (I)-voltage (V) curves for crystallised SiGe stripes written at 0.1 mm s$^{-1}$ and 25 mm s$^{-1}$, in dark conditions and with illumination by an 800 nm laser source. The amorphous IV curve has been enhanced by 1000 times for comparison purposes.

is no longer a detectable photocurrent. At this wavelength, the incident photons lack the energy to excite free carriers across the bandgap. For this, the incident laser power was reduced to 2.5 mW and the photocurrent $I_{photo} = I_{light} - I_{dark}$ was recorded for stripes written at 0.1, 1, 10 & 100 mm s$^{-1}$ as the illuminating wavelength was swept from 980-1540 nm in 20 nm steps. The normalised photocurrents are compared to that of pure c-Si in Figure 7.12, showing that as the laser writing speed increases, the onset of a measurable photocurrent occurs at higher wavelengths. At low wavelengths, the influence of the c-Si substrate is seen up to $\sim$ 1150 nm, as the penetration depth of the illuminating wavelengths are sufficient to pass through the 400 nm SiGe film. Beyond this point, the photon energy does not excite carriers across the Si bandgap. By comparison with the indirect bandgap for unstrained $Si_{0.4}Ge_{0.6}$, which corresponds to a wavelength of 1280 nm, it can be seen that the laser-induced phase segregation increases the photodetection range of the SiGe alloy by over 200 nm. Additionally, in low-speed stripes where the Ge composition deviates little from $x = 0.6$, the photodetection range is also increased by $\sim$ 50 nm due to the decrease in bandgap resulting from the tensile strain that arises during laser annealing.

Comparison to photodetection work in $Si_{1-x}Ge_x$ nanowires and $Ge_{1-x}Sn_x$ heterostructures indicates superior responsivity in both systems, with the former exhibiting a two order of magnitude variation in photocurrent depending on the Ge fraction [168], and the latter showing photodetection to wavelengths of up to 2.2 µm [169]. However, in these examples the composition tuning was achieved during deposition, meaning that this new method shows far greater flexibility in its application, and significantly reduces the complexity and cost of fabrication steps.

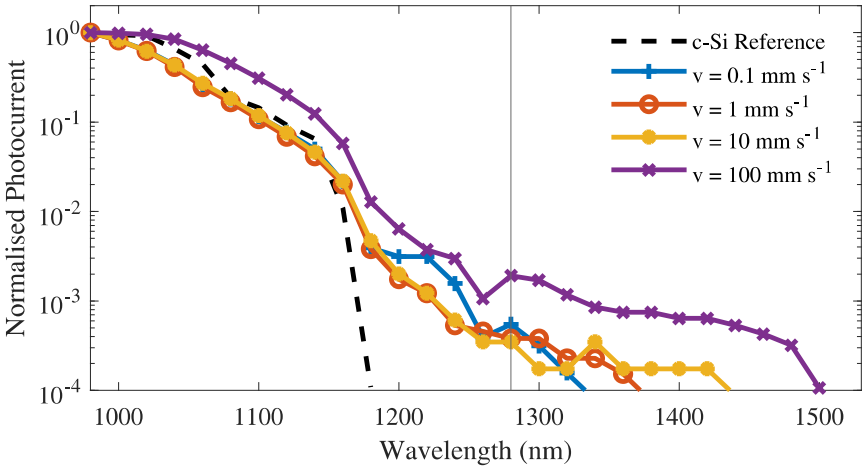


FIGURE 7.12: The spectral response of the photocurrent varies with the illuminating wavelength and the writing speed. High writing speeds extend the detection wavelength range by more than lower writing speeds due to the increased Ge concentration. The vertical line at 1280 nm indicates the bandgap of unstrained $Si_{0.4}Ge_{0.6}$.

## 7.5 Conclusions

The demonstration of post-deposition controllable compositional segregation in a binary SiGe alloy by constant-velocity continuous-wave laser annealing has been achieved, with local Ge content ranging from $0 < x < 1$. Measurement of the composition has been carried out by Raman spectroscopy and confirmed by optical microscopy, back-scattered electron diffraction microscopy and finite-element phase-field simulations. The characterisation of the photoconductor-based detection range of these laser-written microstructures has been undertaken, demonstrating bandgap engineering to tune the absorption edge by over 200 nm. Combining this work with other studies into the engineering of SiGe opens the door for advanced on-chip post-deposition fabrication of advanced photonic circuits comprising of waveguides, gratings and bandgap-sensitive components such as photodetectors. The optical and electronic characteristics of the laser-crystallised material are, however, currently limited by the polycrystalline nature of the material. Amorphous grain boundaries degrade optical and electronic performance due to scattering and absorption, but an extensive body of work exists in the electronics industry, focused on the maximisation of grain sizes obtained through continuous-wave laser annealing of amorphous films. The application of such techniques may provide the capacity to fabricate large-crystal or even monocrystalline SiGe integrated photonic components. In addition, the behaviour of SiGe during laser treatment is similar to that of many binary and ternary alloys and other multi-component systems due to the similarity in their phase diagrams, indicating that the methods applied here may be more broadly applicable.

# Chapter 8

# Conclusions and Future Work

## 8.1 Conclusions

This PhD project has focused on the application of localised laser crystallisation to fabricate low cost and flexible semiconductor-based optoelectronic systems. Waveguides have been fabricated in hydrogenated amorphous silicon using a novel etchless laser writing process, record low losses have been obtained in laser-crystallised polysilicon waveguides that has allowed for the first nonlinear characterisation in this material, and controllable compositional segregation of silicon-germanium alloys has been demonstrated.

Using localised continuous-wave laser crystallisation, waveguides were created by writing a low-index polysilicon cladding into a high-index planar a-Si:H film. Transmission measurements demonstrated losses of $(4.46 \pm 0.84)\,\mathrm{dB\,cm^{-1}}$ at $\lambda = 1550\,\mathrm{nm}$, which when compared to $(4.31 \pm 0.76)\,\mathrm{dB\,cm^{-1}}$ in a lithographically-defined reference sample indicates the viability of the method for broader applications, albeit with further development of the process to reduce losses further. The high versatility of the laser writing system was demonstrated by the fabrication of S-bend and Y-junction structures. No transmission was observed through these more complex structures, which was attributed to scattering and absorption in the region between the polysilicon cladding and hydrogenated amorphous core. Raman spectroscopic analysis along a cross-section indicated a zone at this boundary that had remained largely amorphous while having also been dehydrogenated. This results from the lateral diffusion of heat during laser crystallisation. The reduction of these losses would enable investigations into this technique for optical interconnections [170], signal processing with nonlinear optics [51]–[53], or devices such as interferometers [69]. This novel approach for lithography-free manufacture of waveguides in a-Si:H serves to avoid the inherent introduction of surface and sidewall roughness from etching, and may provide a flexible and adaptable approach to photonic system fabrication.

In pursuit of CMOS-compatible low-loss polysilicon, amorphous silicon deposited at 230 °C by HWCVD was etched to form wire structures, which were then crystallised by localised laser annealing to form polysilicon. The etching acted to thermally isolate the material, improving the crystallisation quality. Raman spectroscopy was used to investigate the material quality, showing the lowest FWHM of $2.72\,\mathrm{cm}^{-1}$, compared to the crystalline reference value of $2.7\,\mathrm{cm}^{-1}$. Over a length of 140 µm, the average deviation from the mean in the FWHM was calculated to be 4.1%, indicating a highly consistent material quality. This conclusion is supported by X-ray diffraction crystallography measurements, which show crystal grain lengths of up to 1.6 mm. Transmission measurements showed linear losses under $5\,\mathrm{dB\,cm}^{-1}$ in six waveguides, with the lowest loss being $(2.41 \pm 0.63)\,\mathrm{dB\,cm}^{-1}$, the lowest reported in polysilicon waveguides to date. This waveguide, and another waveguide with loss of $(3.98 \pm 0.73)\,\mathrm{dB\,cm}^{-1}$, were selected for characterisation of the third-order nonlinear processes two-photon absorption and self-phase modulation. The TPA coefficient and nonlinear Kerr coefficient were calculated from these, with values of $\beta_{\mathrm{TPA}}$ between $7 \times 10^{-12}\,\mathrm{m\,W}^{-1}$ and $10 \times 10^{-12}\,\mathrm{m\,W}^{-1}$, and $n_2$ in the range of $3.5 \times 10^{-18}\,\mathrm{m}^2\,\mathrm{W}^{-1}$ to $4.5 \times 10^{-18}\,\mathrm{m}^2\,\mathrm{W}^{-1}$. These are, respectively, at the higher and lower ends of the values reported in single crystal silicon, suggesting that with improvements to the material quality, polysilicon fabricated by the annealing of deposited amorphous silicon may enable low-cost CMOS-integrated multilayer silicon photonics.

Finally, the application of this laser annealing process to planar amorphous $Si_{0.4}Ge_{0.6}$ films was used to demonstrate compositional segregation dependent on the translation velocity of the laser spot. The composition was simulated using a finite-element phase-field method, and the simulation was shown to match experimental observations from Raman spectroscopy and back-scattered electron diffraction microscopy. The altered concentrations of silicon and germanium in the crystalline stripes cause modifications to the bandgap, demonstrated by photodetection and spectral response measurements. An increase in photocurrent of $\sim 4$ orders of magnitude was seen between amorphous and polycrystalline material, with higher laser scanning speeds resulting in a greater sensitivity. The bandgap of a stripe written at $100\,\mathrm{mm\,s}^{-1}$ was seen to act as a photodetector for wavelengths of up to $\sim 1500$ nm, compared to the 1280 nm bandgap of unstrained $Si_{0.4}Ge_{0.6}$. The material strain induced by the crystallisation will also modify the bandgap, however the extent of this has been characterised. The high tunability of the bandgap and composition presents a new technique for fabricating graded-index Si-Ge structures with different compositional requirements in a single photonic layer, with the method being theoretically applicable to a wide range of similar alloy materials.

With all processes being carried out at temperatures below 450 °C, all of the fabrication techniques demonstrated in this thesis are compatible with back-end-of-line integration into the CMOS process flow.

## 8.2 Future Work

The applications of direct laser writing as a waveguide fabrication technique, as described in this thesis, leave a myriad of potential avenues for further development. This section will outline those that have been identified so far.

In a-Si:H, the optimisation of crystallisation dynamics to limit the lateral dissipation of heat in the laser writing process may limit the outdiffusion of hydrogen, reducing transmission losses. As lower losses were obtained in the initial work undertaken with a low-power source, lower powers may in fact be more suitable, and beam shaping techniques may also influence the resulting material quality. If such low losses are obtained, the demonstration of transmission through S-bends and Y-junctions is expected. As these are building blocks for photonic circuitry, waveguiding through such components would indicate the capability of this method for the fabrication of full optical layers.

For the fabrication of polysilicon waveguides, the use of higher scanning speeds may result in larger grain sizes and associated lower propagation losses. Previous studies have recorded greater crystal grain sizes at higher scanning speeds, with Healy et al. reporting a single-crystal fiber core at $1\,\mathrm{mm\,s^{-1}}$ and Michaud et al. identifying an optimum scanning speed of $70\,\mathrm{mm\,s^{-1}}$. Reducing waveguide dimensions to $1\,\mu\mathrm{m}$ or less would also bring the cross-section more in line with that of structures used in silicon photonics for nonlinear propagation, increasing the optical intensity without changing the required power. At this stage, the majority of optical power lost during the waveguiding studies in this thesis is thought to have originated from the coupling, as the crystalline material quality was seen to be good based on Raman spectroscopy and XRD.

In photonic circuits, coupling losses would be much lower, meaning that the laser output power required to achieve the third order nonlinearities demonstrated in this work would be significantly reduced. Alternatively, equivalent laser output powers could be used to obtain much greater spectral broadening, as was discussed in Section 6.5. Similarly, the demonstration of other nonlinear mechanisms such as cross-phase modulation, Raman amplification and four-wave mixing would consolidate the potential of polysilicon for use in optical nonlinear applications. A primary attraction of polysilicon is its deposition flexibility, and so the fabrication of multilayer photonic systems is a significant step that must at some point be undertaken. Furthermore, as polysilicon has uses in microelectronics as well as optics, the characterisation of the electron mobility of such large grain material may serve to expand the applications of the laser crystallisation process to other fields.

Finally, the preliminary work to tailor the compositional segregation of silicon-germanium opens the door to a vast range of potential applications. The optimisation of material composition is critical for device fabrication as the optical properties must be selected for the desired applications. A more comprehensive investigation into the relation between

laser scanning speed and composition, as well as into the resulting optical, electrical and material properties of the processed material, would provide the full range of information needed for this design process. From there, the fabrication of devices such as photodetectors, the demonstration of waveguiding and the characterisation of nonlinear optical effects would prove the suitability of this laser writing technique for the fabrication of full optical circuitry layers. Notably, waveguiding in Si-rich laser-written stripes would require additional etching to ensure confinement, whereas waveguiding in Ge-rich stripes is possible due to the higher refractive index of Ge compared to Si. Additionally, the highly tunable velocity-dependent composition should allow for the fabrication of low-dimension structures such as Bragg gratings using a variable scanning speed. Finally, silicon-germanium is only one example of a binary alloy structure, and so this laser writing process should be applicable to a wide array of other materials.

# Appendix A

# Polysilicon Loss Measurements

| **Waveguide** | **Width** (µm) | **Speed** ($mm\,s^{-1}$) | **Power** (mW) | **Propagation Loss** ($dB\,cm^{-1}$) | **Coupling Loss** (dB) |
|---|---|---|---|---|---|
| 21.1.E.1 | 3 | 0.1 | 285 | 7.31 | 23.93 |
| 21.1.E.3 | | | | 13.16 | 22.95 |
| 21.1.E.4 | | | | 8.03 | 30.66 |
| 21.1.E.5 | | | | 3.98 | 25.78 |
| 21.1.E.6 | | | | 6.91 | 23.30 |
| 21.1.E.7 | | | | 14.57 | 22.63 |
| 21.1.E.8 | | | | 12.62 | 23.84 |
| 21.1.F.3 | 4 | 0.1 | 288 | 17.13 | 14.07 |
| 21.1.F.4 | | | | 16.85 | 16.72 |
| 21.1.F.5 | | | | 11.81 | 20.86 |
| 21.1.F.6 | | | | 10.06 | 22.86 |
| 21.1.F.7 | | 1 | 354 | 11.91 | 20.52 |
| 21.1.F.8 | | | | 10.53 | 20.86 |
| 21.1.F.9 | | | | 11.73 | 20.82 |
| 21.1.F.10 | | | | 13.23 | 17.08 |
| OLD.2.B.4 | 2 | 1 | 392 | 11.63 | 24.63 |
| OLD.2.B.7 | | | | 9.22 | 22.79 |
| OLD.2.C.2 | 2 | 1 | 295 | 16.99 | 21.48 |
| OLD.2.C.7 | | | 283 | 9.26 | 24.53 |
| OLD.2.C.10 | | | | 14.09 | 18.82 |
| 23.1.A.1 | 3 | 0.1 | 285 | 15.77 | 17.30 |
| 23.1.C.1 | 3 | 0.1 | 285 | 15.59 | 13.61 |
| 23.1.C.2 | | | | 11.38 | 24.10 |
| 23.1.C.4 | | | | 2.67 | 31.23 |

Table A.1: All transmission losses obtained where the linear fit to the results has an rms value $> 0.6$, section 1.

| **Waveguide** | **Width** (µm) | **Speed** ($mm\,s^{-1}$) | **Power** (mW) | **Propagation Loss** ($dB\,cm^{-1}$) | **Coupling Loss** (dB) |
|---|---|---|---|---|---|
| 23.2.A.3 | 3 | 0.1 | 285 | 7.88 | 32.5 |
| 23.2.A.6 | | | | 10.65 | 27.96 |
| 23.2.A.7 | | | | 22.91 | 7.73 |
| 23.2.A.8 | | | | 15.24 | 19.86 |
| 23.2.A.10 | | | | 22.62 | 10.67 |
| 23.2.B.6 | 3 | 0.1 | 285 | 2.93 | 36.56 |
| 23.2.B.8 | | | | 17.63 | 14.64 |
| 23.2.B.9 | | | | 6.55 | 27.09 |
| 23.2.B.10 | | | | 7.63 | 26.95 |
| 23.2.C.2 | 3 | 0.1 | 285 | 13.74 | 22.55 |
| 23.2.C.3 | | | | 7.48 | 29.2 |
| 23.2.C.4 | | | | 7.52 | 27.27 |
| 23.2.C.5 | | | | 9.60 | 24.51 |
| 23.2.C.7 | | | | 11.57 | 25.4 |
| 23.2.C.8 | | | | 16.62 | 16.45 |
| 23.2.C.9 | | | | 9.87 | 22.02 |
| 23.2.D.7 | 3 | 0.1 | 285 | 12.33 | 27.32 |
| 23.2.D.8 | | | | 8.01 | 31.71 |
| 23.2.D.10 | | | | 11.42 | 23.82 |
| 23.2.E.7 | 3 | 0.1 | 285 | 2.41 | 32.59 |
| 23.2.E.8 | | | | 2.79 | 33.13 |
| 23.2.E.9 | | | | 3.32 | 33.91 |
| 23.2.E.10 | | | | 8.46 | 24.79 |
| 23.2.F.1 | 3 | 0.1 | 285 | 7.95 | 29.12 |
| 23.2.F.2 | | | | 10.39 | 25.46 |
| 23.2.F.3 | | | | 15.25 | 17.02 |
| 23.2.F.4 | | | | 16.56 | 16.48 |
| 23.2.F.5 | | | | 13.14 | 17.87 |
| 23.2.F.6 | | | | 11.69 | 24.24 |
| 23.2.F.7 | | | | 10.46 | 23.25 |

TABLE A.2: All transmission losses obtained where the linear fit to the results has an rms value $> 0.6$, section 2.

# Appendix B

# 1.6 mm Crystal

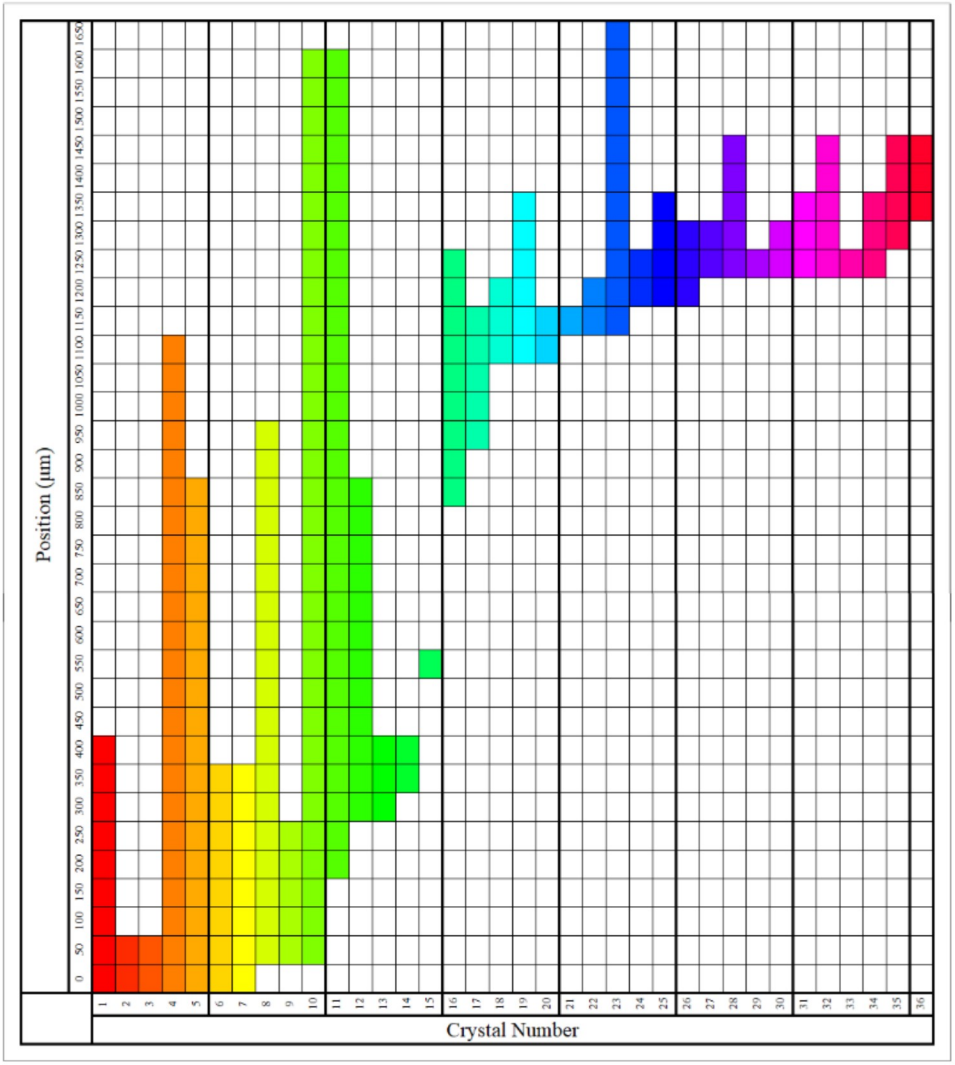


FIGURE B.1: Crystal 10 has a recorded length of 1.6 mm. A total of 103 crystals were identified along the 9.3 mm long waveguide.

# Appendix C

# List of Publications

## C.1 Journal Papers

1. Aktas, O., **MacFarquhar, S. J.**, Oo, S. Z., Tarazona, A., Chong, H. M. H. and Peacock, A. C. "Nonlinear properties of laser-processed polycrystalline silicon waveguides for integrated photonics". *Optics Express*, vol. 28, no. 20, pp. 29192-29201, 2020.

2. Aktas, O., Oo, S. Z., **MacFarquhar, S. J.**, Mittal, V., Chong, H. M. H. and Peacock, A. C. "Laser-Driven Phase Segregation and Tailoring of Compositionally Graded Microstructures in Si-Ge Nanoscale Thin Films". *ACS Applied Materials and Interfaces*, vol. 12, no. 8, pp. 9457-9467, 2020.

## C.2 Conference Papers

1. **MacFarquhar, S. J.**, Aktas, O., Oo, S. Z., Tarazona, A., Chong, H. M. H. and Peacock, A. C., "Nonlinear Characterization of Laser Processed Polysilicon Waveguides for Integrated Photonics," in *CLEO: Applications and Technology* (San José), 2021.

2. **MacFarquhar, S. J.**, Aktas, O., Oo, S. Z., DONG, Chong, H. M. H. and Peacock, A. C., "Fabrication of Hydrogenated Amorphous Silicon Waveguides via a Lithography-Free Direct Laser Writing Method," in *Conference on Lasers and Electro-Optics*, 2020. *(Withdrawn)*

3. Peacock, A. C., **MacFarquhar, S. J.**, Franz, Y., Runge, A. F. J., Mailis, S., Oo, S. Z., Mittal, V., Chong, H. M. H. and Aktas, O. (2020). "Laser processed semiconductors for integrated photonic devices - INVITED". *EPJ Web of Conferences*, vol. 238, 01001, 2020.

4. Aktas, O., **MacFarquhar, S. J.**, Oo, S. Z., Mittal, V., Chong, H. M. H. and Peacock, A. C., "Laser-Written Silicon-Germanium Alloy Microstructures with Tunable Compositionally Graded Profiles," in *CLEO: Science and Innovations* (Washington), SF2R.5, 2020.

5. Aktas, O., Franz, Y., Runge, A. F. J., **MacFarquhar, S. J.**, Oo, S. Z., Tarazona, A., Chong, H. M. H., Mailis, S. and Peacock, A. C. "Laser Processing of Amorphous Semiconductors on Planar Substrates for Photonic and Optoelectronic Applications Laser Processing of Amorphous Semiconductors on Planar Substrates for Photonic and Optoelectronic Applications", *The International Conference on Metamaterials, Photonic Crystals and Plasmonics* (Lisbon), 2019.

# Bibliography


[1] R. A. Soref and J. P. Lorenzo, "Single-Crystal Silicon: A New Material For 1.3 And 1.6 µm Integrated-Optical Components," *Electronics Letters*, vol. 21, no. 21, pp. 693–694, 1985.

[2] R. A. Soref and J. P. Lorenzo, "All-silicon active and passive guided-wave components for $\lambda = 1.3$ and 1.6 µm," *IEEE Journal of Quantum Electronics*, vol. 22, no. 6, pp. 873–879, 1986.

[3] Optical Connections, *Silicon photonics ready for take-off towards 'multibillion-dollar' market*, Accessed May 5 2021, created December 5 2016. [Online]. Available: `https://opticalconnectionsnews.com/2016/12/silicon-photonics-ready-take-off-towards-multibillion-dollar-market/`.

[4] Emergen Research, *Silicon Photonics Market By Product, By Component, By End-Use, By Region Forecasts to 2027*, Accessed May 5, 2021. [Online]. Available: `https://www.emergenresearch.com/industry-report/silicon-photonics-market`.

[5] H. H. Li, "Refractive index of silicon and germanium and its wavelength and temperature derivatives," *Journal of Physical and Chemical Reference Data*, vol. 9, no. 3, pp. 561–658, 1980.

[6] J. Cardenas, C. B. Poitras, J. T. Robinson, K. Preston, L. Chen, and M. Lipson, "Low loss etchless silicon photonic waveguides," *Optics Express*, vol. 17, no. 6, pp. 4752–4757, 2009.

[7] M. A. Popović, T. Barwicz, M. R. Watts, P. T. Rakich, L. Socci, E. P. Ippen, F. X. Kärtner, and H. I. Smith, "Multistage high-order microring-resonator add–drop filters," *Optics Letters*, vol. 31, no. 17, pp. 2571–2573, 2006.

[8] L. Liao, D. Samara-Rubio, M. Morse, A. Liu, D. Hodge, D. Rubin, U. D. Keil, and T. Franck, "High speed silicon Mach-Zehnder modulator," *Optics Express*, vol. 13, no. 8, p. 3129, 2005.

[9] V. R. Almeida, C. A. Barrios, R. R. Panepucci, and M. Lipson, "All-optical control of light on a silicon chip," *Nature*, vol. 431, no. 7012, pp. 1081–1084, 2004.

[10] Q. Xu, B. Schmidt, S. Pradhan, and M. Lipson, "Micrometre-scale silicon electro-optic modulator," *Nature*, vol. 435, no. 7040, pp. 325–327, 2005.

[11] H. Rong, R. Jones, A. Liu, O. Cohen, D. Hak, A. Fang, and M. Paniccia, "A continuous-wave Raman silicon laser," *Nature*, vol. 433, no. 7027, pp. 725–727, 2005.

[12] Y. H. Chen, J. D. Hwang, C. Y. Kung, P. S. Chen, C. S. Wei, C. K. Wu, and J. C. Liu, "Improving the performance of SiGe metal-semiconductor-metal photodetectors by using an amorphous silicon passivation layer," *IEEE Electron Device Letters*, vol. 28, no. 12, pp. 1111–1113, 2007.

[13] J. S. Orcutt, R. J. Ram, and V. Stojanović, "Integration of silicon photonics into electronic processes," in *Photonics West (Silicon Photonics VIII)*, vol. 8629, 2013, 86290F.

[14] M. Schneider, I. K. Schuller, and A. Rahman, "Epitaxial growth of silicon: A molecular-dynamics simulation," *Physical Review B*, vol. 36, no. 2, pp. 1340–1343, 1987.

[15] J. S. Orcutt, S. D. Tang, S. Kramer, K. Mehta, H. Li, V. Stojanović, and R. J. Ram, "Low-loss polysilicon waveguides fabricated in an emulated high-volume electronics process," *Optics Express*, vol. 20, no. 7, pp. 7243–7254, 2012.

[16] S. Bernabè, "Opportunities and challenges of silicon photonics based System-In-Package," in *IEEE 64th Electronic Components and Technology Conference: Emerging Technologies and Market Trends of Silicon Photonics*, Orlando, USA, 2014.

[17] T. Institute, *Packaging*, Accessed May. 11, 2022. [Online]. Available: `https://www.tyndall.ie/packaging/`.

[18] T. Barwicz, T. W. Lichoulas, Y. Taira, Y. Martin, S. Takenobu, A. Janta-Polczynski, H. Numata, E. L. Kimbrell, J. W. Nah, B. Peng, D. Childers, R. Leidy, M. Khater, S. Kamlapurkar, E. Cyr, S. Engelmann, P. Fortier, and N. Boyer, "Automated, high-throughput photonic packaging," *Optical Fiber Technology*, vol. 44, no. February, pp. 24–35, 2018.

[19] J. C. C. Fan and H. J. Zeiger, "Crystallization of amorphous silicon films by Nd:YAG laser heating," *Applied Physics Letters*, vol. 27, no. 4, pp. 224–226, 1975.

[20] A. Gat, L. Gerzberg, J. F. Gibbons, T. J. Magee, J. Peng, and J. D. Hong, "CW laser anneal of polycrystalline silicon: Crystalline structure, electrical properties," *Applied Physics Letters*, vol. 33, no. 8, pp. 775–778, 1978.

[21] D. K. Biegelsen, N. M. Johnson, D. J. Bartelink, and M. D. Moyer, "Laser-induced crystallization of silicon islands on amorphous substrates: Multilayer structures," *Applied Physics Letters*, vol. 38, no. 3, pp. 150–152, 1981.

[22] J. Sakurai, S. Kawamura, H. Mori, and M. Nakano, "Lateral epitaxial growth in poly-Si film over SiO2 from single-Si seed by scanning CW Ar laser annealing," *Japanese Journal of Applied Physics*, vol. 20, no. 3, pp. L176–L178, 1981.

[23] T. J. Stultz and J. F. Gibbons, "The use of beam shaping to achieve large-grain cw laser-recrystallized polysilicon on amorphous substrates," *Applied Physics Letters*, vol. 39, no. 6, pp. 498–500, 1981.

[24] G. K. Celler, L. E. Trimble, K. K. Ng, H. J. Leamy, and H. Baumgart, "Seeded oscillatory growth of Si over $SiO_2$ by cw laser irradiation," *Applied Physics Letters*, vol. 40, no. 12, pp. 1043–1045, 1982.

[25] S. Kawamura, J. Sakurai, M. Nakano, and M. Takagi, "Recrystallization of Si on amorphous substrates by doughnut-shaped CW Ar laser beam," *Applied Physics Letters*, vol. 40, no. 5, pp. 394–395, 1982.

[26] H. Kuriyama, S. Kiyama, S. Noguchi, T. Kuwahara, S. Ishida, T. Nohda, K. Sano, H. Iwata, H. Kawata, M. Osumi, S. Tsuda, S. Nakano, and Y. Kuwano, "Enlargement of poly-Si film grain-size by excimer laser annealing and its application to high-performance poly-Si thin-film transistor," *Japanese Journal of Applied Physics*, vol. 30, no. 12B, pp. 3700–3703, 1991.

[27] J. S. Im, H. J. Kim, and M. O. Thompson, "Phase transformation mechanisms involved in excimer laser crystallization of amorphous silicon films," *Applied Physics Letters*, vol. 63, no. 14, pp. 1969–1971, 1993.

[28] A. M. Agarwal, L. Liao, J. S. Foresi, M. R. Black, X. Duan, and L. C. Kimerling, "Low-loss polycrystalline silicon waveguides for silicon photonics," *Journal of Applied Physics*, vol. 80, no. 11, pp. 6120–6123, 1996.

[29] M. Modreanu, M. Gartner, N. Tomozeiu, C. Cobianu, P. Cosmin, and R. Gavrila, "Microstructural and Optical Properties of LPCVD Polysilicon Films," in *2001 International Semiconductor Conference*, Sinaia: IEEE, 2001, pp. 387–390.

[30] A. Hara, M. Takei, F. Takeuchi, K. Suga, K. Yoshino, M. Chida, T. Kakehi, Y. Ebiko, Y. Sano, and N. Sasaki, "High Performance Low Temperature Polycrystalline Silicon Thin Film Transistors on Non-alkaline Glass Produced Using Diode Pumped Solid State Continuous Wave Laser Lateral Crystallization," *Japanese Journal of Applied Physics*, vol. 43, no. 4A, pp. 1269–1276, 2004.

[31] S. J. Park, Y. M. Ku, K. H. Kim, E. H. Kim, B. K. Choo, J. S. Choi, S. H. Kang, Y. J. Lim, and J. Jang, "CW laser crystallization of amorphous silicon; dependence of amorphous silicon thickness and pattern width on the grain size," *Thin Solid Films*, vol. 511, pp. 243–247, 2006.

[32] C.-C. Kuo, "On-Line Determination of Average Grain Size of Polycrystalline Silicon," *Journal of Russian Laser Research*, vol. 32, no. 1, pp. 12–18, 2011.

[33] N. Healy, S. Mailis, N. M. Bulgakova, P. J. A. Sazio, T. D. Day, J. R. Sparks, H. Y. Cheng, J. V. Badding, and A. C. Peacock, "Extreme electronic bandgap modification in laser-crystallized silicon optical fibres," *Nature Materials*, vol. 13, no. September, pp. 1–6, 2014.

[34] N. Healy, M. Fokine, Y. Franz, T. H. Hawkins, M. Jones, J. Ballato, A. C. Peacock, and U. J. Gibson, "CO2 laser-induced directional recrystallization to produce single crystal silicon-core optical fibers with low loss," *Advanced Optical Materials*, vol. 4, no. 7, pp. 1004–1008, 2016.

[35] Y. Franz, A. F. J. Runge, S. Z. Oo, G. Jimenez-Martinez, N. Healy, A. Khokhar, A. Tarazona, H. M. H. Chong, S. Mailis, and A. C. Peacock, "Laser crystallized low-loss polycrystalline silicon waveguides," *Optics Express*, vol. 27, no. 4, p. 4462, 2019.

[36] J. S. Foresi, M. R. Black, A. M. Agarwal, and L. C. Kimerling, "Losses in polycrystalline silicon waveguides," *Applied Physics Letters*, vol. 68, no. 15, pp. 2052–2054, 1996.

[37] L. Liao, D. R. Lim, A. M. Agarwal, X. Duan, K. K. Lee, and L. C. Kimerling, "Optical transmission losses in polycrystalline silicon strip waveguides," *Journal of Electronic Materials*, vol. 29, no. 12, pp. 1380–1386, 2000.

[38] K. Preston, B. Schmidt, and M. Lipson, "Polysilicon photonic resonators for large-scale 3D integration of optical networks," *Optics Express*, vol. 15, no. 25, pp. 17 283–17 290, 2007.

[39] Q. Fang, J. F. Song, S. H. Tao, M. B. Yu, G. Q. Lo, and D. L. Kwong, "Low loss ($6.45\,\mathrm{dB\,cm^{-1}}$) sub-micron polycrystalline silicon waveguide integrated with efficient SiON waveguide coupler," *Optics Express*, vol. 16, no. 9, pp. 6425–6432, 2008.

[40] K. Preston, P. Dong, B. Schmidt, and M. Lipson, "High-speed all-optical modulation using polycrystalline silicon microring resonators," *Applied Physics Letters*, vol. 92, no. 15, pp. 90–93, 2008.

[41] K. Preston, S. Manipatruni, A. Gondarenko, C. B. Poitras, and M. Lipson, "Deposited silicon high-speed integrated electro-optic modulator," *Optics Express*, vol. 17, no. 7, pp. 5118–5124, 2009.

[42] D. Kwong, J. Covey, A. Hosseini, Y. Zhang, X. Xu, and R. T. Chen, "Ultralow-loss polycrystalline silicon waveguides and high uniformity 1x12 MMI fanout for 3D photonic integration," *Optics Express*, vol. 20, no. 19, p. 21 722, 2012.

[43] S. Cheemalapati, M. Ladanov, J. Winskas, and A. Pyayt, "Optimization of dry etching parameters for fabrication of polysilicon waveguides with smooth sidewall using a capacitively coupled plasma reactor.," *Applied Optics*, vol. 53, no. 25, pp. 5745–9, 2014.

[44] T. M. B. Masaud, A. Tarazona, E. Jaberansary, X. Chen, G. T. Reed, G. Z. Mashanovich, and H. M. H. Chong, "Hot-wire polysilicon waveguides with low deposition temperature.," *Optics Letters*, vol. 38, no. 20, pp. 4030–2, 2013.

[45] K. Preston, C. B. Poitras, M. O. Thompson, and M. Lipson, "Photonic devices in low-temperature laser-crystallized deposited silicon," in *Conference on Lasers and Electro-Optics*, 2010, pp. 5–6.

[46] Y. H. D. Lee, M. O. Thompson, and M. Lipson, "Deposited low temperature silicon GHz modulator," *Optics Express*, vol. 21, no. 22, pp. 26 688–92, 2013.

[47] A. Voutsas, "A new era of crystallization: Advances in polysilicon crystallization and crystal engineering," *Applied Surface Science*, vol. 208-209, no. 1, pp. 250–262, 2003.

[48] C.-C. Kuo, "Micro-Raman spectroscopy characterization of polycrystalline silicon films fabricated by excimer laser crystallization," *Optics and Lasers in Engineering*, vol. 47, no. 5, pp. 612–616, 2009.

[49] G. Martinez-Jimenez, Y. Franz, A. F. J. Runge, M. Ceschia, N. Healy, S. Z. Oo, A. Tarazona, H. M. H. Chong, A. C. Peacock, and S. Mailis, "Photonic microstructures produced by selective etching of laser-crystallized amorphous silicon," *Optical Materials Express*, vol. 9, no. 6, pp. 2573–2581, 2019.

[50] S. Z. Oo, A. Tarazona, A. Z. Khokhar, R. Petra, Y. Franz, G. Z. Mashanovich, G. T. Reed, A. C. Peacock, and H. M. H. Chong, "Hot-wire chemical vapor deposition low-loss hydrogenated amorphous silicon waveguides for silicon photonic devices," *Photonics Research*, vol. 7, no. 2, pp. 193–200, 2019.

[51] K. Narayanan and S. F. Preble, "Optical nonlinearities in hydrogenated- amorphous silicon waveguides," *Optics Express*, vol. 18, no. 9, pp. 8998–9005, 2010.

[52] P. Mehta, N. Healy, N. F. Bavril, P. J. A. Sazio, J. V. Badding, and A. C. Peacock, "Nonlinear transmission properties of hydrogenated amorphous silicon core fibers towards the mid-infrared regime," *Optics Express*, vol. 21, no. 11, pp. 552–554, 2013.

[53] K. Li and A. C. Foster, "Parametric Nonlinear Silicon-Based Photonics," *Proceedings of the IEEE*, vol. 106, no. 12, pp. 2196–2208, 2018.

[54] K. K. Lee, D. R. Lim, L. C. Kimerling, J. Shin, and F. Cerrina, "Fabrication of ultralow-loss $Si/SiO_2$ waveguides by roughness reduction," *Optics Letters*, vol. 26, no. 23, p. 1888, 2001.

[55] M. A. Ettabib, L. Xu, A. Bogris, A. Kapsalis, M. Belal, E. Lorent, P. Labeye, S. Nicoletti, K. Hammani, D. Syvridis, D. P. Shepherd, J. H. Price, D. J. Richardson, and P. Petropoulos, "Telecom to mid-infrared supercontinuum generation in a silicon germanium waveguide," *Optics Letters*, vol. 40, no. 17, pp. 4118–4121, 2015.

[56] J. M. Ramirez, V. Vakarin, J. Frigerio, P. Chaisakul, D. Chrastina, X. Le Roux, A. Ballabio, L. Vivien, G. Isella, and D. Marris-Morini, "Ge-rich graded-index $Si_{1-x}Ge_x$ waveguides with broadband tight mode confinement and flat anomalous dispersion for nonlinear mid-infrared photonics," *Optics Express*, vol. 25, no. 6, p. 6561, 2017.

[57] B. Jalali, V. Raghunathan, R. Shori, S. Fathpour, D. Dimitropoulos, and O. Stafsudd, "Prospects for silicon mid-IR Raman lasers," *IEEE Journal on Selected Topics in Quantum Electronics*, vol. 12, no. 6, pp. 1618–1626, 2006.

[58] T. Tsuchizawa, K. Yamada, H. Fukuda, T. Watanabe, S. Uchiyama, and S. Itabashi, "Low-loss Si wire waveguides and their application to thermooptic switches," *Japanese Journal of Applied Physics, Part 1: Regular Papers and Short Notes and Review Papers*, vol. 45, no. 8 B, pp. 6658–6662, 2006.

[59] V. Raghunathan, R. Claps, D. Dimitropoulos, and B. Jalali, "Parametric Raman Wavelength Conversion in Scaled Silicon Waveguides," *Journal of Lightwave Technology*, vol. 23, no. 6, pp. 2094–2101, 2005.

[60] Z. Wang, H. Liu, N. Huang, Q. Sun, and J. Wen, "Impact of dispersion profiles of silicon waveguides on optical parametric amplification in the femtosecond regime," *Optics Express*, vol. 19, no. 24, p. 24 730, 2011.

[61] Y. Wei, Y. Zhao, J. Yang, M. Wang, and X. Jiang, "Chirp characteristics of silicon Mach-Zehnder modulator under small-signal modulation," *Journal of Lightwave Technology*, vol. 29, no. 7, pp. 1011–1017, 2011.

[62] L. Yin, Q. Lin, and G. P. Agrawal, "Soliton fission and continuum generation in silicon waveguides," *Optics Letters*, vol. 32, no. 4, pp. 391–393, 2007.

[63] J. M. Fedeli, M. Migette, L. Di Cioccio, L. El Melhaoui, R. Orobtchouk, C. Seassal, P. Rojo-Romeo, F. Mandorlo, D. Marris-Morini, and L. Vivien, "Incorporation of a photonic layer at the metallization levels of a CMOS circuit," *IEEE International Conference on Group IV Photonics GFP*, vol. 2, pp. 200–202, 2006.

[64] I. M. Soganci, A. La Porta, and B. J. Offrein, "Flip-chip optical couplers with scalable I/O count for silicon photonics," *Optics Express*, vol. 21, no. 13, pp. 16 075–16 085, 2013.

[65] Y. Chen, H. Li, and M. Li, "Flexible and tunable silicon photonic circuits on plastic substrates," *Scientific Reports*, vol. 2, no. 622, pp. 1–6, 2012.

[66] S. Pae, T. Su, J. P. Denton, and G. W. Neudeck, "Multiple layers of silicon-on-insulator islands fabrication by selective epitaxial growth," *IEEE Electron Device Letters*, vol. 20, no. 5, pp. 194–196, 1999.

[67] A. Harke, M. Krause, and J. Mueller, "Low-loss singlemode amorphous silicon waveguides," *Electronics Letters*, vol. 41, no. 25, pp. 1377–1379, 2005.

[68] S. Rao, C. D'Addio, and F. Della Corte, "All-optical modulation in a CMOS-compatible amorphous silicon-based device," *Journal of the European Optical Society - Rapid publications*, vol. 7, no. 0, pp. 2011–2013, 2012.

[69] G. Cocorullo, F. G. Della Corte, R. De Rosa, I. Rendina, A. Rubino, and E. Terzini, "Amorphous silicon-based guided-wave passive and active devices for silicon integrated optoelectronics," *IEEE Journal on Selected Topics in Quantum Electronics*, vol. 4, no. 6, pp. 997–1001, 1998.

[70] R. A. Street, *Hydrogenated Amorphous Silicon*, ser. Cambridge Solid State Science Series. Cambridge University Press, 1991.

[71] A. Gat and J. F. Gibbons, "A laser-scanning apparatus for annealing of ion-implantation damage in semiconductors," *Applied Physics Letters*, vol. 32, no. 3, pp. 142–144, 1978.

[72] A. Gat, J. F. Gibbons, T. J. Magee, J. Peng, V. R. Deline, P. Williams, and C. A. Evans, "Physical and electrical properties of laser-annealed ion-implanted silicon," *Applied Physics Letters*, vol. 32, no. 5, pp. 276–278, 1978.

[73] E. P. Donovan, F. Spaepen, D. Turnbull, J. M. Poate, and D. C. Jacobson, "Heat of crystallization and melting point of amorphous silicon," *Applied Physics Letters*, vol. 42, no. 8, pp. 698–700, 1983.

[74] W. B. Jackson, N. M. Johnson, and D. K. Biegelsen, "Density of gap states of silicon grain boundaries determined by optical absorption," *Applied Physics Letters*, vol. 43, pp. 195–197, 1983.

[75] R. E. Jones and S. P. Wesolowski, "Electrical, thermoelectric, and optical properties of strongly degenerate polycrystalline silicon films," *Journal of Applied Physics*, vol. 56, pp. 1701–1706, 1984.

[76] S. K. Selvaraja, M. Schaekers, W. Bogaerts, D. Van Thourhout, and R. Baets, "Polycrystalline silicon as waveguide material for advanced photonic applications," in *Proceedings of 11th IEEE/LEOS Benelux Annual Workshop*, Eindhoven, 2007, pp. 19–20.

[77] S. Zhu, Q. Fang, M. B. Yu, G. Q. Lo, and D. L. Kwong, "Propagation losses in undoped and n-doped polycrystalline silicon wire waveguides," *Optics Express*, vol. 17, no. 23, p. 20 891, 2009.

[78] Y. H. D. Lee and M. Lipson, "Back-end deposited silicon photonics for monolithic integration on CMOS," *IEEE Journal of Selected Topics in Quantum Electronics*, vol. 19, no. 2, 2013.

[79] Y. Franz, "Polycrystalline Silicon Waveguides for Integrated Photonics," PhD Thesis, University of Southampton, Faculty of Physical Sciences and Engineering, 2018.

[80] H. Stöhr and W. Klemm, "Über Zweistoffsysteme mit Germanium. I. Germanium/Aluminium, Germanium/Zinn und Germanium/Silicium," *Zeitschrift für anorganische und allgemeine Chemie*, vol. 241, no. 4, pp. 305–313, 1939.

[81] J. Liu, M. Beals, A. Pomerene, S. Bernardis, R. Sun, J. Cheng, L. C. Kimerling, and J. Michel, "Waveguide-integrated, ultralow-energy GeSi electro-absorption modulators," *Nature Photonics*, vol. 2, no. 7, pp. 433–437, 2008.

[82] S. Abdul Hadi, P. Hashemi, N. DiLello, E. Polyzoeva, A. Nayfeh, and J. L. Hoyt, "Thin-film $Si_{1-x}Ge_x$ HIT solar cells," *Solar Energy*, vol. 103, pp. 154–159, 2014.

[83] Y. Kim, M. Yokoyama, N. Taoka, M. Takenaka, and S. Takagi, "Ge-rich SiGe-on-insulator for waveguide optical modulator application fabricated by Ge condensation and SiGe regrowth," *Optics Express*, vol. 21, no. 17, p. 19 615, 2013.

[84] J. Kang, M. Takenaka, and S. Takagi, "Novel Ge waveguide platform on Ge-on-insulator wafer for mid-infrared photonic integrated circuits," *Optics Express*, vol. 24, no. 11, p. 11 855, 2016.

[85] F. Schaffler, in *Properties of Advanced Semiconductor Materials GaN, AlN, InN, BN, SiC, SiGe*, L. M.E., R. S.L., and S. M.S., Eds., New York: John Wiley & Sons Inc., 2001, pp. 149–188.

[86] Y. Abdulraheem, I. Gordon, T. Bearda, H. Meddeb, and J. Poortmans, "Optical bandgap of ultra-thin amorphous silicon films deposited on crystalline silicon by PECVD," *AIP Advances*, vol. 4, no. 5, 2014.

[87] I. P.-T. Institute, *Silicon Germanium Band Structure and Carrier Concentration*, Accessed Feb. 24, 2022. [Online]. Available: `http://www.ioffe.ru/SVA/NSM/Semicond/SiGe/bandstr.html`.

[88] L. Shen, N. Healy, P. Mehta, T. D. Day, J. R. Sparks, J. V. Badding, and A. C. Peacock, "Nonlinear transmission properties of hydrogenated amorphous silicon core fibers towards the mid-infrared regime," *Optics Express*, vol. 21, no. 11, p. 13 075, 2013.

[89] N. K. Hon, R. Soref, and B. Jalali, "The third-order nonlinear optical coefficients of Si, Ge, and $Si_{1-x}Ge_x$ in the midwave and longwave infrared," *Journal of Applied Physics*, vol. 110, no. 1, 2011.

[90] B. U. Sohn, C. Monmeyran, L. C. Kimerling, A. M. Agarwal, and D. T. Tan, "Kerr nonlinearity and multi-photon absorption in germanium at mid-infrared wavelengths," *Applied Physics Letters*, vol. 111, no. 9, pp. 1–6, 2017.

[91] D. Lu, P. Morin, B. Sahu, T. B. Hook, P. Hashemi, A. Scholze, B. Kim, P. Kerber, A. Khakifirooz, P. Oldiges, K. Rim, and B. Doris, "(Invited) Silicon Germanium FinFET Device Physics, Process Integration and Modeling Considerations," *ECS Transactions*, vol. 64, no. 6, pp. 337–345, 2014.

[92] C. Jacoboni, F. Nava, C. Canali, and G. Ottaviani, "Electron drift velocity and diffusivity in germanium," *Physical Review B*, vol. 24, no. 2, pp. 1014–1026, 1981.

[93] M. Morales, D. Munoz-Martin, Y. Chen, O. García, J. J. García-Ballesteros, J. Cárabe, J. J. Gandía, and C. Molpeceres, "Study of a-Si crystallization dependence on power and irradiation time using a CW green laser," in *Laser-based Micro- and Nanoprocessing VIII*, vol. 8968, 2014, 89680U.

[94] S. Jin, S. Hong, M. Mativenga, B. Kim, H. H. Shin, J. K. Park, T.-W. Kim, and J. Jang, "Low temperature polycrystalline silicon with single orientation on glass by blue laser annealing," *Thin Solid Films*, vol. 616, pp. 838–841, 2016.

[95] K. Sera, F. Okumura, H. Uchida, S. Itoh, S. Kaneko, and K. Hotta, "High-Performance TFT's Fabricated by XeCl Excimer Laser Annealing of Hydrogenated Amorphous-Silicon Film," *IEEE Transactions on Electron Devices*, vol. 36, no. 12, pp. 2868–2872, 1989.

[96] S. Sedky, A. Witvrouw, H. Bender, and K. Baert, "Experimental determination of the maximum post-process annealing temperature for standard CMOS wafers," *IEEE Transactions on Electron Devices*, vol. 48, no. 2, pp. 377–385, 2001.

[97] M. W. Geis, D. C. Flanders, and H. I. Smith, "Crystallographic orientation of silicon on an amorphous substrate using an artificial surface-relief grating and laser crystallization," *Applied Physics Letters*, vol. 35, no. 1, pp. 71–74, 1979.

[98] J. F. Gibbons, K. F. Lee, T. J. Magee, J. Peng, and R. Ormond, "CW laser recrystallization of $\langle 1\,0\,0 \rangle$ Si on amorphous substrates," *Applied Physics Letters*, vol. 34, no. 12, pp. 831–833, 1979.

[99] G. S. Ganot, "Laser Crystallization of Silicon Thin Films for Three-Dimensional Integrated Circuits," PhD Thesis, Columbia University, 2012.

[100] J. F. Michaud, R. Rogel, T. Mohammed-Brahim, and M. Sarret, "Cw argon laser crystallization of silicon films: Structural properties," *Journal of Non-Crystalline Solids*, vol. 352, no. 9-20 SPEC. ISS. Pp. 998–1002, 2006.

[101] Thorlabs, *Silicon Windows*, Accessed Jan. 12, 2021. [Online]. Available: `https://www.thorlabs.com/NewGroupPage9.cfm?ObjectGroup_ID=3979`.

[102] ——, *Germanium Windows*, Accessed Oct. 7, 2021. [Online]. Available: `https://www.thorlabs.com/newgrouppage9.cfm?objectgroup_ID=3980`.

[103] D. Marcuse, "Mode Conversion Caused by Surface Imperfections of a Dielectric Slab Waveguide," *Bell System Technical Journal*, vol. 48, no. 10, pp. 3187–3215, 1969.

[104] F. P. Payne and J. P. R. Lacey, "A theoretical analysis of scattering loss from planar optical waveguides," *Optical and Quantum Electronics*, vol. 26, no. 10, pp. 977–986, 1994.

[105] R. Pafchek, R. Tummidi, J. Li, M. A. Webster, E. Chen, and T. L. Koch, "Low-loss silicon-on-insulator shallow-ridge TE and TM waveguides formed using thermal oxidation," *Applied Optics*, vol. 48, no. 5, pp. 958–963, 2009.

[106] T. G. Nguyen and A. Mitchell, "Polarisation dependent scattering loss in thin, shallow-ridge silicon-on-insulator waveguides with resonant lateral leakage," in *35th Australian Conference on Optical Fibre Technology*, Melbourne: IEEE, 2010, pp. 10–12.

[107] A. H. Mahan, J. Carapella, B. P. Nelson, R. S. Crandall, and I. Balberg, "Deposition of device quality, low H content amorphous silicon," *Journal of Applied Physics*, vol. 69, no. 9, pp. 6728–6730, 1991.

[108] K. F. Feenstra, R. E. Schropp, and W. F. Van Der Weg, "Deposition of amorphous silicon films by hot-wire chemical vapor deposition," *Journal of Applied Physics*, vol. 85, no. 9, pp. 6843–6852, 1999.

[109] R. E. Schropp, "Hot Wire Chemical Vapor Deposition: Recent Progress, Present State of the Art and Competitive Opportunities," *ECS Transactions*, vol. 25, no. 8, pp. 3–14, 2019.

[110] C. Kittel, *Introduction to Solid State Physics*, 8th ed. New York: John Wiley & Sons, Inc., 2004.

[111] M. Okamura and S. Suzuki, "Infrared Photodetection Using a-Si:H Photodiode," *IEEE Photonics Technology Letters*, vol. 6, no. 3, pp. 412–414, 1994.

[112] O. B. Gusev, A. N. Kuznetsov, E. I. Terukov, M. S. Bresler, V. K. Kudoyarova, I. N. Yassievich, B. P. Zakharchenya, and W. Fuhs, "Room-temperature electroluminescence of erbium-doped amorphous hydrogenated silicon," *Applied Physics Letters*, vol. 70, no. 2, pp. 240–242, 1997.

[113] S. Zhu, G. Q. Lo, and D. L. Kwong, "Low-loss amorphous silicon wire waveguide for integrated photonics: effect of fabrication process and the thermal stability," *Optics Express*, vol. 18, no. 24, pp. 25 283–25 291, 2010.

[114] M. Borselli, T. J. Johnson, and O. Painter, "Beyond the Rayleigh scattering limit in high-Q silicon microdisks: theory and experiment," *Optics Express*, vol. 13, no. 5, p. 1515, 2005.

[115] O. Ogah, "Free-carrier effects in polycrystalline silicon-on-insulator photonic devices," Ph.D. dissertation, Rochester Institute of Technology, 2010, pp. 51–52.

[116] Q. Xu, S. Manipatruni, B. Schmidt, J. Shakya, and M. Lipson, "12.5 Gbit/s carrier-injection-based silicon micro-ring silicon modulators," *Optics Express*, vol. 15, no. 2, pp. 430–436, 2007.

[117] K. Okamoto, *Wave theory of optical waveguides*, 2nd ed. San Diego: Elsevier Science & Technology, 2006.

[118] A. Brimont, D. J. Thomson, P. Sanchis, J. Herrera, F. Gardes, J. M. Fedeli, G. T. Reed, and J. Martí, "High speed silicon electro-optical modulators enhanced via slow light propagation," *Optics Express*, vol. 19, no. 21, p. 20 876, 2011.

[119] F. H. Suhailin, L. Shen, N. Healy, L. Xiao, M. Jones, T. H. Hawkins, J. Ballato, U. J. Gibson, and A. C. Peacock, "Tapered polysilicon core fibers for nonlinear photonics," *Optics Letters*, vol. 41, no. 7, p. 1360, 2016.

[120] PeriodicTable.org, *Silicon – Thermal Conductivity*, Accessed Nov. 12, 2021. [Online]. Available: `https://www.periodic-table.org/silicon-thermal-conductivity/`.

[121] AZO Materials, *Silica - Silicon Dioxide ($SiO_2$)*, Accessed Nov. 12, 2021. [Online]. Available: `https://www.azom.com/properties.aspx?ArticleID=1114`.

[122] Crystran, *Silica Glass (SiO2)*, Accessed Nov. 24, 2021. [Online]. Available: `https://www.crystran.co.uk/optical-materials/silica-glass-sio2`.

[123] PeriodicTable.org, *Silicon - Thermal Expansion Coefficient*, Accessed Nov. 24, 2021. [Online]. Available: `https://www.periodic-table.org/silicon-thermal-expansion/`.

[124] J. Filik, A. W. Ashton, P. C. Chang, P. A. Chater, S. J. Day, M. Drakopoulos, M. W. Gerring, M. L. Hart, O. V. Magdysyuk, S. Michalik, A. Smith, C. C. Tang, N. J. Terrill, M. T. Wharmby, and H. Wilhelm, "Processing two-dimensional X-ray diffraction and small-angle scattering data in DAWN 2," *Journal of Applied Crystallography*, vol. 50, no. 3, pp. 959–966, 2017.

[125] M. A. Foster, K. D. Moll, and A. L. Gaeta, "Optimal waveguide dimensions for nonlinear interactions," *Optics Express*, vol. 12, no. 13, pp. 299–305, 2004.

[126] B. Jalali, O. Boyraz, D. Dimitropoulos, and V. Raghunathan, "Scaling laws of nonlinear silicon nanophotonics," in *Proc. SPIE 5730, Optoelectronic Integration on Silicon II*, J. A. Kubby and G. E. Jabbour, Eds., San Jose, pp. 41–49.

[127] R. L. Espinola, J. I. Dadap, R. M. Osgood, Jr., S. J. McNab, and Y. A. Vlasov, "C-band wavelength conversion in silicon photonic wire waveguides," *Optics Express*, vol. 13, no. 11, p. 4341, 2005.

[128] Y.-H. Kuo, H. Rong, V. Sih, S. Xu, M. Paniccia, and O. Cohen, "Demonstration of wavelength conversion at 40 Gb/s data rate in silicon waveguides," *Optics Express*, vol. 14, no. 24, p. 11 721, 2006.

[129] C. Koos, P. Vorreau, T. Vallaitis, P. Dumon, W. Bogaerts, R. Baets, B. Esembeson, I. Biaggio, T. Michinobu, F. Diederich, W. Freude, and J. Leuthold, "All-optical high-speed signal processing with silicon-organic hybrid slot waveguides," *Nature Photonics*, vol. 3, no. 4, pp. 216–219, 2009.

[130] H. Ji, H. Hu, M. Galili, L. K. Oxenløwe, M. Pu, K. Yvind, J. M. Hvam, and P. Jeppesen, "Optical waveform sampling and error-free demultiplexing of 1.28 Tbit/s serial data in a silicon nanowire," in *National Fiber Optic Engineers Conference*, San Diego, 2010, pp. 8–10.

[131] Y. Ding, J. Xu, H. Ou, and C. Peucheret, "Mode-selective wavelength conversion based on four-wave mixing in a multimode silicon waveguide," *Optics Express*, vol. 22, no. 1, p. 127, 2014.

[132] F. Dell'Olio and V. M. Passaro, "Optical sensing by optimized silicon slot waveguides," *Optics Express*, vol. 15, no. 8, p. 4977, 2007.

[133] J. T. Robinson, L. Chen, and M. Lipson, "On-chip gas detection in silicon optical microcavities," *Optics Express*, vol. 16, no. 6, pp. 4296–4301, 2008.

[134] D. Dorfner, T. Zabel, T. Hürlimann, N. Hauke, L. Frandsen, U. Rant, G. Abstreiter, and J. Finley, "Photonic crystal nanostructures for optical biosensing applications," *Biosensors and Bioelectronics*, vol. 24, no. 12, pp. 3688–3692, 2009.

[135] R. Claps, D. Dimitropoulos, V. Raghunathan, Y. Han, and B. Jalali, "Observation of stimulated Raman amplification in silicon waveguides," *Optics Express*, vol. 11, no. 15, pp. 1731–1739, 2003.

[136] T. K. Liang and H. K. Tsang, "Efficient Raman amplification in silicon-on-insulator waveguides," *Applied Physics Letters*, vol. 85, no. 16, pp. 3343–3345, 2004.

[137] H. Rong, A. Liu, R. Jones, O. Cohen, D. Hak, R. Nicolaescu, A. Fang, and M. Paniccla, "An all-silicon Raman laser," *Nature*, vol. 433, no. 7023, pp. 292–294, 2005.

[138] I. W. Hsieh, X. Chen, X. Liu, J. I. Dadap, N. C. Panoiu, C. Y. Chou, F. Xia, W. M. Green, Y. A. Vlasov, and R. M. Osgood, "Supercontinuum generation in silicon photonic wires," *Optics Express*, vol. 15, no. 23, pp. 15 242–15 249, 2007.

[139] W. Ding, C. Benton, A. V. Gorbach, W. J. Wadsworth, J. C. Knight, D. V. Skryabin, M. Gnan, M. Sorrel, and R. M. De La Rue, "Solitons and spectral broadening in long silicon-on- insulator photonic wires," *Optics Express*, vol. 16, no. 5, p. 3310, 2008.

[140] F. Leo, S.-P. Gorza, J. Safioui, P. Kockaert, S. Coen, U. Dave, B. Kuyken, and G. Roelkens, "Dispersive wave emission and supercontinuum generation in a silicon wire waveguide pumped around the 1550 nm telecommunication wavelength," *Optics Letters*, vol. 39, no. 12, p. 3623, 2014.

[141] N. Singh, D. D. Hudson, and B. J. Eggleton, "Silicon-on-sapphire pillar waveguides for Mid-IR supercontinuum generation," *Optics Express*, vol. 23, no. 13, p. 17 345, 2015.

[142] M. Borghi, C. Castellan, S. Signorini, A. Trenti, and L. Pavesi, "Nonlinear silicon photonics," *Journal of Optics*, vol. 19, no. 9, 2017.

[143] Y. Liu and H. K. Tsang, "Time dependent density of free carriers generated by two photon absorption in silicon waveguides," *Applied Physics Letters*, vol. 90, no. 21, pp. 10–13, 2007.

[144] G. P. Agrawal, *Nonlinear Fiber Optics*, 5th. Boston: Academic Press, 2013, pp. 27–56.

[145] P. V. Mamyshev, "All-optical data regeneration based on self-phase modulation effect," in *24th European Conference on Optical Communication. ECOC '98 (IEEE Cat. No.98TH8398)*, Madrid, 1998, pp. 475–476.

[146] F. Parmigiani, M. Ibsen, T. T. Ng, L. Provost, P. Petropoulos, and D. J. Richardson, "An efficient wavelength converter exploiting a grating-based saw-tooth pulse shaper," *IEEE Photonics Technology Letters*, vol. 20, no. 17, pp. 1461–1463, 2008.

[147] P. Mehta, N. Healy, J. R. Sparks, T. D. Day, P. J. Sazio, J. V. Badding, and A. C. Peacock, "Ultrafast all-optical modulation in silicon optical fibers," in *Frontiers in Optics 2011/Laser Science XXVII*, San Jose, 2011, pp. 4–6.

[148] H. K. Tsang, C. S. Wong, T. K. Liang, I. E. Day, S. W. Roberts, A. Harpin, J. Drake, and M. Asghari, "Optical dispersion, two-photon absorption and self-phase modulation in silicon waveguides at 1.5 µm wavelength," *Applied Physics Letters*, vol. 80, no. 3, pp. 416–418, 2002.

[149] M. Dinu, F. Quochi, and H. Garcia, "Third-order nonlinearities in silicon at telecom wavelengths," *Applied Physics Letters*, vol. 82, no. 18, pp. 2954–2956, 2003.

[150] G. W. Rieger, K. S. Virk, and J. F. Young, "Nonlinear propagation of ultrafast 1.5 $\mu$m pulses in high-index-contrast silicon-on-insulator waveguides," *Applied Physics Letters*, vol. 84, no. 6, pp. 900–902, 2004.

[151] Q. Lin, O. J. Painter, and G. P. Agrawal, "Nonlinear optical phenomena in silicon waveguides: modeling and applications," *Optics Express*, vol. 15, no. 25, p. 16 604, 2007.

[152] A. C. Peacock, P. Mehta, P. Horak, and N. Healy, "Nonlinear pulse dynamics in multimode silicon core optical fibers," *Optics Letters*, vol. 37, no. 16, p. 3351, 2012.

[153] N. Sasaki, M. Arif, Y. Uraoka, J. Gotoh, and S. Sugimoto, "Unseeded crystal growth of (100)-oriented grain-boundary-free Si thin-film by a single scan of the CW-laser lateral crystallization of a-Si on insulator," *Crystals*, vol. 10, no. 5, 2020.

[154] D. C. Harris, "Durable 3-5 µm transmitting infrared window materials," *Infrared Physics and Technology*, vol. 39, no. 4, pp. 185–201, 1998.

[155] M. J. Süess, R. Geiger, R. A. Minamisawa, G. Schiefler, J. Frigerio, D. Chrastina, G. Isella, R. Spolenak, J. Faist, and H. Sigg, "Analysis of enhanced light emission from highly strained germanium microbridges," *Nature Photonics*, vol. 7, no. 6, pp. 466–472, 2013.

[156] J. R. Jain, A. Hryciw, T. M. Baer, D. A. Miller, M. L. Brongersma, and R. T. Howe, "A micromachining-based technology for enhancing germanium light emission via tensile strain," *Nature Photonics*, vol. 6, no. 6, pp. 398–405, 2012.

[157] J. Liu, X. Sun, R. Camacho-Aguilera, L. C. Kimerling, and J. Michel, "Ge-on-Si laser operating at room temperature," *Optics Letters*, vol. 35, no. 5, p. 679, 2010.

[158] D. J. Paul, "Si/SiGe heterostructures: From material and physics to devices and circuits," *Semiconductor Science and Technology*, vol. 19, no. 10, 2004.

[159] S. Chiussi, E. López, J. Serra, P. González, C. Serra, B. León, F. Fabbri, L. Fornarini, and S. Martelli, "Influence of laser fluence in ArF-excimer laser assisted crystallisation of a-SiGe:H films," *Applied Surface Science*, vol. 208-209, no. 1, pp. 358–363, 2003.

[160] M. Weizman, N. H. Nickel, I. Sieber, and B. Yan, "Successive segregation in laser-crystallized poly-SiGe thin films," *Journal of Non-Crystalline Solids*, vol. 352, no. 9-20, pp. 1259–1262, 2006.

[161] C. Y. Ong, K. L. Pey, X. Li, X. C. Wang, C. M. Ng, and L. Chan, "Laser annealing induced high Ge concentration epitaxial SiGe layer in Si1-x Gex virtual substrate," *Applied Physics Letters*, vol. 93, no. 4, pp. 1–4, 2008.

[162] D. A. Coucheron, M. Fokine, N. Patil, D. W. Breiby, O. T. Buset, N. Healy, A. C. Peacock, T. Hawkins, M. Jones, J. Ballato, and U. J. Gibson, "Laser recrystallization and inscription of compositional microstructures in crystalline SiGe-core fibres," *Nature Communications*, vol. 7, 2016.

[163] A. F. J. Runge, Y. Franz, C. G. Littlejohns, K. Grabska, S. Mailis, F. Y. Gardes, and A. C. Peacock, "Laser-assisted material composition engineering of SiGe planar waveguides," in *CLEO - Pacific Rim*, Singapore, 2017.

[164] O. Aktas, S. Z. Oo, S. J. MacFarquhar, V. Mittal, H. M. H. Chong, and A. C. Peacock, "Laser-Driven Phase Segregation and Tailoring of Compositionally Graded Microstructures in Si-Ge Nanoscale Thin Films," *ACS Applied Materials and Interfaces*, vol. 12, no. 8, 2020.

[165] F. Pezzoli, E. Bonera, E. Grilli, M. Guzzi, S. Sanguinetti, D. Chrastina, G. Isella, H. von Känel, E. Wintersberger, J. Stangl, and G. Bauer, "Raman spectroscopy determination of composition and strain in $Si_{1-x}Ge_x$ / Si heterostructures," *Materials Science in Semiconductor Processing*, vol. 11, no. 5, pp. 279–284, 2008.

[166] T. S. Perova, J. Wasyluk, K. Lyutovich, E. Kasper, M. Oehme, K. Rode, and A. Waldron, "Composition and strain in thin $Si_{1-x}Ge_x$ virtual substrates measured by micro-Raman spectroscopy and x-ray diffraction," *Journal of Applied Physics*, vol. 109, no. 3, 2011.

[167] D. Rouchon, M. Mermoux, F. Bertin, and J.-M. Hartmann, "Germanium content and strain in $Si_{1-x}Ge_x$ alloys characterized by Raman spectroscopy," *Journal of Crystal Growth*, vol. 392, pp. 66–73, 2014.

[168] C. J. Kim, H. S. Lee, Y. J. Cho, J. E. Yang, R. R. Lee, J. K. Lee, and M. H. Jo, "On-nanowire band-graded Si:Ge photodetectors," *Advanced Materials*, vol. 23, no. 8, pp. 1025–1029, 2011.

[169] A. Gassenq, F. Gencarelli, J. Van Campenhout, Y. Shimura, R. Loo, G. Narcy, B. Vincent, and G. Roelkens, "GeSn/Ge heterostructure short-wave infrared photodetectors on silicon," *Optics Express*, vol. 20, no. 25, p. 27 297, 2012.

[170] R. Takei, S. Manako, E. Omoda, Y. Sakakibara, M. Mori, and T. Kamei, "Sub-1 dB/cm submicrometer-scale amorphous silicon waveguide for backend on-chip optical interconnect," *Optics Express*, vol. 22, no. 4, p. 4779, 2014.